UNIVERSITÀ DEGLI STUDI DI MILANO

Scuola di Dottorato in Fisica, Astrofisica e Fisica Applicata

Ciclo XXXV

Electro-Optical and Electro-Mechanical Response of Ferroelectric Nematic Fluids

Settore Scientifico Disciplinare FIS/03

Supervisore: Professor Tommaso Bellini

Tesi di Dottorato di:
Federico Caimi

Anno Accademico: 2021/2022

To my sweet Elena

"Maybe nothing in this world happens by accident.
As everything happens for a reason, our destiny slowly takes form"
(Silvers Reyleigh, Eiichirō Oda, One Piece)

Commission of the final examination:

External Referees:
Prof. Roberto Caputo
Prof. Francesca Serra

External Members:
Prof. Liana Lucchetti
Prof. Richard J. Mandle

Internal Member:
Prof. Tommaso Bellini

Final examination:

Date: 23/02/2023
Università degli Studi di Milano, Dipartimento di Fisica, Milano, Italy

Cover illustration:

Polarized optical microscopy image of RM734 confined in a microchannel

MIUR subjects:

FIS/03

Contents

List of Figures

List of Tables

Introduction

Motivation

Liquid crystals are a particular state of matter in which molecules possess both properties of crystalline solids (e.g. fixed molecular orientation, optical anisotropy etc.) and conventional liquids (e.g. fluidity, positional disorder etc.). Thanks to their optical uniaxiality, fluidity, elasticity, responsiveness to electric fields and controllable coupling of the molecular orientation at the interface with solid surfaces, they played a huge role in the last century technology, especially into displays and optical devices.

Depending on how the molecules are relatively positioned and oriented, a large number of different mesophases can be defined; among them, one of the more, if not the most, relevant for technological applications is the so-called thermotropic nematic phase (N), in which rod-like molecules roughly share a common orientation while preserving the lack of long-range positional order found in a conventional liquid. It's worth noting that, even if the mesogens – the molecules composing the phase – are polar and with chemically distinct terminals, the overall phase is non-polar, since the molecular interactions cannot distinguish between these ends, resulting in an almost equal number of molecules being aligned in a parallel or in an antiparallel way respect the common direction.

The polar analog of this phase, called ferroelectric nematic phase (N_F), in which the mesogens are all aligned in the same direction, has been theoretically predicted by Born[1] and Debye[2] in the first years of the 19th century and never observed until, in 2017, Mandle et al.[3] and Nishikawa et al.[4] simultaneously synthesized two different and highly polar compounds showing multiple nematic phases once cooled from the isotropic phase. These newly discovered mesophases were noted by the two groups to possess ferroelectric-like properties, but only three years later Chen et al.[5] fully understood the nature of the low temperature nematic phase shown by RM734, one of these two molecules, and depicted it as N_F.

Such findings open a whole new field of explorations in liquid crystal and more broadly into soft matter research with new physical effects[6], caused by the polar symmetry breaking, for example: the coupling between the alignment of the phase and electric/magnetic fields; the behaviour of topological defects; the surface anchoring; the hydrodynamics under electromagnetic fields; the interplay of bound and free electric charges; the study the pretransitional regions; the interplay of polarity and chirality.

Furthermore, the properties of N_F phase, including the enormous spontaneous polarization coupled with its fluidity, the fast response to electric fields and the non linear optic capabilities makes these materials optimal candidates for the realization of next

generation technological devices such as displays, signal modulators, memories and optical instruments.

Thesis overview

Main results

Led by the aforementioned motivations, the present thesis is focused on the study of the physical properties of the ferroelectric nematic phase of RM734, in an effort to both enlarge the basic knowledge of this particular mesophase and provide new tools and hints for the development of future technological devices. The main results of this thesis are summarized below.

Surface alignment of RM734 on different materials
The surface alignment of the N_F phase of RM734 confined into flat cells realized with various rubbed and unrubbed surfaces has been explored[7]. These observations allowed the discovery that the confining surfaces played a strong role on the formation of different orientational patterns, textures, defect structures and field response and allowed to demonstrate that the 3D structuring of the macroscopic polarization **P** of the N_F phase can be controlled by designing the polarity of the 2D bounding surfaces, a key aspect of nematic liquid crystal science and its potential for technology. Furthermore, the appearance of the polar order during the N-N_F transition changes the interactions of the director with bounding surfaces even driving, for a specific substrate, the alignment from homeotropic in N phase to planar once in N_F phase.

Electrostatic instability of RM734 sessile droplets on lithium niobate surfaces
When a droplet of RM734 is deposited on top of a lithium niobate ferroelectric crystal and cooled below the temperature of the N-N_F transition, it can suddenly become unstable, disintegrating through the emission of fluid jets[8]. These jets are mostly interfacial, spreading out on the substrate surface, and exhibit fractal branching out into smaller streams to eventually disrupt, forming secondary droplets which can undergo successive explosions as the temperature is further lowered. This behaviour has been interpreted as a particular case of Rayleigh instability happening when the electrostatic repulsion, caused by the accumulation of polarization charges on the droplet surface, overcomes the surface tension of the liquid. These polarization charges are provoked by the coupling between the bulk polarization of the ferroelectric liquid and the pyroelectric polarization of the ferroelectric crystal through its fringing field and solid-fluid interface contact. This kind of polarization-induced Rayleigh instability crucially depends on the unique combination of polarization and fluidity of the ferroelectric nematic and might provide the basis for electrohydromechanical applications.

Electric superscreening and electric field guiding into RM734-filled microchannels
After filling custom-made microchannels buried in monolithic fused silica with RM734, connecting their endings to gold electrodes and applying low electric fields E_0 to the N_F phase of the material the orientation of the nematic director, thus the bulk polarization, continuously follows the winding paths of the channel, regardless of its shape[9]. Differently shaped channels have been tested finding that the polarization was always directed parallel to the solid surfaces, regularly following the channel even in their curved sections bending contrary to the naïve electrode-to-electrode direction expected for E_0 in uniform dielectrics. The continuity of N_F polarization along the channels also implies a similar continuity of the electric field, which thus

follows the material rather than being directed along the paths connecting the electrodes as in homogeneous dielectric media. We understand this effect as a consequence of a so-called *ferroelectric superscreening* that cancels the normal components of **E**, which is thus parallel to the channel axis within the channel. Because of the large value of **P**, much larger than typical surface charges displaced in conventional experimental conditions, such cancellation is achieved with tilt angles δ between **P** and the surfaces of at most $\delta \approx 10^{-7}$ rad, an angular variation so small to be impossible to observe. The screening and guiding effect is not dissimilar to what happens in a bent conductive wire between electrodes, where the surface accumulation of free charges steers the field along the wire, independently of its path.

Switching dynamics of RM734 confined into microchannels after the inversion of the electric field: Upon switching the sign of an electric field E_0 applied to the N_F phase of RM734 confined into the forenamed microchannels, a complex multiscale switching event is promptly generated. The whole switching process is completely dominated by electrostatic forces and at least three different moments can be distinguished. At first the system breaks into micron-sized domains in which **P** locally rotates away from the original orientation in a variety of directions leading to a very thin and sandy texture. Then, once the domains rotated enough to start reorganizing in the opposite direction, they start to merge forming a twisted, highly-defected texture; these defect walls could be the boundaries between two opposite-rotating domains. The last stage of the inversion is the reorganization of the molecules bound to the channel surfaces which eliminates the twists, disentangle the defect lines and leaves an homogeneous, well-aligned texture. This last process is completed through the motion of two soliton-like interfaces, nucleated in the slimmest section of the channel and running towards the electrodes with a velocity v_I linearly dependant on E_0. The electric superscreening, the guided electric field and the multiscale switching process were furthermore confirmed by numerical simulations of a continuum model of quasi-2D N_F liquid crystal in microchannels showing, regardless the consistent simplifications applied, results very similar to the experimental observations.

Microchannels with complex geometries: The great flexibility of the microchannel fabrication process allowed us to realize channel with bifurcations and producing geometries in which the N_F phase, due to its polar nature, cannot simply follow the channel walls without forming topological defects. The analysis of the switching dynamics in microchannels with a bifurcation revealed that the electric field is not uniform in the whole channel, but it is reduced after the bifurcation. Furthermore, the study of complex geometries revealed the presence of asymmetric responses, possibly arising from a difference between the positive and the negative splay of RM734.

Thesis outline

The current thesis consists of a total of seven chapters, grouped into four parts comprising the different thematics faced during the study of the N_F phase of RM734. Part I, composed by chapters 1 and 2, presents RM734, the material studied in this thesis, focusing on the general characteristics of liquid crystals and the particular features of the ferroelectric nematic phase N_F. Part II and III are uniquely composed by a single chapter each, respectively chapters 3 and 4, introducing different responses of RM734 in contact with different materials; Part II is indeed focused on behaviour of the N_F phase when confined into variously treated flat cells while Part III is focused on the response of a sessile droplet of the ferroelectric liquid deposited onto a ferroelectric crystal. Part IV, corresponding to the last two chapters, is dedicated to the study of RM734 confined into differently-shaped microchannels connecting electrodes under the effect of weak electric fields. The principal content of each chapter is summarized here below.

Chapter 1 – Liquid crystals and liquid crystalline phases
This thesis starts with some basic notion about liquid crystals and a brief description of their principal mesophases. A short presentation of the main physical properties of liquid crystals considered in this work is also added.

Chapter 2 – RM734 and the ferroelectric nematic phase
After considering the general properties of different liquid crystal mesophases the focus is moved on the main actors of this thesis, the molecule RM734 and its recently discovered ferroelectric nematic phase. Together with the main features and the principal questions involving this mesophase, a small overview of the state of the art is presented in this chapter.

Chapter 3 – Surface alignment of RM734
The behaviour of RM734 confined into flat cells is thoroughly investigated and described into this chapter. In particular, we realized and tested a set of four distinct rubbed and unrubbed surfaces showing different anchoring strength and predictable polar and quadrupolar alignment. This findings allowed us to demonstrate that, controlling the polarity of the 2D bounding surfaces, it is possible to organize the vectorial orientation distribution of a 3D volume of polar molecules.

Chapter 4 – Explosive electrostatic instability of RM734 droplets on ferroelectric solid surfaces
Upon depositing RM734 droplets onto a lithium niobate crystal and cooling the system below the N-N_F temperature we observed an electromechanical instability of the liquid crystal material which provokes the explosion of the droplet and the emission of fluid branches. In this chapter, a phenomenological description of this event is provided alongside a plausible interpretation of this occurrence.

Chapter 5 – Electric superscreening and polarization control in RM734 confined in microchannels Filling a set of differently-shaped microchannels with RM734 and applying low electric field to their terminals, we found that the polarization continuously follows the winding path of the channels, even in sections bent in the opposite direction of the expected electric field – electrode to electrode oriented –, which would be present in absence of the liquid crystal material. Our interpretation of this phenomenon and the study of the complex, multi-scale dynamics occurring upon the inversion of the applied electric field are treated into this chapter. A numerical simulation of a continuum model of quasi-2D N_F liquid crystal in microchannels, confirming the experimental data, is also presented here.

Chapter 6 – Topological defects in frustrated RM734 confined in microchannels Designing appropriate microchannels is furthermore possible to create bifurcations and situations in which, due to the intimate nature of the N_F phase, a continuous and polar order cannot be achieved leading to the formation of topological defects. In this chapter the study of the electric field in complex RM734-filled microchannels and some observations on the obtained defect lines are presented.

Bibliography

[1] M. Born. Über anisotrope flüssigkeiten. versuch einer theorie der flüssigen kristalle und des elektrischen kerr-effekts in flüssigkeitenn. *Sitzungsber. Preuss. Akad Wiss.*, 30: 614–650, 1916.

[2] P. Debye. Einige resultate einer kinetischen theorie der isolatoren. *Phys. Z.*, 13:97–100, 1912.

[3] R. J. Mandle, S. J. Cowling, and J. W. Goodby. A nematic to nematic transformation exhibited by a rod-like liquid crystal. *Physical Chemistry Chemical Physics*, 19:11429–11435, 2017.

[4] H. Nishikawa, K. Shiroshita, H. Higuchi, Y. Okumura, Y. Haseba, S. I. Yamamoto, K. Sago, and H. Kikuchi. A fluid liquid-crystal material with highly polar order. *Advanced Materials*, 29, 11 2017.

[5] X. Chen, E. Korblova, D. Dong, X. Wei, R. Shao, L. Radzihovsky, M. A. Glaser, J. E. Maclennan, D. Bedrov, D. M. Walba, and N. A. Clark. First-principles experimental demonstration of ferroelectricity in a thermotropic nematic liquid crystal: Polar domains and striking electro-optics. *Proceedings of the National Academy of Sciences*, 117: 14021–14031, 2020.

[6] O. D. Lavrentovich. Ferroelectric nematic liquid crystal, a century in waiting. *Proceedings of the National Academy of Sciences*, 117(26):14629–14631, 2020.

[7] F. Caimi, G. Nava, R. Barboza, N. A. Clark, E. Korblova, D. M. Walba, T. Bellini, and L. Lucchetti. Surface alignment of ferroelectric nematic liquid crystals. *Soft Matter*, 17:8130–8139, 2021.

[8] R. Barboza, S. Marni, F. Ciciulla, F. A. Mir, G. Nava, F. Caimi, A. Zaltron, N. A. Clark, T. Bellini, and L. Lucchetti. Explosive electrostatic instability of ferroelectric liquid droplets on ferroelectric solid surfaces. *Proceedings of the National Academy of Sciences*, 119(32):e2207858119, 2022.

[9] F. Caimi, G. Nava, S. Fuschetto, L. Lucchetti, P. Paiè, R. Osellame, X. Chen, N. A. Clark, M. Glaser, and T. Bellini. Superscreening and polarization control in confined ferroelectric nematic liquids. *arXiv*, 2022. URL `https://arxiv.org/abs/2210.00886`.

Part I

The ferroelectric nematic phase

CHAPTER 1

Liquid Crystals

1.1 An organized fluid state of matter

All the matter we experience every day exists in one, or more, of the many different states of molecular organization which can be recognized and defined from their distinct physical properties. As a result of the different type and degree of orientational and positional order of their constitutive atoms or molecules, different substances in various physical states may or may not, for example, be able to change shape to fit a container or occupy the whole volume available. The three main and most famous states, although not unique, are the gas, liquid and solid states. Molecules in gaseous state are completely free to move and thus occupy the whole volume available, interactions within particles in isotropic liquid state are higher resulting in a constant volume, however molecules are still free enough to move into the phase adapting the shape of the material to the one of the container; the orientation of the particles in both gas and liquid states are completely random. When the strength of the interactions between the molecules are further increased the solid state is obtained: in this state both the position and the orientation of the particles are fixed, resulting in a material with a fixed volume and shape, regardless of the shape and the size of the container. Solid matter can be further divided into crystalline and amorphous solids, in the firsts the molecules orientation is constant and their position is fixed onto the points of a lattice while for the seconds the orientations and the position are still fixed but in a random and non periodic way. Even if alongside this conventional states a huge number of different and more exotic states can be observed and described (e.g. plasma, Bose-Einstein condensate, superfluids, etc.) for the sake of this thesis the focus will be set on some particular phases whose properties are between the ones of isotropic liquids and the ones of crystalline solids and thus called mesomorphic phases (from the ancient greek $\mu\acute{\varepsilon}\sigma o\varsigma$, middle, half and $\mu o\varrho\varphi\acute{\eta}$, form, appearance). The substances which possess these *mesophases* are named liquid crystals (LC) since they show the fluidity of isotropic liquids combined with some degree of orientational and positional order, typical of crystals[1–6]. These materials can be divided into two broad classes: lyotropic LCs (from the ancient greek $\lambda\acute{\upsilon}\omega$, to dissolve and $\tau\varrho o\pi\acute{\eta}$, turning, change) are molecules that show mesophases once dissolved, at a certain concentration into a solvent and thermotropic LCs (from the ancient greek $\theta\varepsilon\varrho\mu\acute{o}\varsigma$, hot and $\tau\varrho o\pi\acute{\eta}$, turning, change) are pure substances that exhibit mesophases upon variation of temperature. Since the substances used in this work belongto this latter class, lyotropic LCs will not be further treated. A molecule capable of forming liquid crystalline mesophases is called mesogen (from the ancient greek $\mu\acute{\varepsilon}\sigma o\varsigma$, middle, half and $\gamma\acute{\varepsilon}\nu o\varsigma$, birth, origin) and usually possesses a strong anisotropic shape, either elongated (calamitic or rod-like molecules) or disk-like (discotic molecules). Depending on the various degrees of positional and orientational order different mesophases can

be described; in the following section a brief introduction on the main liquid crystalline mesomorphic phases will be given and in the next chapter the attention will be set onto the ferroelectric nematic phase (N_F), the recently-discovered mesophase subject of this work.

1.2 Thermotropic liquid crystalline phases

LC materials can arrange in many possible structures, the same mesogen can even show multiple mesophases upon varying the temperature, a property called polymorphism (from ancient greek $\pi o \lambda \acute{\upsilon} \varsigma$, much, many and $\mu o \varrho \varphi \acute{\eta}$, form, appearance). A first classification of the the four main classes of thermotropic liquid crystals can be done on the basis of the translational correlations of their constituting molecules: nematic ordering possesses no translational correlation, smectic phases has 1D correlation, columnar mesophases possesses a 2D correlation and lastly there is a large family of 3D correlated structures such as cubic and blue phases. Being this last class very broad and variegated while not having any connection with this thesis it will not be described further.

1.2.1 Nematic phase

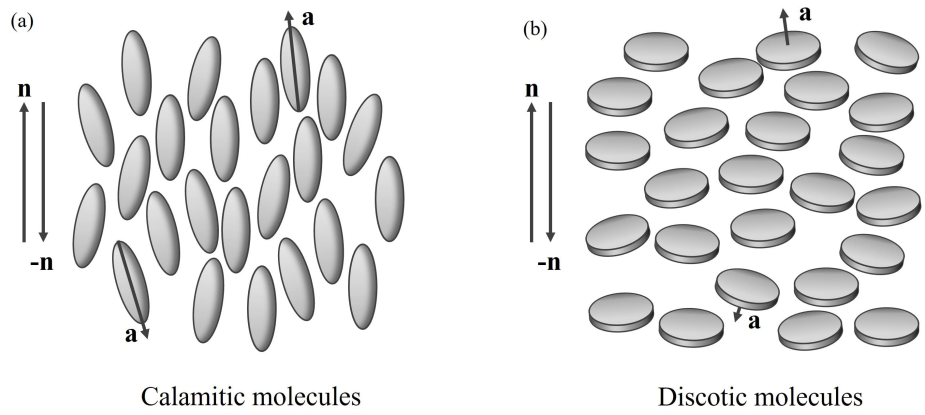

Figure 1.1: Nematic phases, (a) nematic phase of calamitic molecules, (b) nematic phase of discotic molecules, arrows represent both molecular axis **a** and nematic director **n**

The first and simplest liquid crystalline mesophase is the nematic phase (N), in which calamitic or discotic molecules can flow like in a liquid, having no correlation of the position of their centers of mass while sharing a preferential orientation of their molecular axes **a** along a common orientation represented by an unit vector **n** called nematic director (see Fig. 1.1)[3]. It's important to note that in a nematic phase, even if the constituting units are polar (as for example cyanobiphenyls), the whole phase is non-polar thanks to a centrosymmetric average arrangement of the molecules, making the notations **n** and **-n** equivalent. The director can also be seen as a $D_{\infty h}$ axis of continuous rotational symmetry[7], the same kind of axis of an homogeneous cylinder, thus its behavior for every direction perpendicular to **n** is identical. The alignment of the molecules along the director is generally not perfect like in a solid crystal; a common way to quantify the quality

of the arrangement is described by the so-called order parameter S which, for a nematic phase, can be defined as:

$$S = \frac{1}{2}\langle 3cos^2\theta - 1\rangle \tag{1.1}$$

where θ is the angle between the molecular axis **a** and the nematic director **n** while the brackets denote a spatial and temporal statistical average. Its value can span between $S = -1/2$ and $S = 1$, with $S = 0$ representing the isotropic phase and $S = 1$ respresenting a perfect alignment of the molecules along the nematic director; for a conventional nematic this value is $0.5 < S < 0.75$. $S = -1/2$ represents a particular case in which the molecular orientation is restricted to a plane perpendicular to the director. The term nematic comes from the ancient Greek word $\nu\tilde{\eta}\mu\alpha$ which means thread; this name has been chosen because when a sample of these materials is observed in a microscope it's easy to observe thread-like structures moving around: these lines are called disclinations and are caused by topological defects occurring in the bulk when the orientation of the molecules can't be unambiguously defined. This topic will be treated in more detail in section 1.4.

Cholesteric phase - the chiral nematic

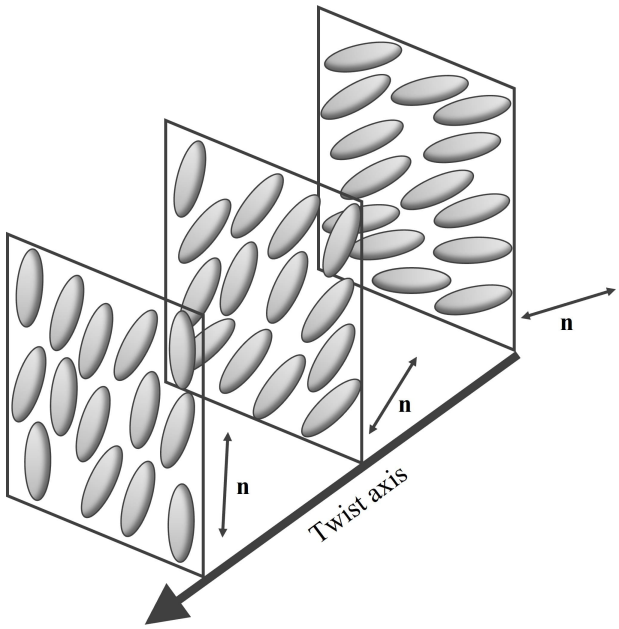

Figure 1.2: Cholesteric phase, arrows represent the continuous rotation of the director **n** along the twist axis

When the nematic mesogens are chiral, or a chiral molecule is added to a N phase, a different type of nematic phase may appear; this mesophase is called cholesteric (N*) since it was first observed with samples of different cholesterol derivatives. This phase can be considered a chiral version of the conventional nematic phase since, even in this

case, the molecules uniquely possess an orientational order and no positional correlations[3]. While being locally identical to the N phase, the N* phase differs from it because of the presence of a macroscopic twist of the director **n** along an axis perpendicular to it (Fig. 1.2), resulting in an helical structure whose pitch p can vary from $100nm$ up to $10\mu m$. Since p can be fine-tuned with the temperature or by mixing different mesogens, and since its size overlaps with the wavelength of the visible light this mesophase possess various interesting optical properties, many of them exploited both by nature[8] or by humans for realizing optical devices[9]. It's also worth noting that, due to the equivalence between **n** and **-n** the actual periodicity of the phase along the helix axis is given by the half of the pitch, $p/2$. Since the formation of this superstructure is caused by chiral factors it's easy to notice that also the cholesteric twist has a chiral character, as it can be either left-handed or right-handed, showing a partial dependence on the configuration of the chiral mesogens and their elastic constants. However a complete description of the relationship between molecular and macroscopical chirality or elastic behavior is still missing.

1.2.2 Smectic phase

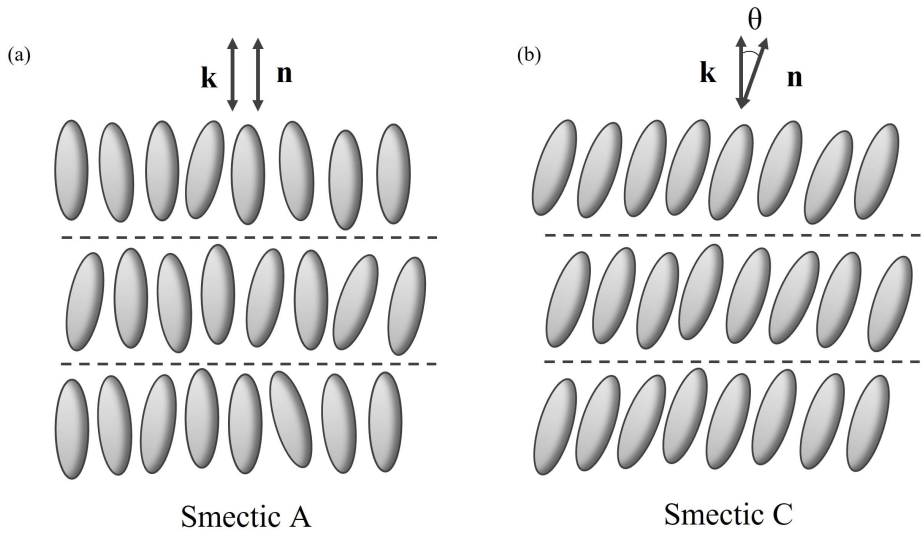

Figure 1.3: (a) Smectic A phase, (b) smectic C phase. Arrows represent both director **n** and the normal direction to the layers **k**, θ is the angle between **n** and **k**

If we start adding some degree of positional ordering to a liquid crystalline mesophase we find the class of smectic phases, named after the ancient Greek word $\sigma\mu\eta\kappa\tau\iota\kappa\acute{o}\varsigma$ meaning soap or detergent, since many materials possessing this mesophase can be used as cleansing agents. Smectic phases are characterized by a layered structure with a sinusoidal distribution of the centers of mass of the molecules in the direction perpendicular to the layers resulting in a quasi-long-range 1D translational order in that direction[4]. Within the layer the molecules are free to move like in a liquid and they can also move from a layer to another. The two main types are smectic A (SmA) and smectic C (SmC), differing in the tilt angle of the molecules inside the layers (Fig. 1.3). In a SmA phase the

molecules have their molecular axis perpendicular to the layers, resulting in a director **n** parallel to the normal to the layers **k**. Inside each layer there is no long range positional order. In a SmC phase the molecules are tiled respect to the layers, resulting in a director **n** which forms an angle θ with the normal to the layers **k**. Even in this case there is no long range positional order inside each layer. This is not true for every smectic material, in fact there are some type of smectics, called hexatic smectics, in which there is an hexagonal weak order within the molecules inside the layers. Some examples of this family are the smectic B (SmB) in which the molecules are aligned perpendicular to the layers while the smectics F and I are two different tilted versions of hexatic smectics. Even in the cases in which there is some positional correlation inside the layers there is no correlation between two distinct layers.

Ferroelectric smectic phases

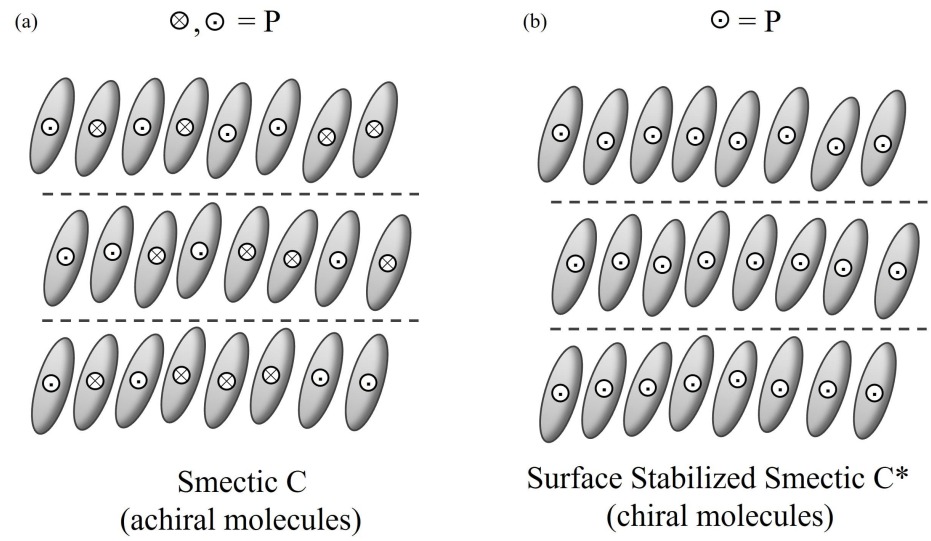

Figure 1.4: (a) Polarization in a smectic C phase, (b) Polarization in a surface stabilized smectic C* phase. Arrows entering end exiting from the plane represent the polarization **P**

If the molecules generating a smectic C phase are chiral we obtain a chiral version of this phase, called smectic C*. This phase possesses the same tilted nature of the its non-chiral analog but the tilt direction precesses around the normal to the planes **k**, creating an helical structure. Another substantial difference between these two mesophases is that in SmC, since the molecules are not chiral, the tilt plane is a mirror plane[10], preventing the presence of any polar property, such a spontaneous polarization **P** (Fig. 1.4a); however, if the molecules are chiral, as in SmC* the tilt plane is not a mirror plane anymore allowing the generation of a spontaneous polarization P perpendicular to both the director **n** and the layer normal **k**, while any other direction is prohibited for symmetry reason. In a chiral smectic C*, due to the precession of the molecules along **k**, P is macroscopically cancelled over one helical pitch, forming a so-called helielectric structure. An external electrical field **E**, giving an azimuthal torque τ = **P**x**E**, may unwind the helix, which is reformed once the field is removed. If a SmC* is confined into a thin

cell, with the smectic layers perpendicular to the cell surfaces, the molecules along the boundaries must be in the same plane of the surfaces and, if the thickness is low enough, the helix is suppressed (Fig. 1.4b). In this configuration only two states are allowed, with the spontaneous polarization pointing towards one surface or the other, it's worth to mention that by applying an electric field perpendicular to the surfaces it is possible to switch between these two bistable states. This type of structure, usable for the creation of electro-optic devices, is called surface-stabilized ferroelectric liquid crystal (SSFLC)[11]. Ferroelectricity has also been found into bent-core smectics (SmB2); these mesogens are "banana-shaped" molecules which can stack within smectic layers. This polar order, combined with a possible dipole perpendicular to the molecular long axis, would result in a spontaneous polarization along the stacks, or rather perpendicular to the layer direction $\mathbf{k}$[12].

1.2.3 Columnar phase

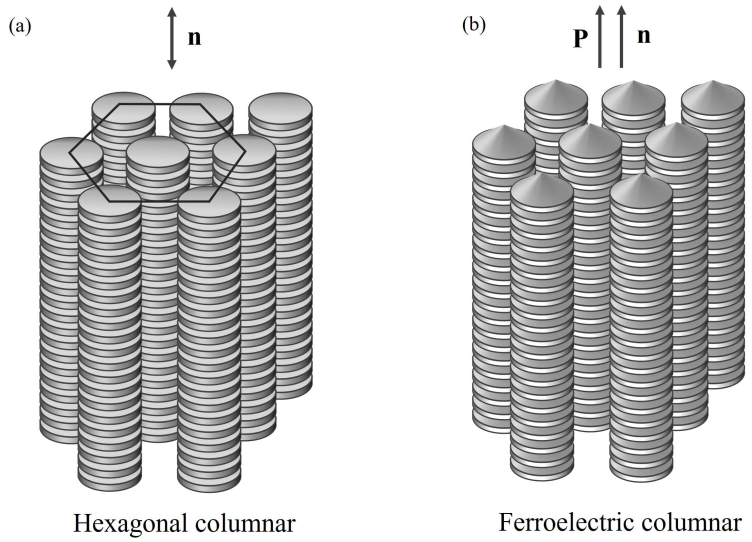

Figure 1.5: (a) Hexagonal columnar phase with the lattice highlighted, (b) Ferroelectric columnar phase. Arrows represent both director **n** and the spontaneous polarization **P**

In a columnar phase the degree of positional ordering is higher than in a smectic phase; as the name suggests, in this mesophases the constituting units (usually discotic molecules) tends to stack one in top of another forming columns, which then organizes in the space in a 2D lattice[4]. The most common structure found is the highly packed hexagonal (as in Fig. 1.5a), but a large number of variants has been identified such as tilted, rectangular, hortorombic, etc. Sometimes even a more disordered columnar nematic phase is observed, in which molecules are still packed into columns which instead undergo a nematic-like ordering. In hexagonal phase mesogens are unidirectionally aligned with a lateral hexagonal order; however, the structure is not rigid like a solid crystal since the molecules can present some disorder around their positions and are free to rotate along their longitudinal axis independently. Furthermore the columns can show a continuous bend and are able to move and slide with respect to each other.

Ferroelectric columnar phases

Using chiral disk-shaped mesogens, in analogy with the SmC* phase, is it possible to obtain columns in which the molecules are tilted with respect to the column axis[13]. Even in this case, such as in the chiral smectics, the molecules tend to form an helical structure with the polarization P rotating perpendicular to the column axis and hence macroscopically averaged to zero. Following the analogy with the SmC* this behavior can be suppressed, therefore obtaining a macroscopic polarization, unwinding the helix using electric fields or surface interactions. The polarization in this kind of systems is limited in the plane perpendicular to the columnar axis, but systems with the polarization along the columns have also been realized. This type of ferroelectric phase can be created using asymmetric disc molecules with a shape resembling a cone or a bowl with a dipole along their rotational symmetry axis; if these molecules can stack in columns a macroscopic spontaneous polarization is readily generated along the columnar axis (Fig. 1.4b). The alignment of the single columns can be either in one direction or the other but an external applied electric field can induce a common orientation of the stacks, which can be retained even after the field removal. Since the rotational viscosity of these aggregates is very high, the polarization reversal is usually achieved through the configuration inversion of the single molecule, if built by flexible subunits[14].

1.3 Optical properties of liquid crystals

Conventional liquids, such as water or oils, are called isotropic liquids since their refractive index n is independent on the direction of an incident light beam, which will be simply refracted according to Snell's law of refraction. This behavior is different to the one of the vast majority of crystalline solids and liquid crystals which in contrast are called anisotropic; in these materials an incident light beam can experiment different refractive indexes depending on its direction of propagation. This property is caused by the different polarizabilities along the axes of the molecules and their macroscopical organization. A medium with two principal refractive indices and one optical axis is called uniaxial, while a medium with three different refractive indices and two distinct optical axes is called biaxial. Since most of liquid crystalline phases are uniaxial media and since in the few exceptions (such as SmC phase) the biaxiality is very small, only uniaxial properties will be considered further on in this thesis. If the refractive index parallel to the optical axis $n_{\parallel}$ is larger than the one perpendicular to it, $n_{\perp}$, so that $\Delta n = n_{\parallel} - n_{\perp} > 0$, the material is defined to have positive birefringence or to be optically positive; when instead $\Delta n = n_{\parallel} - n_{\perp} < 0$ we have a negative birefringent material. When an incoming light beam hits a birefringent material it splits into two components an ordinary ray and an extraordinary ray propagating in different directions with their polarization perpendicular to each other. These two rays proceed through the material with two different velocities since they experience two different refractive indices called n_o and n_e which can be derived from the principal axes as:

$$n_o = n_{\perp} \tag{1.2}$$

$$n_e = \frac{n_{\parallel} n_{\perp}}{\sqrt{n_{\parallel}^2 cos^2\phi + n_{\perp}^2 sin^2\phi}} \tag{1.3}$$

where ϕ is the angle between between the optical axis and the direction of light propagation. Proceeding through the media at two different velocities the two beams gain a

phase difference δ, given by:

$$\delta = \frac{2\pi}{\lambda}(n_e - n_o)d \tag{1.4}$$

where λ is the wavelength of the beam in the vacuum and d is the distance travelled into the medium. This phenomenon allows the conversion of an incident linearly polarized beam in an elliptically polarized one, making a birefringent sample bright when placed between cross polarizers. This phenomenon is at the basis of the polarized transmission optical microscopy (PTOM) technique, which will be explained in the following section.

1.4 Polarized Transmission Optical Microscopy

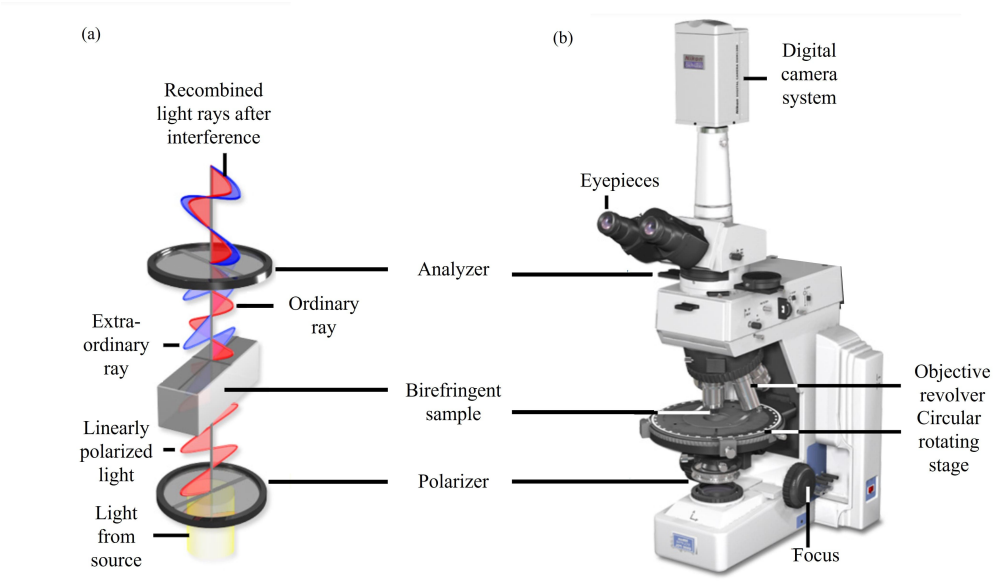

Figure 1.6: (a) Schematics of the principles of polarized transmission optical microscopy (b) Main components of a polarizing microscope. Adapted from[15].

Polarized transmission optical microscopy (PTOM) is a very useful technique for the study of birefringent samples, especially liquid crystals. It consists in adding to a microscope a linear polarizing filter, trivially called "polarizer", after the light source in order to shine onto the sample a linearly polarized radiation and a second one, which can be rotated and called "analyzer", after the sample (see Fig 1.6).

When the two polarizers are crossed, and between them there is no sample or an isotropic liquid, all the light coming from the polarizer is blocked by the analyzer thus producing a black image. However, if a birefringent material is observed, the incident linearly polarized light is converted to elliptically polarized light and, since one of its components is able to pass through the analyzer, a bright image is obtained. The transmitted intensity is:

$$I = I_0 sin^2(2\varphi) sin^2(\frac{\delta}{2}) \tag{1.5}$$

where I_0 is the intensity of the light coming out of the polarizer, δ is the phase difference between the ordinary and the extraordinary rays and φ is the azimuthal angle, the angle between the analyzer and the projection of the optical axis onto the sample plane. When the nematic director is perpendicular to the incoming ligth beam, $n_e - n_o = n_{\parallel} - n_{\perp} = \Delta n$, and thus, combining equations 1.4 and 1.5, the following relation is obtained:

$$I = I_0 sin^2(2\varphi) sin^2(\frac{\pi d \Delta n}{\lambda_0}) \tag{1.6}$$

where λ_0 is the wavelength of the incoming light and d the thickness of the sample. Using this equation is possible to describe, from the first sinus factor, the variations of the transmitted light intensity observed when a birefringent material is continuously rotated between cross polarizers. The second sinus factor is responsible of the different colours observed for anisotropic materials because it quantifies the phase difference between the ordinary and the extraordinary rays in which the incoming light is split when passing through the birefringent sample. These two rays recombine as they leave the material, interfering in a constructive or destructive way, depending on the incoming light wavelength λ_0; if a polychromatic ligth enters the sample, only certain wavelengths (selected by the combination of Δn and d) can constructively interfere, producing a colored image. Since the second sinusoidal term depends on a combination of wavelength, thickness and birefringence, it is possible to create a chart, called Michel-Lévy interference color chart (Fig 1.6), in which these three quantities can be simultaneously represented. Using this chart is then possible to estimate the birefringence of a material once its thickness is known or, vice versa, knowing the Δn of a sample it is possible to calculate its thickness. However most of the images shown in this thesis are taken from samples with high birefringence ($\Delta n \approx 2$) and thickness $> 20\mu m$ thus appearing yellowish, being in a zone far beyond the sixth order.

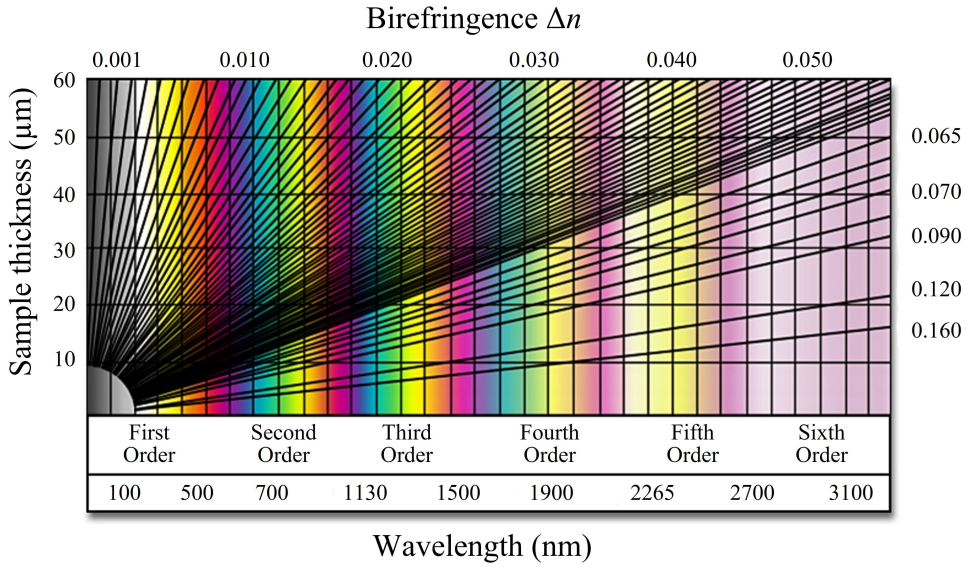

Figure 1.7: Michel-Lévy interference color chart. Adapted from [15].

1.5 Textures and topological defects in nematic liquid crystals

When a thin liquid crystal cell is imaged in a polarizing microscope, various textures and colors appear, depending on the particular phase and orientation of the molecules. These textures, thanks to liquid crystalline birefringence, can provide a large amount of information on the symmetry and the alignment of the mesogens in the sample. PTOM technique, among the several others available for the study of LC materials, can indeed be considered a practical identification method for the different mesophases and a convenient way to determine the structure even in inhomogeneous samples. Smooth features, for example are an indication of a nematic phase, while sharp domain edges are a distinctive sign of the smectic phase. Since in the present thesis the considered material only shows nematic phases, only a description of the nematic textures and defects will be provided.

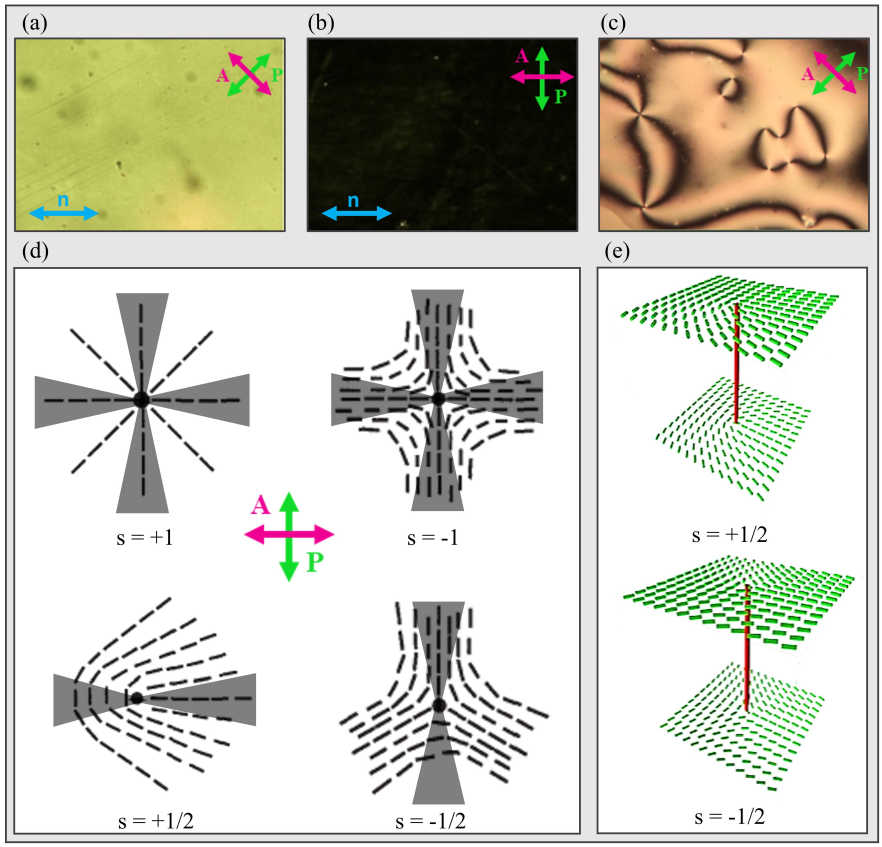

Figure 1.8: (a) Homogeneous planar alignment of the N phase of RM734 in a $20\mu m$-thick cell, with the nematic director **n** oriented at $45°$ respect of the polarizer. (b) Homogeneous planar alignment of the N phase of RM734 in a $20\mu m$-thick cell, with the nematic director **n** parallel to the polarizer. (c) Schlieren texture formed by the N phase of RM734 in a $20\mu m$-thick cell. (d) Structures and strength s of the principal topological defects found in nematics. Black lines represent the nematic director while dark cones represent the dark brushes of the Schlieren texture. (e) Representation as red lines of the disclinations with strength $s = +1/2$ and $s = -1/2$, nematic director is represented as green rods. Panel e is adapted with permission from [16].

When a nematic material is aligned parallel to the cell surfaces and anchoring interactions are strong enough to provide an homogeneous common orientation, a uniform color, depending on thickness and birefringence, is obtained. According to equations 1.5 and 1.6, the transmitted light intensity of a homogeneous nematic sample sinusoidally varies when it is rotated between crossed polarizers, with a maximum intensity when the molecules form an angle of $45°$ with one of the two polarizers (Fig. 1.8a) and a minimum, black state when aligned parallel to one of the polarizers (Fig. 1.8b). If the anchoring interactions are weak and the molecule orientation can gradually vary along the cell the texture is not uniform anymore and the so-called *Schlieren* texture is observed (Fig.1.8c). It appears as a characteristic set of points connected by a series of alternating bright and dark brushes, the latter corresponding to the extinction zones in which the nematic director is parallel to one of the two polarizer. The points, instead, are topological defects in which the direction of the nematic director cannot be unequivocally assigned. Depending on their structure, they can possess two or four dark brushes as represented in Fig. 1.8d; every defect possess a "strength", whose modulus can be easily calculated as $s = n/4$, being n the number of brushes; the sign can be obtained rotating the analyzer, if the brushes rotates in the same direction the sign is considered to be positive, otherwise it is negative. Defects with strength $s = \pm 1/2$ can propagate in the third dimension, as sketched using red lines in Fig. 1.8e, creating thread-like structures which are called defect lines or disclinations which are visible in very thick samples; instead, defects with strength $s = \pm 1$ can "escape" in the third dimension and become non-singular.

Sometimes, cells with particular boundary conditions can create regions with different topologies; if two different topologies get in touch, and molecules cannot continuously joint the two zones, a particular type of defect is formed. This structure, characterized by an abrupt change in topology, is called defect wall and appear as a thin dark line.

As evident in[17], the polar nature of the recently discovered ferroelectric nematic phase N_F, characterized by a common verse and direction of the mesogens and deeply discussed in the next chapter, implies some differences respect of the broadly studied N phase. In N_F phase, for example, defects with $s = \pm 1/2$ cannot exist due to topological continuity requirements, and defects with $s = \pm 1$, which can relax in the third dimension, are uncommon. However, since various twisted and untwisted topology can be created in N_F phase, defect walls, separating domains with different topologies, are relatively common[18–20].

If the nematic material possess homeotropic alignment, that is, perpendicular to the cell plates, the direction of light propagation coincides with the optical axis of the phase. In this case, in the plane of the cell no anisotropy is present and thus the light is extinguished by the analyzer, producing a black image, called pseudo-isotropic texture which can be distinguished from an actual isotropic dark state simply tilting the cell or perturbing the alignment squeezing of the cell.

Bibliography

[1] P.-G. De Gennes and J. Prost. *The physics of liquid crystals*. Oxford University Press, 1993.

[2] D. Dunmur, A. Fukuda, and G. Luckhurst. *Physical Properties of Liquid Crystals Nematics*. The Institution of Electrical Engineers, 2001.

[3] P. Oswald and P. Pieranski. *Nematic and Cholesteric Liquid Crystals - Concepts and physical properties illustrated by experiments*. Taylor & Francis, 2005.

[4] P. Oswald and P. Pieranski. *Smectic and Columnar Liquid Crystals - Concepts and physical properties illustrated by experiments*. Taylor & Francis, 2006.

[5] G. Zanchetta. *PhD Thesis*. Università degli Studi di Milano, 2007.

[6] P. J. Collings and M. Hird. *Introduction to liquid crystals*. Taylor & Francis, 2009.

[7] P. W. Atkins, J. de Paula, and J. Keeler. *Atkins' Physical Chemistry*. Oxford University Press, 2018.

[8] M. Mitov. Cholesteric liquid crystals in living matter. *Soft Matter*, 13:4176–4209, 2017.

[9] G. Chilaya. *Cholesteric Liquid Crystals: Properties And Applications*. LAP Lambert Academic Publishing, 2013.

[10] R. J. Meyer and L. Mcmillan. Simple molecular theory of the smectic c, b, and 0 phases, 1974.

[11] N. A. Clark and M. A. Handschy. Surface-stabilized ferroelectric liquid-crystal electro-optic waveguide switch. *Applied Physics Letters*, 57:1852–1854, 1990.

[12] D. R. Link, G. Natale, R. Shao, J. E. Maclennan, N. A. Clark, E. Korblova, and D. M. Walba. Spontaneous formation of macroscopic chiral domains in a fluid smectic phase of achiral molecules. *Science*, 278:1924–1927, 1997.

[13] H. Bock and W. Helfrich. Two ferroelectric phases of a columnar dibenzopyrene. *Liquid Crystals*, 18:387–399, 1995.

[14] H. Takezoe and F. Araoka. Polar columnar liquid crystals. *Liquid Crystals*, 41:393–401, 2014.

[15] P. C. Robinson and M. W. Davidson. Polarized light microscopy. URL `https://www.microscopyu.com/techniques/polarized-light/polarized-light-microscopy`.

[16] A. Gudimalla, M. Lavrič, M. Trček, S. Harkai, B. Rožič, G. Cordoyiannis, S. Thomas, K. Pal, Z. Kutnjak, and S. Kralj. Nanoparticle-stabilized lattices of topological defects in liquid crystals. *International Journal of Thermophysics*, 41(4):51, Mar 2020.

[17] P. Rudquist. Revealing the polar nature of a ferroelectric nematic by means of circular alignment. *Scientific Reports*, 11, Dec 2021.

[18] X. Chen, E. Korblova, D. Dong, X. Wei, R. Shao, L. Radzihovsky, M. A. Glaser, J. E. Maclennan, D. Bedrov, D. M. Walba, and N. A. Clark. First-principles experimental demonstration of ferroelectricity in a thermotropic nematic liquid crystal: Polar domains and striking electro-optics. *Proceedings of the National Academy of Sciences*, 117:14021–14031, 2020.

[19] O. D. Lavrentovich. Ferroelectric nematic liquid crystal, a century in waiting. *Proceedings of the National Academy of Sciences*, 117(26):14629–14631, 2020.

[20] N. Sebastián, R. J. Mandle, A. Petelin, A. Eremin, and A. Mertelj. Electrooptics of mm-scale polar domains in the ferroelectric nematic phase. *Liquid Crystals*, 48: 2055–2071, 2021.

CHAPTER 2

RM734 and the Ferroelectric Nematic Phase

2.1 Introduction

As presented in Section 1.2.1, the nematic phase (N) is the simplest and most diffused liquid crystalline phase known, in which the mesogens, usually rod-shaped objects, align in a common direction described by the unit vector **n** called the director. The properties of this mesophase, also thanks to its wide use in LCD technology, has been deeply investigated during the last century[1–3]. This phase, even when formed by polar molecules, is apolar; the mesogens, indeed, can align along **n** in a parallel or antiparallel way without any preference. At the beginning of 20th century, Debye[4] and Born[5] theorized the possible existence of a polar nematic phase, which would then possess ferroelectric properties. They hypothesised that this type of molecular ordering could survive if the molecules had an high enough electric dipole p, capable of generating dipole-dipole interactions strong enough to overcome thermal fluctuations. In the following decades, while an experimental proof of the existence of a ferroelectric nematic (N_F) was still missing, some scientist, such as Frank first[6] and Pleiner and Brand later[7], tried to give theoretical explanations to the elusiveness of this particular mesophase. Finally, in 2017, roughly a century after the speculations of Debye and Born, Mandle et al. and Nishikawa et al. independently synthesized two different highly-polar materials (respectively called RM734 and DIO) which showed multiple nematic phases[8] [9]. Even though some stange properties, such as the enormous bulk polarization of the low-temperature nematic phase of DIO, had been observed, it was only in 2020 that Chen et al. demonstrated, for RM734, that this newly discovered nematic phase was indeed ferroelectric[10]. The combination of fluidity with its spontaneous bulk polarization[11], its strong non-linear optical response[12,13] and its unique electro-optical properties[14] makes the study of these materials very interesting for both technological and basic researches[15], in which this work is placed. In this Chapter the N_F will be firstly presented, proceeding, in Section 2.3, with a brief description of RM734 will be given focusing on some of its main chemical features and properties. Lastly a brief comparison between the different ferroelectric nematic mesogens actually known will be presented with an eye on the state-of-the art studies on the molecular basis of the N_F phase.

2.2 The ferroelectric nematic phase

The ferroelectric nematic phase N_F can be considered similar to a conventional nematic phase N in which the equivalence between **n** and **-n** isn't present any more. This is a caused by a polar orientation of the molecules that now, in addition to a common direction, share also a common verse of their molecular dipoles, resulting in a macroscopic spontaneous polarization density P. This property has been firstly measured

by Nishikawa et al. in the low-temperature N phase of DIO (in that time called M_P phase)[9] and later measured and used by Chen et al. to demonstrate the ferroelectricity of RM734[10]. Both groups found an high value of P, which increases once T is decreased, reaching a final value of $\approx 4.5\mu C/cm^2$ for DIO and $\approx 6\mu C/cm^2$ for RM734 (Fig 2.1).

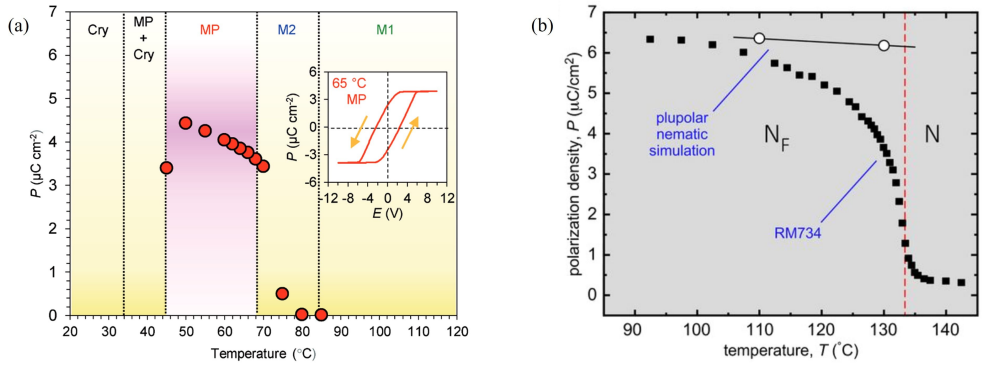

Figure 2.1: (a) Polarization density P of DIO measured on cooling (red circles) reaching the value of $P \approx 4.5\mu C/cm^2$ at the lowest temperatures. MP phase corresponds the ferroelectric nematic phase. The inset represents the P–E hysteresis loop recorded at 65 °C (b) Polarization density P of RM734 measured on cooling (black squares) saturating at $P \approx 6\mu C/cm^2$ at the lowest temperatures. The white circles are values of P calculated from a MD simulation of the N_F phase where the long-range orientation fluctuations are suppressed, giving a P value determined by molecular-scale fluctuations and local packing. RM734 approaches this value at low T. Adapted from[10] under a Creative Commons Attribution 4.0 International License and adapted with permission from[9]

This value is several times higher than the one found into SmC*[16] and into bent-core smectics[17] and comparable to the one of ferroelectric columnar phases[18] and solid ferroelectrics[19]. Since the nematic order parameter, expressed in equation 1.1, cannot highlight the differences between N and N_F phases, the polarization P, normalized over its maximum theoretical value P_M, can be used as a polar nematic order parameter, such as:

$$p = \frac{P}{P_M} \tag{2.1}$$

This parameter is 0 in a conventional nematic phase N while reaches 1 in a perfectly oriented N_F.

Another possible polar order parameter, which relies only on geometric parameters can be defined as:

$$p = \langle cos(\beta_i) \rangle \tag{2.2}$$

where β_i is the angle between each molecular dipole and the local average P direction, while the brackets indicate a spatial and temporal statistical average. For RM734, while entering the N_F phase, this value continuously grows, while reducing T, from $p = 0$ to values up to $p > 0.9$. It may be worth noting that, differently from conventional N phase, cases with $p < 0$ and $p > 0$ do not correspond to physically different states, since it is possible to obtain one from the other simply changing the coordinate system.

The birefringence of RM734 in N_F phase is very high, being $\Delta n = 0.2$, a value comparable with the one of conventional nematics. Another interesting property of the N_F mesophase is a remarkable sensitivity towards electric fields which leads, in combination with the high Δn, to the presence of electro-optic effects with electric field as low as $E \approx 1V/cm$ a value a hundred times smaller in comparison with the other liquid crystals[11,14]. Furthermore this coupling of E with N_F, differently to N, is polar, allowing Chen et al. to demonstrate the ferroelectric nature of this phase upon the selective reorientation of oppositely oriented polar domains using electric fields of different sign[10] (see Fig 2.2).

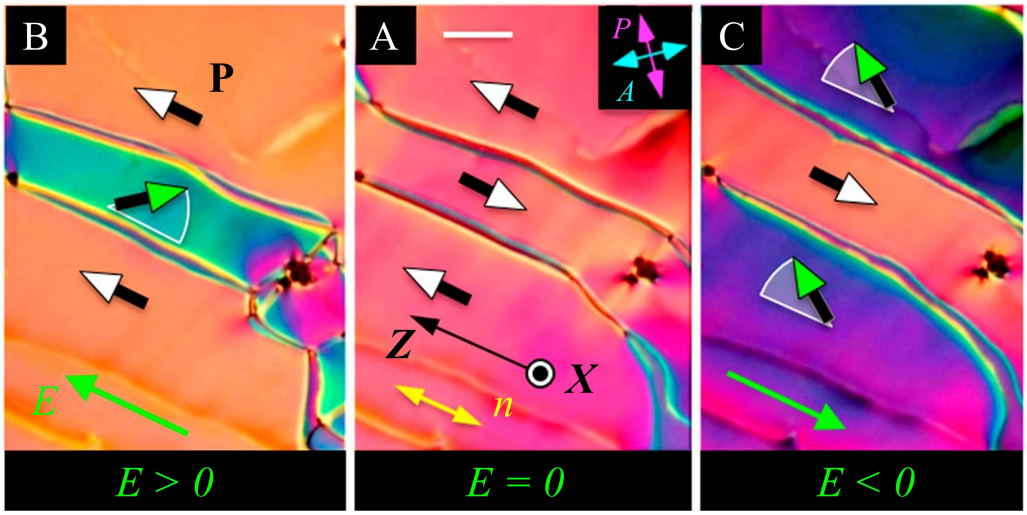

Figure 2.2: PTOM images of electrical reorientation of polar domains in a flat cell filled with RM734 at T = 120 °C. These domains spontaneously forms upon cooling from the N phase to N_F and possess a polarization density P. (a) Field-free initial state showing three domains separated by domain walls, each domain having n along the buffing direction z. (b) Application of an electric field $E = 1V/cm$ inducing an in-plane reorientation of n in the central domain, leaving the upper and lower domains almost unchanged. (c) Application of $E = -1V/cm$ inducing an in-plane reorientation of n in the upper and lower domains. There is little optical change or reorientation in the central domain. When the field is switched back to $E = 0$, the system returns to the starting state (a). Adapted from[10] under a Creative Commons Attribution 4.0 International License

Ferroelectric nematics also exhibit high nonlinear optical susceptibilities, rendering them intriguing candidates for the realization of next-generation electronic and photonic devices[12,13]. For example, RM734 possesses a nonlinear susceptibility of $5.6pm/V$ in the transparent regime, one of the highest values among ferroelectric liquid crystalline materials, making it a very efficient material in optical second-harmonic generation[12]. Ferroelectric nematic phase has also been found in polymeric materials which can be created upon the repetition of the RM734 central unit[20] or upon inserting lateral photopolymerizable groups[21], maybe opening the way towards new advanced materials. Sometimes, non mesogenic molecules can be added to liquid crystalline materials in order to modify their properties; this strategy has also been applied to the N_F phase. When a chiral dopant is added to an N_F material, a chiral version of this mesophase, called helielectric nematic phase (N_F*), can be obtained[22–24]. In this phase the molecules form an helical structure with the polarization vector P continuously rotating along the helix

axis, representing a polar analog of the cholesteric phase N*. This phase preserves the giant dielectric effect of its non-polar counterpart while showing an enhanced non-linear optical response when the helielectric pitch is close to the SHG wavelength[23] or a selective reflection in the visible range which can be fine-tuned using ultra-low electric fields. This chiral phase has also been found in a pure RM734 chiral derivative[25] Nishikawa et al. added a photoisomerizable azobenzene-tethered molecule to a N_F, obtaining a material which can switch between the ferroelectric nematic phase and the antiferroelectric SmZ_A phase; this results in a system with a phototunable dielectric permittivity in a wide range ($200 < \epsilon < 18000$)[26]. The phototrigger, indeed, upon the irradiation with different wavelengths, can be interchanged between a linear, trans- configuration, compatible with the N_F phase and an angled, cis- configuration which force a phase transition to the SmZ_A phase allowing the realization of photo-variable capacitors.

2.3 RM734 and the other archetypal ferroelectric nematics

The mesogen studied in this thesis is 4-[(4-nitrophenoxy)carbonyl]phenyl2,4- dimethoxybenzoate, more commonly known as RM734; this molecule is composed by three phenyl rings held together, in a linear fashion, by carboxylate esters while carrying a nitro group in the para position at one end and two methoxy groups at the other end, respectively in the para and ortho position. This configuration results in a series of different dipoles, roughly oriented in the same direction, summing in a very large molecular dipole of $\sim 11D$. This compound, at room temperature appears as a white crystalline solid with a melting temperature of $\sim 190°C$, entering directly into the N phase and a clearing temperature of $\sim 195°C$. The N_F phase is indeed monotropic, appearing exclusively on cooling; the phase diagram of RM734, obtained in the cooling direction is:

$$\text{Iso} \text{—}195°C\text{—} \text{N} \text{—}133°C \text{—} \text{N}_\text{F} \text{—}70°C \text{—} \text{X}$$

This molecule was the first one to be undoubtedly defined N_F and, together with DIO and UUQU-4-N, can be considered as one of the three archetypal ferroelectric nematic families which started the researches on this peculiar mesophase. While RM734 and DIO are very important being the first ferroelectric nematic discovered, their N_F phases are present at temperatures far beyond RT, hampering their use, as pure compounds, into technological devices; in contrast, UUQU-4-N discovered in 2021 by Manabe et al. has the advantage of a N_F phase stable around $20°C$[27], making it interesting for a technological and commercial use. The structures and cooling phase diagrams of these three molecules are reported in Fig. 2.3

By a simple comparison between these three molecules it is possible to observe that they possess some similarities such as a rigid core consisting in at least three aromatic rings and relatively short alkyl or alkoxy tails. Another common feature is the high molecular dipole moment, which, in combination with a small enough intermolecular distance, has been used by Madhusudana to explain the stability of the ferroelectric nematic phase in the only theoretical model available so far to describe the weakly first-order nature of the N-N_F transition[28].

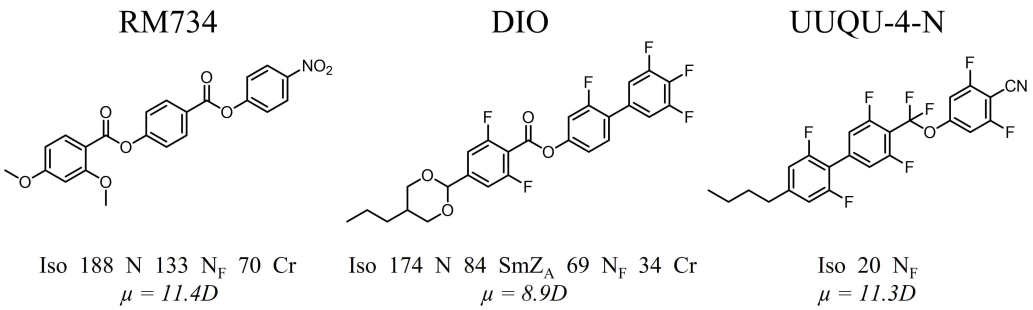

Figure 2.3: Structures, transition temperatures in $°C$ and dipole moments of RM734, DIO and UUQU-4-N

2.4 Effects of structural variations on the ferroelectric nematic phase of RM734

While RM734 has been the first compound to be recognized as N_F, the first mesogen reported to possess an "unknown nematic" N_X phase was the structurally-related molecule RM230 (Fig 2.4) in which the terminal methoxy is replaced by an ethoxy group [8].

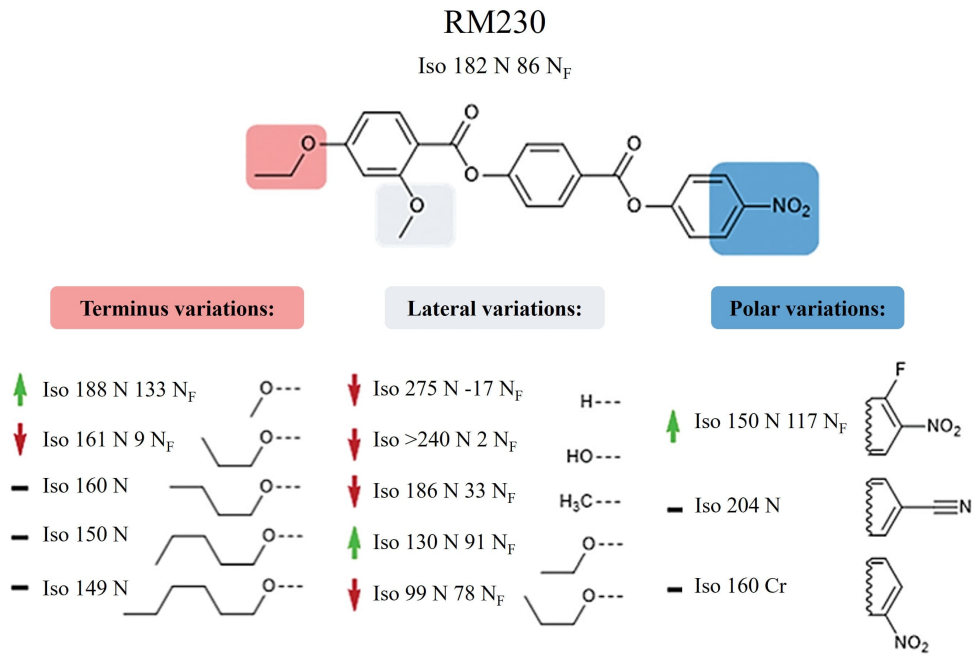

Figure 2.4: Structural variations and transition temperatures in $°C$ of RM230, recorded on cooling from the isotropic phase. Green and red arrows indicates respectively an increase or a decrease of $T_{N\text{-}N_F}$ while a black dash indicates the suppression of the N_F phase. Adapted with permission from [29].

The finding of two distinct nematic phases motivated Mandle et al. to investigate, upon the synthesis of different RM230 variants (among which RM734), the structure-property relationships promoting the occurrence of what today is known to be the N_F phase[29,30]. They started substituting the terminal group, finding that inserting chains longer than the ethoxy the N_F phase was suppressed, while shortening it to a methoxy increased $T_{N\text{-}N_F}$ of $\sim 50°C$. Different substitutions of the lateral methoxy revealed that a large group helped in preventing the crystallization while its removal decreased $T_{N\text{-}N_F}$ by over $50°C$[31]. Moving to the other terminal of the molecule, the addition of a fluorine atom in the ortho position of the nitro group raised $T_{N\text{-}N_F}$ by over $30°C$, while reducing the dipole inserting a nitrile group in place of the nitro group prevents the formation of the N_F phase; this same effect is obtained changing the orientation of the dipole replacing the 4-nitrophenyl unit with its 3-nitro isomer.

Due to its importance in the field, further structure-property relationships studies have been performed by different groups using RM734 as parent material, as shown in Fig 2.5.

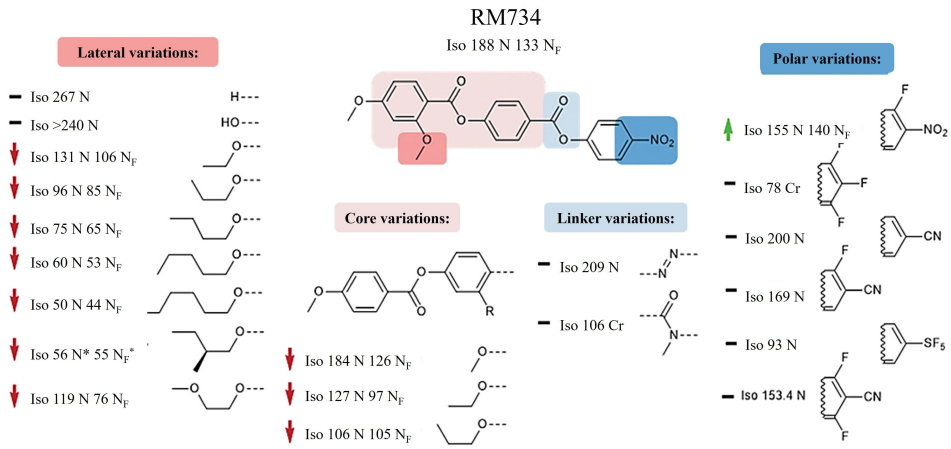

Figure 2.5: Structural variations and transition temperatures in $°C$ of RM734, recorded on cooling from the isotropic phase. Green and red arrows indicates respectively an increase or a decrease of $T_{N\text{-}N_F}$ while a black dash indicates the suppression of the N_F phase. Adapted with permission from[29].

From these new synthesis emerged that other terminal polar units, when the nitro group is missing, are suppressing the N_F phase. Other bulky lateral groups have been tested as well, confirming that longer lateral chains help in lowering $T_{N\text{-}N_F}$ together with melting and clearing points; among them the chiral (S)-2-methylbutoxy group promoted the formation of the N_F* phase, without the addition of any external dopant[23,25]. Some variations on the core group have been tested[31], finding that moving the lateral group to the central ring do not eliminate the N_F phase and only slight reductions of the transition temperatures are achieved. Ester linkers have also been proved fundamental to retain the N_F phase; indeed, when they are replaced with azo or n-methylamide linking units the ferroelectric nematic phase is suppressed.

Other works focused onto the fluorination of RM734, showing again that, when a fluorine is inserted in ortho to the nitro group, $T_{N\text{-}N_F}$ is increased while $T_{Iso\text{-}N}$ is decreased[30].

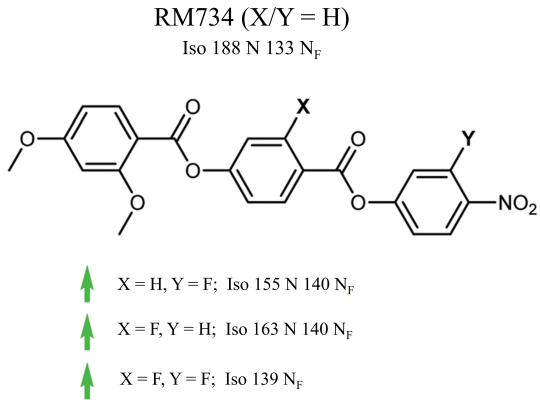

Figure 2.6: Structural variations and transition temperatures in $^{\circ}C$ of fluorinated derivatives of RM734, recorded on cooling from the isotropic phase. Green and red arrows indicates respectively an increase or a decrease of $T_{N\text{-}N_F}$ while a black dash indicates the suppression of the N_F phase. Adapted with permission from [29].

When a fluorine atom is inserted in the 3-position of the central ring a new compound, called RT11001, is obtained whose spontaneous polarization, with a value of $6.9\mu C/cm^2$, is the largest ever recorded for a liquid crystalline material [32]. When both this fluorinations are intrduced simultaneously the nematic phase is suppressed resulting in a compound that exhibits a direct isotropic to N_F phase transition [33].

Further researches have been performed onto a RM734 derivative, with a 4-cyano-3,5-difluoro polar end and called RM734-CN(2F), a molecule which doesn't show N_F phase.

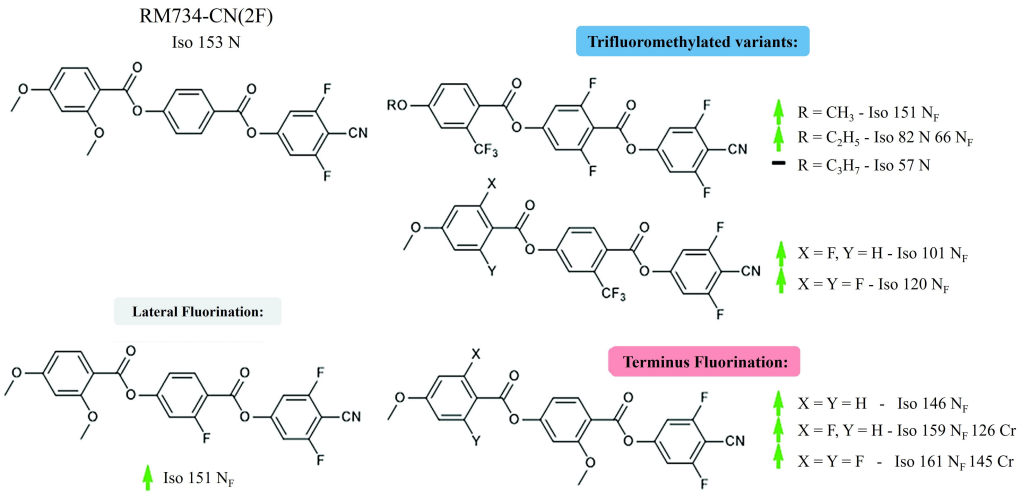

Figure 2.7: Structural variations and transition temperatures in $^{\circ}C$ of structural variants of RM734-CN(2F), recorded on cooling from the isotropic phase. Green and red arrows indicates respectively an increase or a decrease of $T_{N\text{-}N_F}$ while a black dash indicates the suppression of the N_F phase. Adapted with permission from [29].

Upon the insertion of several fluorine atoms into different positions and upon the replacement of the lateral methoxy with a trifluoromethyl group the ferroelectric phase is reestablished. Again, increasing the length of the terminal alkoxy chain, the N_F phase is destabilized, disappearing for groups longer than the ethoxy[34].

Analogous studies have been performed on DIO molecule[31,34], whose dipole arises from the combination of a 1,3-dioxane ring, a carboxylate ester, and aromatic fluorination pattern; however, since this thesis will only focus on RM734, these works will not be treated in the present section.

Finally, new classes of N_F materials, usually highly fluorinated and rigid molecules, have also been discovered, such as the aforementioned UUQU-4-N[27] family or the LC1 family[35], not presented.

2.5 Computational analysis and discussion

Even though molecular substitutions provide precious clues on the stability of the N_F phase, a detailed description of the mechanisms guiding its formation is still missing. However, molecular dynamics atomistic simulations have been realized[10,36], trying to unravel the mystery behind the appearance of this mesophase. Both groups used a similar approach, differing only in the force field (APPLE&P[10] vs GAFF-LCFF[36]), simulation times ($20ns$[10] vs $250ns$[36]) and the dimensions of the simulated boxes (384 molecules contained[10] vs 680[36]), while both applied periodic boundary conditions and NTP equilibration. $P = 1atm$ has been fixed and various T, spanning the N and N_F phases, have been used. Mandle et al., together with RM734, simulated also RM734-CN, a molecule non displaying the N_F phase. Two different starting conditions have been probed: a polar configuration (POL) in which the molecules are perfectly ordered along the $+z$ direction and a non polar (NONPOL) one in which half of the molecules are aligned along $+z$ and the other half along $-z$. These two configurations are the extreme situation of order and disorder but can be considered a good approximation to the real system because if these simulations are used to evaluate $\mathbf{P}$ a value very similar to the one measured for RM734 at low T is obtained, indicating that the simulated POL state is closely resembling the actual ordering of the mesogens.

Fig. 2.8a-b represent the positional pair correlation functions $g_P(\rho, z)$ and $g_{NP}(\rho, z)$ obtained by the two groups, for both the POL and the NONPOL configurations, with the second being the sum of $g_{NP}^{par}(\rho, z)$ and $g_{NP}^{anti}(\rho, z)$, which are the correlations between molecular pairs with parallel or antiparallel orientation of their molecular axes. These functions, being φ-average conditional probability densities of molecular centers, calculated around a RM734 molecule, which is centred at the origin and aligned along z, are uniaxially symmetric in cylindrical (ρ,φ,z) coordinates, just like N and N_F phases. Furthermore they have a molecule-shaped, low-density zone near the origin because of steric repulsion preventing overlapping of molecules and peaks representing preferred modes of packing with neighbouring molecules. For the sake of brevity, only the peaks of POL configurations will be treated, a complete treatment of the simulation, together with computational details are present in the cited articles.

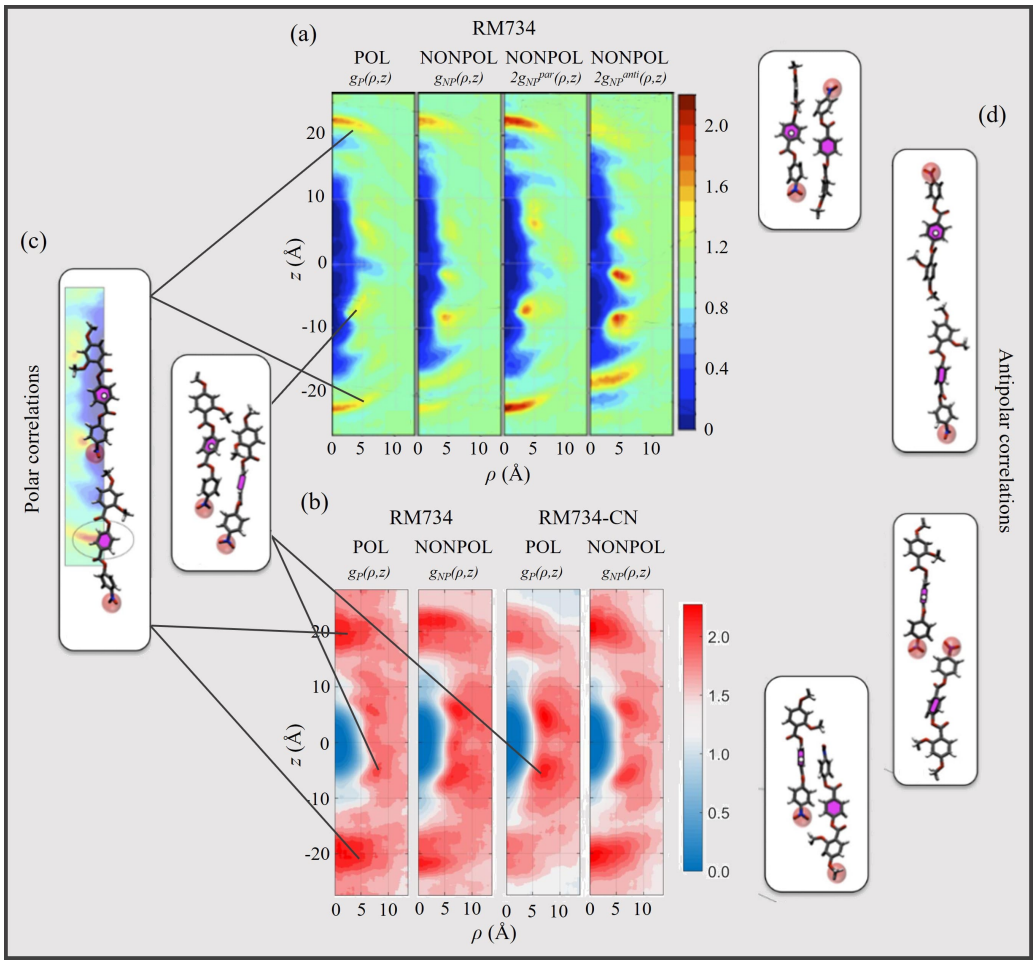

Figure 2.8: (a) Positional pair correlation functions obtained by atomistic MD simulations on RM734 molecule performed by Chen et al.[10], starting from a polar (POL) and a non-polar (NONPOL) configuration, showing the dominant pair correlations adopted by molecules in the two states. (b) Positional pair correlation functions obtained by atomistic MD simulations on RM734 and RM734-CN molecules performed by Mandle et al.[36], starting from a polar (POL) and a non-polar (NONPOL) configuration, showing the dominant pair correlations adopted by molecules in the two states. (c) Representation of the possible polar correlations found in simulations, with lines indicating the corresponding peaks. (d) Representation of the possible antipolar correlations found in simulations, non trated in the present thesis. Adapted from[10,36] under a Creative Commons Attribution 4.0 International License

The peaks at $z \approx \pm 22\mathring{A}$ found by both groups, show that, in the POL configuration, RM734 molecules tends to pair in a head-to-tail fashion (as represented in Fig. 2.8c, left panel); this interaction seems to be much weaker in RM734-CN, in which the substitution of the terminal nitro group of RM734 with a cyano group suppress the N_F phase, suggesting that this type of interaction may be fundamental for the stability of the polar order in the ferroelectric nematic phase. The off-axis peaks found at $\rho \approx z \approx 6\mathring{A}$ indicate a polar side-by-side association (Fig. 2.8c, right panel), probably resulting from specific electrostatic interactions between positive and negative charged groups along

the molecule. These interactions plays a fundamental role in preventing the antiparallel association of the molecular dipoles, stabilizing the polar order in N_F phase. RM734-CN shows similar, but sharper and stronger peaks which indicate the presence of staggered parallel pairing of molecules, supported by CN-C(O)O interactions, which is preferred to the head-to-tail configuration adopted by RM734 induced by the interaction between the terminal methoxy ant the nitro group.

In conclusion, combining the observations obtained by functional groups substitution[8,29–35] on N_F mesogens and atomistic MD simulations[10,36], it appears that the ferroelectric nematic phase requires a combination of different molecular features to be stabilized over the conventional non-polar nematic phase. First of all, mesogens requires a very high value of molecular dipole, in the order of $\sim 10D$, usually obtained as the sum of different smaller dipoles distributed along the molecule. A second requirement is the presence of strong electronegative groups on one terminal and a short alkyl chain on the other to favour the head-to-tail aggregation observed in MD simulations. Transversal dipoles are also fundamental to provide the side-by-side interactions needed to prevent the antiparallel orientation of molecular dipoles and provide short intermolecular distances required in the only theoretical model currently available[28].

Even though these observations provide a lot of clues to understand the N_F phase stability, a complete comprehension of the mechanisms underlying its formation are still missing and further theories and experiments are still required.

Bibliography

[1] D. Dunmur, A. Fukuda, and G. Luckhurst. *Physical Properties of Liquid Crystals Nematics*. The Institution of Electrical Engineers, 2001.

[2] P. Oswald and P. Pieranski. *Nematic and Cholesteric Liquid Crystals - Concepts and physical properties illustrated by experiments*. Taylor & Francis, 2005.

[3] M. Bremer, P. Kirsch, M. Klasen-Memmer, and K. Tarumi. The tv in your pocket: Development of liquid-crystal materials for the new millennium. *Angewandte Chemie - International Edition*, 52:8880–8896, 8 2013.

[4] P. Debye. Einige resultate einer kinetischen theorie der isolatoren. *Phys. Z.*, 13: 97–100, 1912.

[5] M. Born. Über anisotrope flüssigkeiten. versuch einer theorie der flüssigen kristalle und des elektrischen kerr-effekts in flüssigkeitenn. *Sitzungsber. Preuss. Akad Wiss.*, 30:614–650, 1916.

[6] F. C. Frank. Liquid crystals: On the theory of liquid crystals. *Discussions of the Faraday Society*, 25:19–28, 1958.

[7] H. Pleiner and H. R. Brand. Spontaneous splay phases in polar nematic liquid crystals. *Europhysics Letters*, 9(3):243, jun 1989.

[8] R. J. Mandle, S. J. Cowling, and J. W. Goodby. A nematic to nematic transformation exhibited by a rod-like liquid crystal. *Physical Chemistry Chemical Physics*, 19:11429–11435, 2017.

[9] H. Nishikawa, K. Shiroshita, H. Higuchi, Y. Okumura, Y. Haseba, S. I. Yamamoto, K. Sago, and H. Kikuchi. A fluid liquid-crystal material with highly polar order. *Advanced Materials*, 29, 11 2017.

[10] X. Chen, E. Korblova, D. Dong, X. Wei, R. Shao, L. Radzihovsky, M. A. Glaser, J. E. Maclennan, D. Bedrov, D. M. Walba, and N. A. Clark. First-principles experimental demonstration of ferroelectricity in a thermotropic nematic liquid crystal: Polar domains and striking electro-optics. *Proceedings of the National Academy of Sciences*, 117:14021–14031, 2020.

[11] X. Chen, E. Korblova, M. A. Glaser, J. E. Maclennan, D. M. Walba, and N. A. Clark. Polar in-plane surface orientation of a ferroelectric nematic liquid crystal: Polar monodomains and twisted state electro-optics. *Proceedings of the National Academy of Sciences*, 118, 2021.

[12] C. L. Folcia, J. Ortega, R. Vidal, T. Sierra, and J. Etxebarria. The ferroelectric nematic phase: an optimum liquid crystal candidate for nonlinear optics. *Liquid Crystals*, 49 (6):899–906, 2022.

[13] J. Ortega, C. L. Folcia, J. Etxebarria, and T. Sierra. Ferroelectric chiral nematic liquid crystals: new photonic materials with multiple bandgaps controllable by low electric fields. *Liquid Crystals*, pages 1–9, 2022.

[14] N. Sebastián, R. J. Mandle, A. Petelin, A. Eremin, and A. Mertelj. Electrooptics of mm-scale polar domains in the ferroelectric nematic phase. *Liquid Crystals*, 48: 2055–2071, 2021.

[15] O. D. Lavrentovich. Ferroelectric nematic liquid crystal, a century in waiting. *Proceedings of the National Academy of Sciences*, 117(26):14629–14631, 2020.

[16] M. Lallart. *Ferroelectrics - Physical Effects*. IntechOpen, 2011.

[17] Y. Shen, T. Gong, R. Shao, E. Korblova, J. E. Maclennan, D. M. Walba, and N. A. Clark. Effective conductivity due to continuous polarization reorientation in fluid ferroelectrics. *Phys. Rev. E*, 84:020701, Aug 2011.

[18] H. Takezoe and F. Araoka. Polar columnar liquid crystals. *Liquid Crystals*, 41:393–401, 2014.

[19] N. Izyumskaya, Y. Alivov, and H. Morkoç. Oxides, oxides, and more oxides: High-$\varkappa$ oxides, ferroelectrics, ferromagnetics, and multiferroics. *Critical Reviews in Solid State and Materials Sciences*, 34(3-4):89–179, 2009.

[20] J. Li, R. Xia, H. Xu, J. Yang, X. Zhang, J. Kougo, H. Lei, S. Dai, H. Huang, G. Zhang, F. Cen, Y. Jiang, S. Aya, and M. Huang. How far can we push the rigid oligomers/polymers toward ferroelectric nematic liquid crystals? *Journal of the American Chemical Society*, 143:17857–17861, 10 2021.

[21] S. Dai, J. Li, J. Kougo, H. Lei, S. Aya, and M. Huang. Polar liquid crystalline polymers bearing mesogenic side chains with large dipole moment. *Macromolecules*, 54: 6045–6051, 7 2021.

[22] H. Nishikawa and F. Araoka. A new class of chiral nematic phase with helical polar order. *Advanced Materials*, 33, 9 2021.

[23] X. Zhao, J. Zhou, J. Li, J. Kougo, Z. Wan, M. Huang, and S. Aya. Spontaneous helielectric nematic liquid crystals: Electric analog to helimagnets. *PNAS*, 118, 2021.

[24] C. Feng, R. Saha, E. Korblova, D. Walba, S. N. Sprunt, and A. Jákli. Electrically tunable reflection color of chiral ferroelectric nematic liquid crystals. *Advanced Optical Materials*, 9, 11 2021.

[25] D. Pociecha, R. Walker, E. Cruickshank, J. Szydlowska, P. Rybak, A. Makal, J. Matraszek, J. M. Wolska, J. M. Storey, C. T. Imrie, and E. Gorecka. Intrinsically chiral ferronematic liquid crystals: An inversion of the helical twist sense at the chiral nematic – chiral ferronematic phase transition. *Journal of Molecular Liquids*, 361, 9 2022.

[26] H. Nishikawa, K. Sano, and F. Araoka. Anisotropic fluid with phototunable dielectric permittivity. *Nature Communications*, 13, 12 2022.

[27] A. Manabe, M. Bremer, and M. Kraska. Ferroelectric nematic phase at and below room temperature. *Liquid Crystals*, 48:1079–1086, 2021.

[28] N. V. Madhusudana. Simple molecular model for ferroelectric nematic liquid crystals exhibited by small rodlike mesogens. *Physical Review E*, 104, 7 2021.

[29] R. J. Mandle. A new order of liquids: polar order in nematic liquid crystals. *Soft Matter*, 18:5014–5020, 6 2022.

[30] R. J. Mandle, S. J. Cowling, and J. W. Goodby. Rational design of rod-like liquid crystals exhibiting two nematic phases. *Chemistry - A European Journal*, 23:14554–14562, 10 2017. doi: 10.1002/chem.201702742.

[31] J. Li, H. Nishikawa, J. Kougo, J. Zhou, S. Dai, W. Tang, X. Zhao, Y. Hisai, M. Huang, and S. Aya. Development of ferroelectric nematic fluids with giant dielectricity and nonlinear optical properties. *Science Advances*, 7:5047–5068, 2021.

[32] R. Saha, P. Nepal, C. Feng, M. S. Hossain, M. Fukuto, R. Li, J. T. Gleeson, S. Sprunt, R. J. Twieg, and A. Jákli. Multiple ferroelectric nematic phases of a highly polar liquid crystal compound. *Liquid Crystals*, pages 1–13, 2022.

[33] S. Brown, E. Cruickshank, J. M. Storey, C. T. Imrie, D. Pociecha, M. Majewska, A. Makal, and E. Gorecka. Multiple polar and non-polar nematic phases. *ChemPhysChem*, 22:2506–2510, 12 2021.

[34] J. Li, Z. Wang, M. Deng, Y. Zhu, X. Zhang, R. Xia, Y. Song, Y. Hisai, S. Aya, and M. Huang. General phase-structure relationship in polar rod-shaped liquid crystals: Importance of shape anisotropy and dipolar strength. *Giant*, 11, 8 2022.

[35] Y. Song, J. Li, R. Xia, H. Xu, X. Zhang, H. Lei, W. Peng, S. Dai, S. Aya, and M. Huang. Development of emergent ferroelectric nematic liquid crystals with highly fluorinated and rigid mesogens. *Physical Chemistry Chemical Physics*, 24:11536–11543, 4 2022.

[36] R. J. Mandle, N. Sebastián, J. Martinez-Perdiguero, and A. Mertelj. On the molecular origins of the ferroelectric splay nematic phase. *Nature Communications*, 12(1):4962, Aug 2021.

Part II

Surface alignment of RM734

CHAPTER 3

Surface alignment of RM734

3.1 Introduction

In a nematic liquid crystal the local tendency for coherent orientation is strong enough to induce a long-range order, manifested by elastic energy coupled with spatial gradients of the orientational field. The spatial uniformity is stabilized, in absence of external forces, only by elastic contributions so that an arbitrarily small applied electric or magnetic field can reorient a bulk nematic sample by coupling to nematic orientation via quadrupolar anisotropy. The N ordering, for the same reasons, is highly responsive towards boundary conditions, such as surfaces realized in order to favour a specific molecular orientation. These conditions, thanks to the fluidity of the N phase, allow to fill a container with a nematic liquid and have it spontaneously adopt a space-filling, three-dimensional (3D) orientational structure. Most of the technologies based on N LCs exploit a combination between high responsivity to applied fields and boundary conditions creating surface-induced 3D structures which respond in a predictable way to external fields. This highlights the importance of understanding and controlling surface and field interactions to find new LCs applications.

After the recent discovery of the ferroelectric nematic phase of RM734 [1–3] and DIO [4], whose enormous spontaneous polarization ($P \sim 6\mu C/cm^2$) [5] and polar linear coupling with external electric fields $\mathbf{E}$ translates into electro-optic responses to fields as small as $\mathbf{E} \sim 1V/cm^2$ [6], a better understanding of its interactions with different boundary conditions is required.

In this chapter the surface alignment of the N_F phase of RM734, induced by various rubbed and unrubbed substrates, is presented demonstrating that confining surfaces exert a strong influence on the formation of different orientational patterns and domains. It is furthermore shown that the polar ordering appearing at the N–N_F phase transition changes the interactions of the director $\mathbf{n}$ with bounding surfaces and it is demonstrated that by designing the polarity of the 2D bounding surfaces, it is possible to control the 3D structuring of the macroscopic electric polarization $\mathbf{P}(r)$ in the N_F phase, a fundamental aspect of LC science and technology. In the simplest example, if the orientation of the preferred polarization is vectorially unidirectional on the confining surfaces, then the N_F volume polarization can be similarly oriented, that is, poled into a uniform orientation by the surfaces without the need for an applied field.

3.2 Materials and methods

3.2.1 Materials

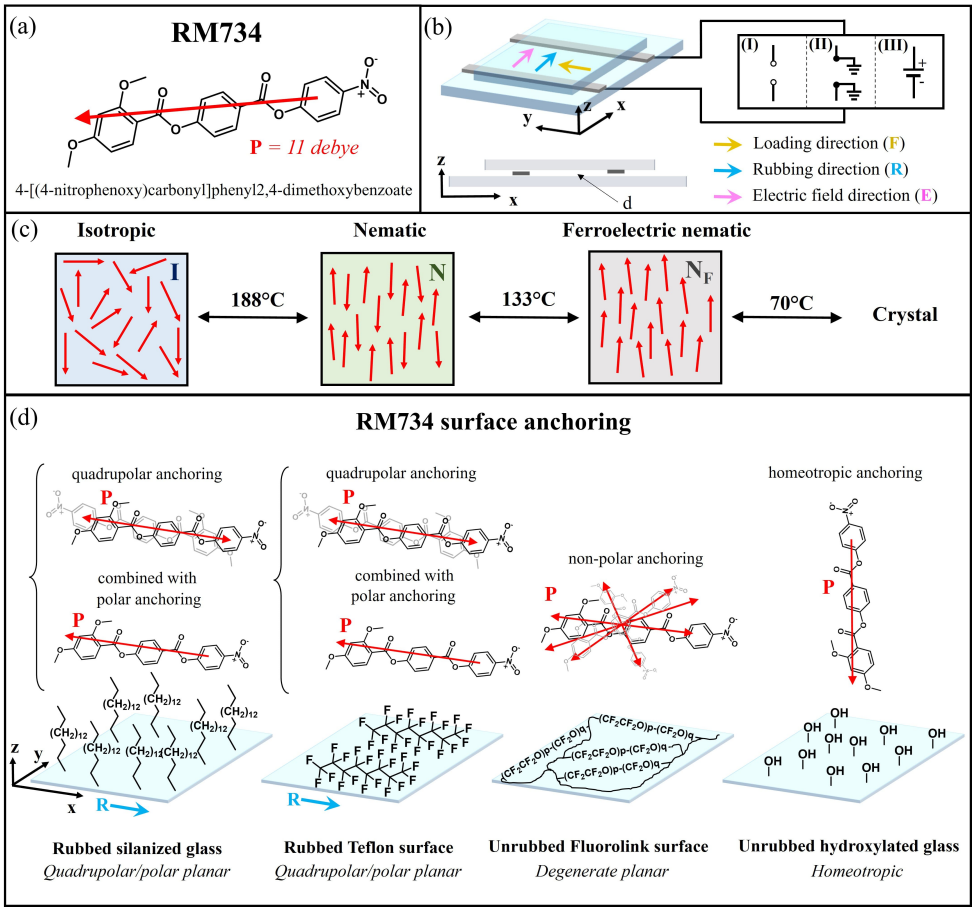

Figure 3.1: (a) Molecular structure and molecular dipole of RM734. (b) Sketch of thin cells formed by two planar slabs held at a distance d by spacers and provided of electrodes. Arrows represent the relevant directions (**F**, **R**, **E**) used to describe the results and the three electrodes configurations used in the experiments: (I) floating, (II) grounded, (III) connected to a function generator. (c) Sketches of the three liquid phases of RM734 and transition temperatures upon cooling from isotropic (d) Sketches of the four surfaces studied in this work and of the orientation of the RM734 molecules with respect to the substrates.

The studied flat cells are realized by two flat glass plates held by spacers at a distance $d = 10\mu m$ or $d = 18\mu m$ and filled by capillarity with RM734 in the N phase at $180°C$. Cells have electrodes with inter-electrode distances between 2 and $5mm$ and are made of aluminium or ITO; this configuration allows the application of in-plane electric fields. The structure of the cell and the three possible electrode configurations used in the experiments (floating, grounded or connected) are schematized in Fig. 3.1b. Floating configuration is realized leaving the electrodes detached from any instrumentation and suspended to avoid the contact with surfaces, grounded configuration is obtained con-

necting both electrodes to ground while connected configuration is achieved connecting them to a function generator. The different cells are prepared through various surface treatments and some of them are mechanically brushed in a specific direction, an operation called rubbing. Therefore the are four relevant vectorial direction used to describe a cell and its behaviour: the polarization direction ($\mathbf{P}$, with unit vector $\mathbf{u}_P$), the electric field direction ($\mathbf{E}$, $\mathbf{u}_E$), the rubbing direction ($\mathbf{R}$, $\mathbf{u}_R$), and the loading direction ($\mathbf{F}$, $\mathbf{u}_F$), providing the direction of the shear flow when the cell is loaded. Cell with rubbed surfaces are constructed in order to share $\mathbf{u}_R$ on both sides and in the same direction of the applied electric field $\mathbf{E}$. In this work four different surfaces (see Fig 3.1d) were considered, whose preparation is realized as follows.

3.2.2 Preparation of rubbed C16 silanized surfaces

C16 silanized surfaces are glass plated covered with hexadecyl aliphatic chains, grafted through covalent bonds. To realize this modification a $5\%\ v/v$ solution of water in ethanol is acidified up to pH 4.5-5.5 with acetic acid. The reactive hexadecyltrimethoxysilane (HDTMS) is added under mild stirring to the solution to achieve a concentration of $2\%\ v/v$ and let react for 5 minutes at room temperature. Using a pipette, the silane solution is poured on tilted glass plates in order to uniformly wet the surface. Glass slides, once the solvent is evaporated, are heated onto a heating plate at $110°C$ for 10 minutes and let to rest at room temperature until the next day. Glass plates are then brushed in the same direction of the silane solution flow using optical paper wetted with ethanol, which also remove unreacted HDTMS residues present.

3.2.3 Preparation of rubbed Teflon surfaces

To prepare rubbed Teflon surfaces clean glass plates are fixed upon a heating plate and heated at $140°C$. A round Teflon bar is then lean against the glass and, once hot, rubbed with a constant speed of $2mm/s$. The slides are then slowly cooled to room temperature before cell assembling.

3.2.4 Preparation of unrubbed Fluorolink surfaces

Unrubbed Fluorolink surfaces are coated by a photocured perfluoropolyether polymer composed by the precursor Fluorolink MD700 and photoinitiator IRGACURE 651. IRG651 is dissolved into a tiny amount of $CHCl_3$, then MD700 is added into a ratio of initiator over monomer of $2\%\ w/w$ and the resulting solution is further diluted with $CHCl_3$ to achieve a final concentration of $25\%\ v/v$ of MD700 in chloroform. Glass plates are carefully cleaned with acetone and air flow to remove any trace of dust and the monomer mixture is spin-coated at a speed of $3000rpm$, letting the solvent evaporate while spinning for 2 minutes. The resulting thin film is photopolymerized under a UV lamp in a nitrogen atmosphere for 40 minutes.

3.2.5 Preparation of unrubbed hydroxylated glass surfaces

Hydroxylation is obtained by soaking the glass plates into piranha solution for 90 minutes. Piranha solution is prepared by slowly adding one volume of $35\%\ v/v$ hydrogen peroxide to three volumes of sulphuric acid under mild stirring. The plates are then rinsed three times with deionized water and once with methanol prior to air drying. Cells are assembled and filled immediately in order to avoid deterioration of the treated surfaces.

3.2.6 Cell characterization

Cells were characterized by observations at Polarized Transmission Optical Microscopy (PTOM) at various temperatures, and in particular in the N phase at $T = 180°C$ and in the N_F phase at $T = 130°C$. Birefringence was measured for planar samples using a Berek compensator, yielding $\Delta n = 0.20$ in N phase and $\Delta n = 0.23$ in N_F phase. N_F phase was usually obtained cooling cells from N phase leaving the two electrodes floating; a procedure called *zero field cooling* (ZFC). The electric field response of N_F was studied both: by applying the field to the N_F phase of ZFC cells and by applying the field in the N phase and cooling the system into the N_F phase while keeping the field on across the transition (*field cooling*, FC). The FC procedure was introduced to investigate if the polar coupling of $\mathbf{E}$ with the N_F pretransitional fluctuations – at the same time responsive and free to rotate – influences the surface anchoring as the N_F ordering extends throughout the cell.

3.3 Experimental results

In this section the dependence of the textures and the response to electric fields of the N_F phase of RM734 on the confinement type will be presented, with a behaviour strongly influenced by the lower symmetry of N_F respect to N. Being $\mathbf{n} \neq -\mathbf{n}$ the ferroelectric phase shows topological defects and domain walls that cannot be seen in conventional nematics; this non-equivalence is evident in the coupling with the surfaces since, on top of the quadrupolar coupling with $\mathbf{n}$, an additional polar anchoring, with a strength depending on the substrate and its treatment, can be present, as summarized in Fig.3.1d for the four different substrates. For example unrubbed Fluorolink can induce a planar alignment of the N_F phase of RM734 without any polar or quadrupolar coupling while rubbed teflon and C16 silanized glass, whose are still inducing a planar alignment, provide a combination of strong quadrupolar anchoring ($\mathbf{n} = \pm\mathbf{u}_R$) and a polar anchoring (surface $\mathbf{u}_P = -\mathbf{u}_R$. The effects of the broken symmetry are even more evident during the N-N_F transition where the changes in textures in the two phases are accompanied by a sudden appearance of topological defects. The most evident transition is appearing in the hydroxyated glass cells in which a conversion from homeotropic (non-polar) anchoring in the N phase to random planar coupling in the N_F phase is observed.

3.3.1 Rubbed C16 silanized cells

While is generally known that aliphatic silane-coated surfaces induce homeotropic ordering of thermotropic nematics[7], in the case of RM734 a planar alignment is favoured both in N and N_F phases, which can be oriented in any direction by gentle surface rubbing. This is shown in Fig 3.2 shows PTOM pictures demonstrating that the N phase exhibits a good homogeneous planar alignment in the direction of rubbing, both right after cell filling (Fig. 3.2a) and when the N phase is obtained on heating from the N_F phase (Fig. 2b). Upon ZFC to the N_F phase, the overall homogeneous alignment is retained while several domains appear while (Fig. 3.2c). These domains are twisted regions connecting surfaces of reversed polarity, as it is revealed by tilting the analyzer clockwise (lower left panel) and counter-clockwise (lower right panel), revealing regions where the N–N_F transition leads to a surface polarity which is parallel to rubbing but with a reversed direction. This indicates both a rubbing-induced strong quadrupolar anchoring along the whole surface and a weaker polar surface coupling, which is occasionally reverted.

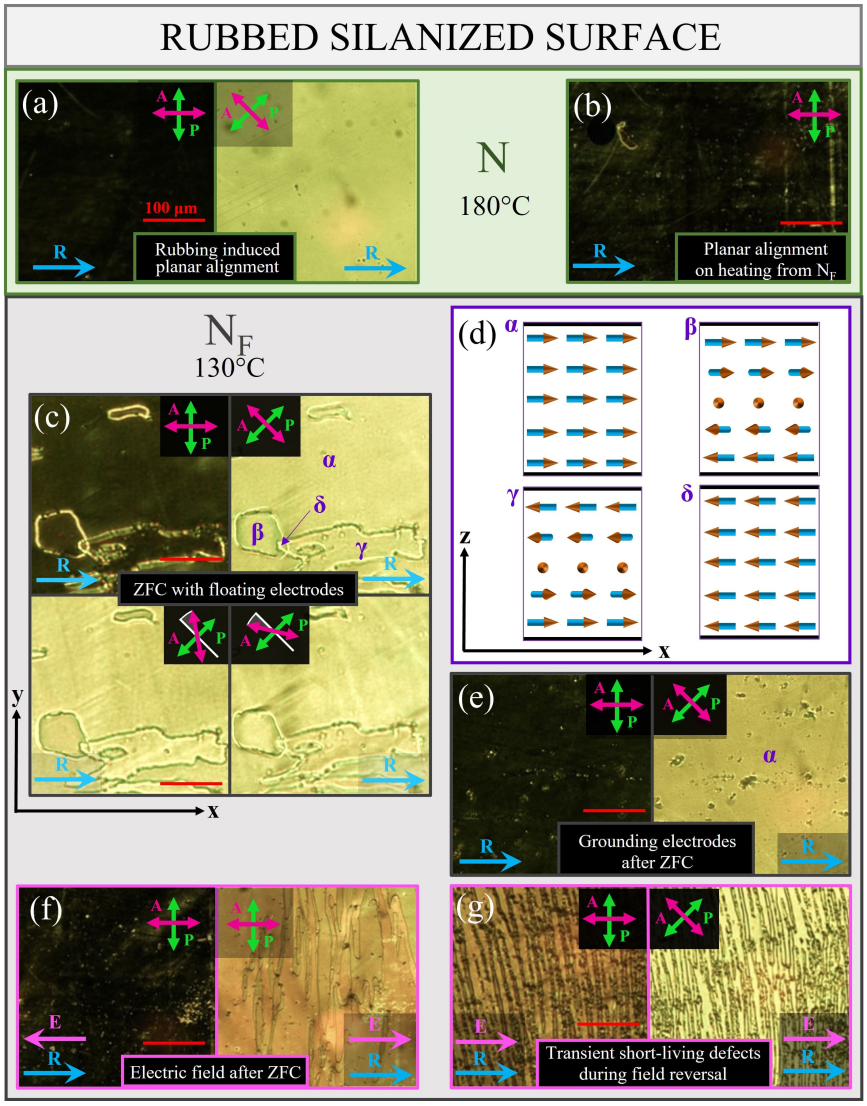

Figure 3.2: Polarized transmission optical microscopy images of 18 mm thick RM734-filled cells having rubbed C16 silanized surfaces. Arrows: rubbing direction (**R**), analyzer (**A**), polarizer (**P**), electric field (**E**). Shadings: nematic phase (green), ferroelectric nematic phase (grey). (a) Cells filled in N phase exhibit planar alignment. (b) Planar alignment is also found after heating from the N_F phase. (c) On *zero field cooling* (ZFC) from N phase the planar alignment is retained except for domains where the surface polarity is reversed (upper panels). Opposite surface polarity induces a twist pattern,as revealed by rotating the analyzer clockwise (lower left panel) and counterclockwise (lower right panel). (d) Sketches of the alignment of the domains marked by α-δ letters across the xz cut of the cell. Domains observed on cooling with floating electrodes (c) disappear when the electrodes are grounded (e). Electric field effects on N_F phase (pink frames). (f), left panel: applying a $1V/cm$ field opposite to **R** ($\mathbf{u}_E = \mathbf{u}_R$), the N_F phase is stabilized and twisted domains disappears. Right panel: As the same field is applied along **R** ($\mathbf{u}_E = \mathbf{u}_R$) a twisted state is induced. (g) Transient short living defect lines appear right after inverting the field. The value of the scale bar is the same in every panel.

The combination of different polar alignment on two different surfaces leads to four different possible regions which are marked with Greek letters in Fig 3.2c and sketched in FIg 3.2d. Regions α and δ are uniformly aligned in opposite directions, while β and γ are twisted (with either right or left-handed rotation) because one surface or the other has reversed polarity. Since the birefringence is high the $18\mu m$ cell is thick enough to enter the Mauguin regime, the adiabatic rotation produces with a nearly identical polarization state of the light for both the twisted and the uniform regions. To confirm this idea some thinner cells have been produced in order to have a shorter twist, and then an incomplete rotation, as shown in Fig 3.3.

While lowering the temperature, the N_F phase appears locally in multiple locations in the cell. When these come into contact with the surfaces, the surface polarity is locally locked by the quadrupolar anchoring, thus producing a twisted structure when such locked polarity is opposite on two facing surfaces. These type of domains, however, are present only in a minor fraction of the cell, suggesting that the surface is exerting a polar coupling with the ferroelectric order parameter p. The stability of these twisted domain, involving both an elastic penalty caused by the distortion of the director and an electric penalty arising from the polarization charges, is not trivial.

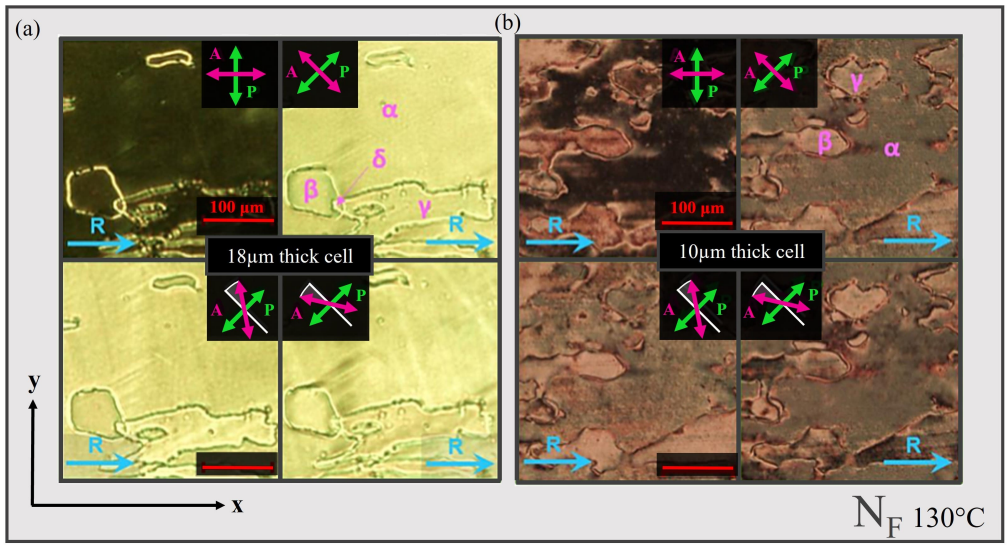

Figure 3.3: (a) $18\mu m$ and (b) $10\mu m$ thick silanized cells in N_F phase after ZFC from the N phase. The domains shown in (a) are of the same nature as those observed in (b) as described in the text. Regions α are uniformly aligned while β and γ are twisted with either right or left-handed rotation. The twisted polar domains exhibit the same brightness as the background in the thicker cell while they have a brighter appearance in the thinner one, which demonstrates the role of adiabatic rotation discussed in the text. Indeed, due to the lower thickness of the cell shown in (b), the twist is tighter and the adiabatic rotation in the domains is incomplete.

A clue for understanding this stability is the sudden disappearance of the twisted domains occurring when the electrodes are connected to ground (Fig 3.2e). Indeed, when the electrodes are in a floating configuration, a surface charge can accumulate at the RM734-electrodes interfaces, reducing, if not reversing, the tendency toward uniform ferroelectric alignment. Instead, when the electrodes are connected to ground this counter-field is removed trough the flow of free charges.

The existence of the polar coupling is clear once the response of ZFC N_F cells under in-plane electric fields is studied. As shown in Fig 3.2f, a small electric field $E = 1V/cm$ antiparallel to rubbing ($\mathbf{u}_E = -\mathbf{u}_R$) cancels the domains and stabilizes the alignment, while the same field in the parallel direction ($\mathbf{u}_E = \mathbf{u}_R$) is not enough to revert the polarity, producing instead a twisted state. Polarity reversal, which is completed when molecules detaches from the surfaces, and yielding a uniform alignment, can only be obtained with larger parallel fields, $E > 5V/cm$.

Upon field reversal, a pattern of defect line is created indicating that, in the presence of an opposing field, the N_F alignment breaks into stripe-shaped domains perpendicular to the field, in line with previous observations[5]. The time evolution of these domains leads to a complex system of topological lines moving without intersecting at different heights in the cell and giving rise to textures as in Fig. 3.2f, right-hand side panel. A careful description of the switching alongside the formed domains, their defect walls and their structures is presented in Fig 3.4, this study as been performed through a combination of topological observations and transmitted ligth intensity analysis, useful to distinguish differently twisted regions. The aim of the figure is to describe the variety of different domains (a-g) and topological defects (colored frames) found upon switching the field.

- Frame I shows A polar uniform planar alignment (a) that is achieved when **E** is opposite to **R**.

- In frame II, shortly after the field reversal, the bulk polarization becomes oriented along the field, while molecules in the proximity of the surfaces remain in their favorite -**R** direction; leading to rod-shaped domains where the polarization, moving from the top to the bottom surface of the cell, undergoes two opposite π rotations within each domain, which can be of opposite handedness (b-c), producing bright states. Since structures b and c cannot be easily distinguished, their assignment in frame II might be inverted. When domains with structure b and structure c come in contact, a thick domain wall is formed.

- Frame III shows that in time, one of the two handedness tends to prevail and most of the lines disappear.

- In frame IV becomes evident that the remaining domain walls start splitting into pairs of lines. The doubling of the blue lines in panel α can be represented as in the blue-framed c-b wall sketch in the bottom of the figure. The displacement of the lines reveals that they can cross, generating new domains having structures (d-e) described in the top panels and shown in frame IV. One of these (structure d), over time, appears to be the most energetically favorable and grows in volume. Again, structures d and e could not be distinguished so their assignment might be inverted. The displacement of the defect lines generates new domain walls (red and pink lines in panel β) whose structures are described in corresponding framed sketches. According to our description the two lines are located at different height inside the sample and thus they can cross without merging (see for example bottom right portion of frame IV).

- After a longer time, in Frame V, a new type of domain (f) is formed, which is interpreted as the inversion of the polarity of the molecules in contact with one of the two surfaces. This inversion eliminates part of the twist deformation, making the sample uniform in half of the height of the cell, leading to a darker texture.

The defect line in panel γ, marked in green, which separates this new state from a twisted state, is represented in green-framed panel.

- Upon reverting the field back to the original direction, in frame VI, the uniform planar alignment (a) is rapidly regained everywhere in the cell but where the domains (f) were observed. In these portions of the cell, where the surface anchoring was flipped, a new striped texture (g) is obtained, whose structure is analogous to (f), but inverted, showing another clean example of reversed surface polarity, supporting the notion of strong quadrupolar and weak polar anchoring. Different stripes are due to opposite handedness of the π twists. The defect line slightly changes (yellow line in panel δ) and the new one is sketched in the yellow-framed panel.

Cell textures observed upon *field cooling* are similar to those obtained by applying a field on ZFC N_F. In both ZFC and FC cells, the alignment induced by the electric field is not stable upon field removal as we observe the reappearance of polar domains as those in Fig. 2c.

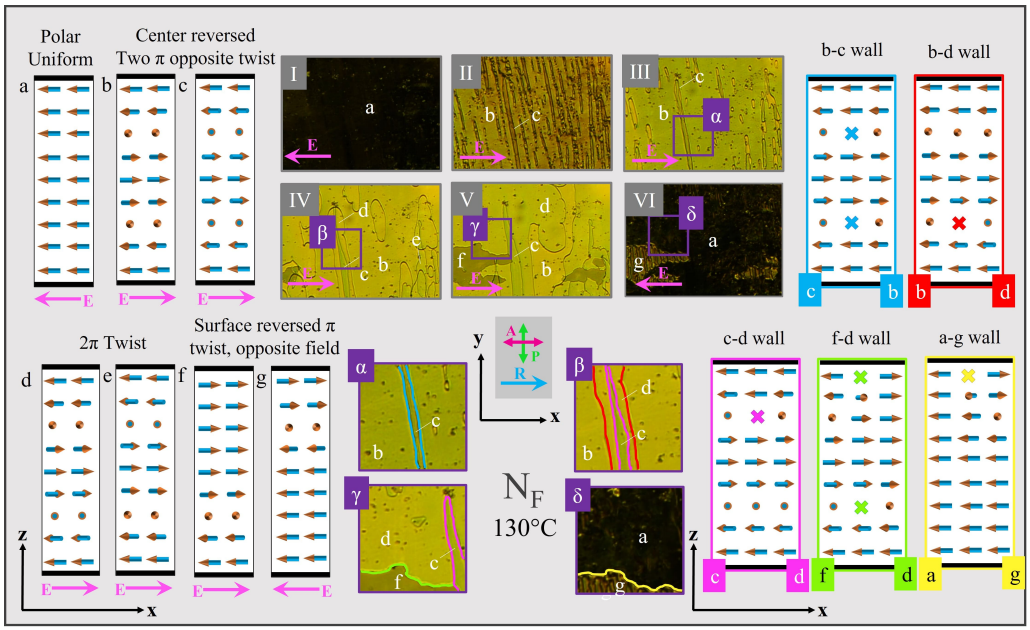

Figure 3.4: Sequence of frames of a switching event and magnification of their portions (α-δ) in which domains are labelled a-g and defect lines are marked with colored lines; their structure is described in the corresponding letter or color framed sketches, where it is represented as a coloured cross. The frames show the behavior of the N_F phase during a $\mathbf{E} = 1V/cm$ electric field reversal into an 18 µm rubbed silanized cell and the subsequent appearance of defect lines. Arrows: analyzer (**A**), polarizer (**P**), electric field (**E**), rubbing direction (**R**). The time interval between subsequent frames is about 2s. Pink arrow represents the electric field direction, blue arrow indicates the rubbing direction while dark pink and green arrows represent respectively the analyzer and the polarizer.

3.3.2 Rubbed Teflon cells

As already known in literature for other compounds[8,9] Teflon-rubbed surfaces induce planar alignment of RM734 molecules.

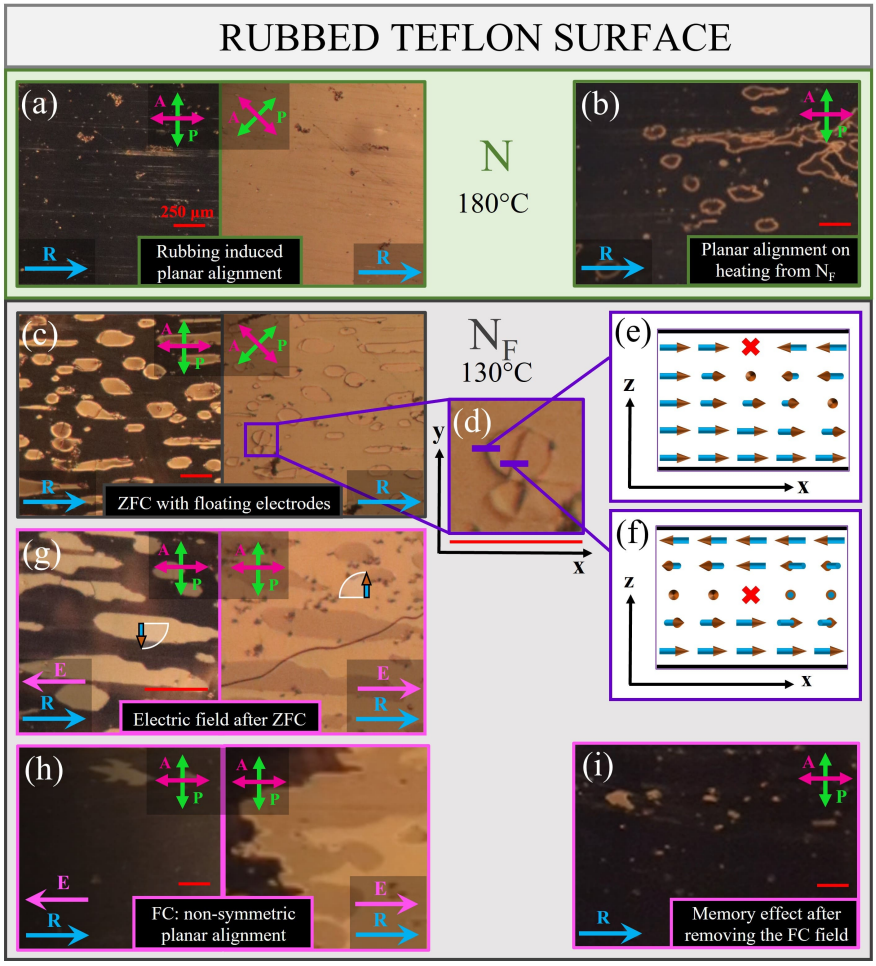

Figure 3.5: Polarized transmission optical microscopy images of 10 mm thick RM734-filled cells having rubbed Teflom surfaces. Arrows: rubbing direction (**R**), analyzer (**A**), polarizer (**P**), electric field (**E**). Shadings: nematic phase (green), ferroelectric nematic phase (grey). (a) Cells filled in N phase exhibit planar alignment. (b) Cell shows some remnant twist domain after heating from the N_F phase. (c) After ZFC most of the cell shows a dark homogeneous planar background with twisted domains with opposite boundary polarity (d) Magnification of a domain with an internal defect line. Its border is described in panel (e) while the internal defect is described in panel (f). Electric field effects on N_F phase (pink frames). (g) Strong polar anchoring is revealed applying a field $\mathbf{E} = 1V/cm$ against and along the rubbing direction, leading for ($\mathbf{u}_E = -\mathbf{u}_R$, left panel) to a darker stabilized background and an enhanced brightness of the twisted domains and for ($\mathbf{u}_E = \mathbf{u}_R$, right panel) to a twisted state in the previously uniform dark regions. (h) effects of the cooling with applied $\mathbf{E} = 1V/cm$: ($\mathbf{u}_E = -\mathbf{u}_R$, left panel) produces a homogeneous alignment, retained upon the removal of the field (i); ($\mathbf{u}_E = -\mathbf{u}_R$, left panel) produces three different luminous domains, described in Fig 3.6. The value of the scale bar is the same in every panel.

Although with some difference, this treatment exhibits, similarly to rubbed silane, a quadrupolar coupling in the N phase which combines with a polar coupling, antiparallel to rubbing ($\mathbf{u}_P = -\mathbf{u}_R$) upon entering the N_F phase. The homogeneous planar alignment of the N phase, in a $10\mu m$ cell, can be seen in Fig 3.5a; this alignment is independent on the loading direction. When this cell is ZFC into N_F phase, several twisted domains, connecting surfaces with inverted polarity, are generated (Fig 3.5c). Due to the low thickness of this cell, as already seen in Fig 3.3b, an imperfect adiabatic rotation is achieved resulting in domains with a different brightness respect of the background. These regions are delimited by thin bright lines that become dark upon $45°$ rotation of the polarizers (Fig. 3.5c and d). Indeed, the need of connecting a twisted domain with an uniform region results in twist-bend deformations which are sketched in Fig. 3.5e. Some domains, as the one magnified in Fig 3.5d, can also show an internal defect line, separating two regions of opposite twist and sketched in Fig. 3.5f. If T is raised and the system enters the N phase again, some domain remains pinned to the surface (Fig 3.5b), with an internal appearance equal to the homogeneous region around, probably due to the twist elimination for symmetry reasons.

Pink-framed images in Fig 3.5 represent the effect of the application of an in plane electric field. When a field $\mathbf{E} = 1V/cm$ is applied antiparallel to rubbing ($\mathbf{u}_E = -\mathbf{u}_R$), the uniform background is unaffected, while in the twist domains **n** undergoes partial in-plane reorientation that effectively reduce the twisted regions inside the cell. If the same field is applied in the opposite direction ($\mathbf{u}_E = \mathbf{u}_R$), the reorientation occurs mainly in the uniform region, which becomes twisted and bright; the magnitude of the field, however, is too low to produce a reversal of the polarity of the molecules onto the surfaces, which is indeed obtained for $\mathbf{E} \geq 10V/cm$. If the cell is cooled under a field $\mathbf{u}_E = -\mathbf{u}_R$ small domains are not present and an uniform ferroelectric phase, with a homogeneous orientation $\mathbf{u}_P = -\mathbf{u}_R$, is obtained (Fig 3.5h, left panel).

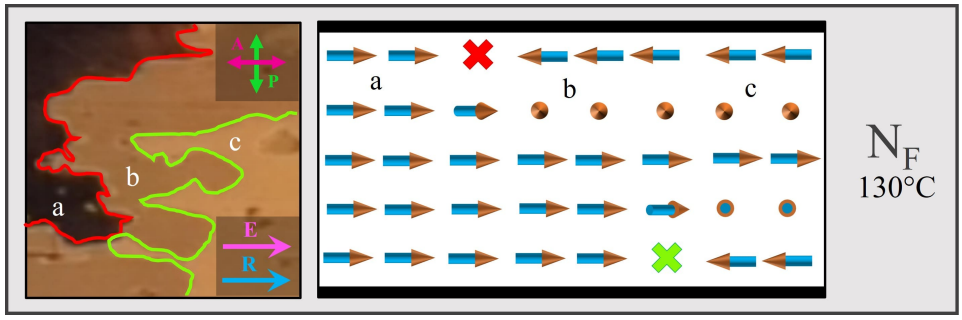

Figure 3.6: Analysis of the three zones (a-c) of the right panel of Fig 3.5h, obtained in a $10\mu m$ rubbed Teflon cell upon FC ($\mathbf{E} = 1V/cm$, $\mathbf{u}_P = \mathbf{u}_R$). The domain boundaries are highlighted with coloured lines and sketched in the right panel. Arrows: rubbing direction (**R**), analyzer (**A**), polarizer (**P**), electric field (**E**). The three domains can be represented as different combinations of boundary polarity: (a) both surfaces are equioriented in the same direction of the field, appearing as a dark, homogeneous phase; (b) the two surfaces are aligned in an antiparallel way, forming a π twisted domain compressed by **E** in half of the cell, appearing of medium brightness due to incomplete adiabatic rotation; (c) surfaces are parallel but in the opposite direction to the field, forming a 2π rotation along the height of the cell and appearing brighter because of an higher adiabatic rotation

A notable feature of FC cells is that this alignment is retained also after the field removal for both $d = 10\mu m$ and $d = 18\mu m$ samples (Fig 3.5i). This further confirm the presence of a stronger quadrupolar coupling along the whole sample and a weaker polar ordering which is dependent on the history of the sample.

When the cell is cooled under a field $\mathbf{u}_E = \mathbf{u}_R$ a more complex scenario, with three different brightness levels, is observed (Fig 3.5h, right panel and Fig 3.6): a dark, uniform, untwisted state, caused by the alignment of both the surface polarities along the field (Fig 3.6a); a domain with partial brightness, provoked by two opposite boundary polarities resulting in a twisted compressed structure near to the surface with the polarity opposite do the field which is too tight to produce a complete adiabatic rotation (Fig 3.6b); a region with higher brightness, where the molecules along both the surfaces are oriented against the applied field and producing two π twisted structures which are difficult to investigate but more deformed, and thus probably brighter, than the previous case (Fig 3.6c). All this observations suggest that Teflon cells contain a significant polar anchoring, with a favorite polarity $\mathbf{u}_P = -\mathbf{u}_R$, in a similar way of C16 silanized cells; however the coupling between RM734 and Teflon seems stronger than the one with aliphatic silanes since in this case the domains can survive the N_F-N transition and the asymmetric field response is much higher, requiring fields $\mathbf{u}_P = \mathbf{u}_R$ up to $\mathbf{E} = 10V/cm$ in order to revert the polarity at the surfaces.

3.3.3 Unrubbed Fluorolink MD700 cells

When RM734 is filled into unrubbed MD700 cells, it aligns planarly with a significantly weak anchoring strength; this means that the loading direction can influence the direction of the N ordering (Fig 3.7a).

If the temperature is cycled over $T_{I\text{-}N}$, this direction is forgotten leading to the formation of Schlieren textures (Fig. 3.7b) in which 1/2 and 1 defects are present, suggesting that the anchoring is strong enough to block their resolution escaping in the z-direction. The appearance of Schlieren textures further implies that the anchoring is weak degenerate. Being the alignment locally uniform, and any region extinguishable upon a proper rotation between cross polarizers, no twisted regions are present, indicating that the elastic forces arising from the distortion of the nematic director are able to overcome the anchoring forces, provoking sliding onto the surfaces.

When the cell is cooled, and the system enters the N_F phase, two different final configurations can be obtained, depending on the starting condition. If the sample is cooled from an homogeneous planar cell (as in Fig. 3.7a) the global alignment is preserved, while the system, free to rotate on the surface, rearrange into locally aligned planar regions surrounded by defect lines, roughly oriented as $\mathbf{n}$ (Fig. 3.7c). These defects have a structure composed by two dark lines (shown in Fig 3.7c-e and sketched in Fig3.7f-g), which slowly shrinks until an equilibrium is reached, probably stabilized by surface imperfections. Instead, when the Schlieren-textured system (Fig. 3.7b) is cooled, the molecules orients in a smooth way, showing a lesser number of similar "two-line" defects. These defects can be generated when domains with opposite polarity nucleate and try to merge through a combination of possible π or $-\pi$ onto the surfaces; when two opposite π and $-\pi$ rotations are present on the two surfaces (Fig3.7f, right panels) "trapped" splay-twist defect lines are generated, which tends to form couples in order to minimize the elastic energy, creating the structure sketched in Fig 3.7g.

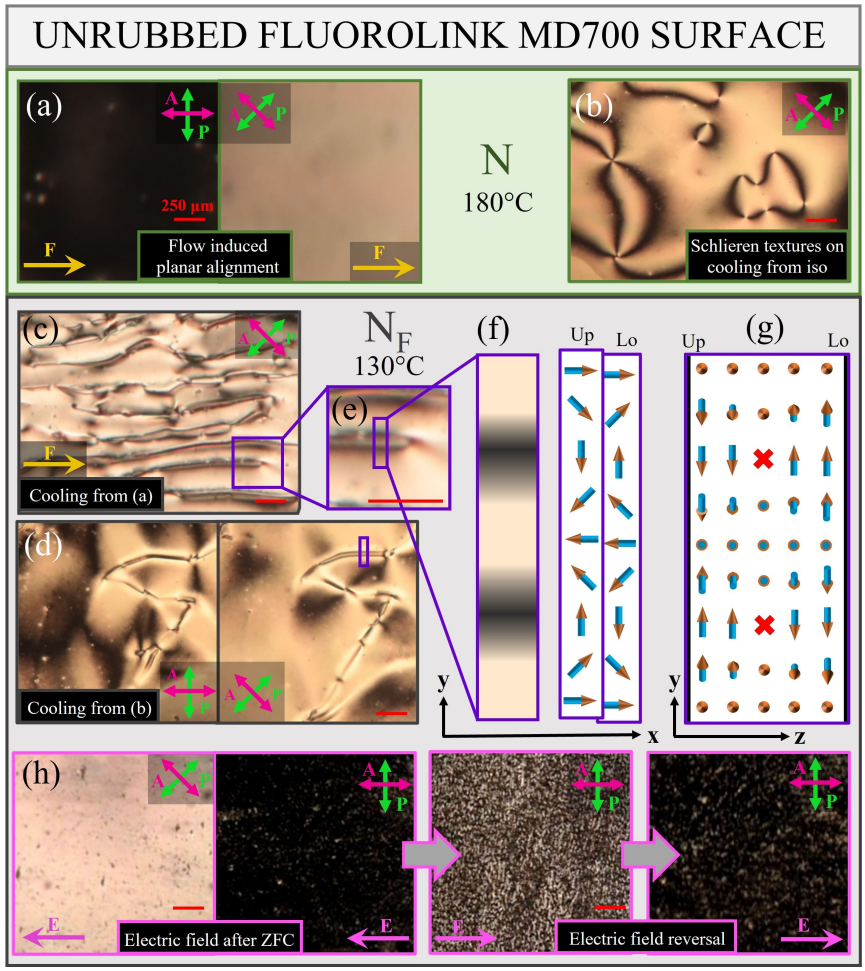

Figure 3.7: Polarized transmission optical microscopy images of 18 mm thick RM734-filled cells having Fluorolink MD700 coated surfaces. Arrows: rubbing direction (**R**), analyzer (**A**), polarizer (**P**), electric field (**E**). Shadings: nematic phase (green), ferroelectric nematic phase (grey). (a) Filling the cell in N phase, a planar alignment in the direction of the flow is achieved. (b) The same cell, once cooled from isotropic phase, shows Schlieren textures. (c) Defected structure cooling the cell to N_F starting from (a). (d) Defected structure cooling the cell to N_F starting from (b). (e) Enlargement of detail of a defect line, whose structural schemes are presented in (f) and (g). Electric field effects on N_F phase (pink frames). (h) When an electric field as low as $\mathbf{E} = 0.5V/cm$ is applied an homogeneous planar alignment is obtained for both **E** signs (h, second panel and fourth). In the third picture of (h) the disordered transient state, appearing upon **E** reversal, is shown, which evolves in about $1s$ into an homogeneous, but with a reversed polarity, planar state The value of the scale bar is indicated in the first panel.

Applying electric field as low as $\mathbf{E} = 0.5V/cm$ is possible to obtain a good alignment of **n** along **E** (Fig 3.7h), which is independent on the electrical and thermal history of the cell and preserved only if the electrodes are grounded after the field removal. This is analogous on what observed into C16 silanized cell, suggesting again that the presence of compensating charges onto the electrodes are decisive for the alignment of the ferroelectric nematic phase. Once the sign of **E** is reverted a sudden reorganization of

the molecules into the cell is obtained (Fig 3.7h, third panel), demonstrating the polar coupling between **E** and **P**. The degenerate planar anchoring is further hinted by the absence of difference between FC and ZFC.

3.3.4 Unrubbed hydroxylated glass cells

The cells realized with hydroxylated glass, when filled with RM734, show a different behavior with respect of the previous ones. In this type of cells, in N phase, molecules are aligned perpendicular to the surfaces in the so-called homeotropic ordering (Fig 3.8a), while turning in a disordered planar alignment once cooled into N_F phase (Fig 3.8b). The homeotropic alignment is stable only upon cooling from isotropic phase into the nematic phase or heating from the ferroelectric nematic, indeed, as soon as the cells are loaded in N phase at $180°C$, a random planar texture, analog to the one in Fig. 3.8b, is obtained.

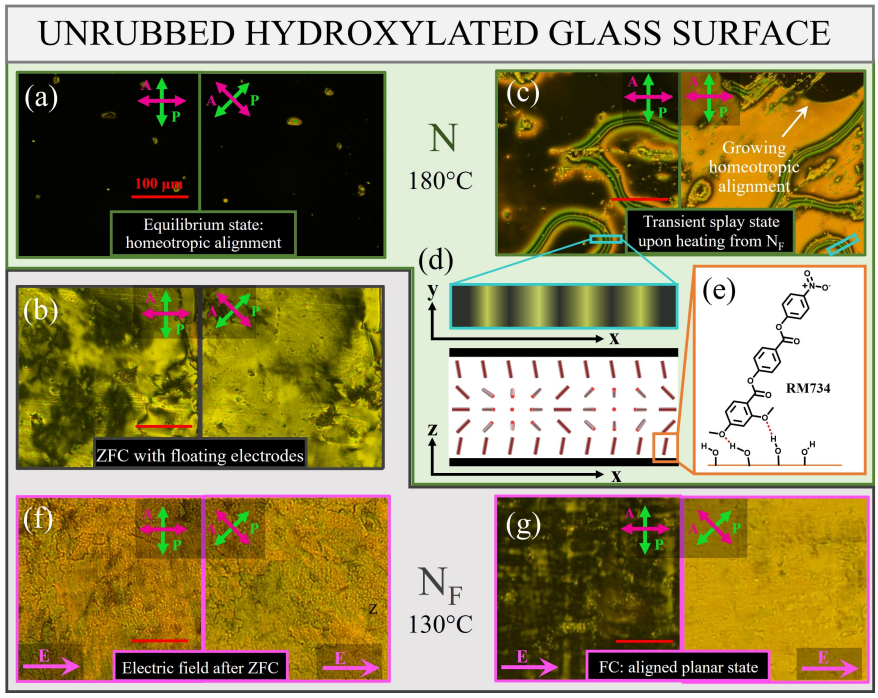

Figure 3.8: Polarized transmission optical microscopy images of 18 mm thick RM734-filled cells having hydroxylated glass surfaces. Arrows: rubbing direction (**R**), analyzer (**A**), polarizer (**P**), electric field (**E**). Shadings: nematic phase (green), ferroelectric nematic phase (grey). (a) Homeotropic alignment obtained upon cooling from isotropic phase. (b) Random planar alignment obtained upon cooling to the N_F phase. (c) Transient pseudo-planar alignment obtained upon fast heating from N_F phase, whose structure is sketched in panel (d). This order is substituted by homeotropic ordering in a few seconds. (e) Sketch of the proposed H-bond-based anchoring. Electric field effects on N_F phase (pink frames). (f) When an electric field up to $\mathbf{E} = \pm 20 V/cm$ is applied to (b) an inhomogeneous twisted structure is obtained. (g) Planar aligned state obtained upon FC with a field $\mathbf{E} = \pm 7.5 V/cm$. The value of the scale bar is indicated in the first panel.

This type of alignment is uncommon on uncoated glass, however has been recently observed that cyano liquid crystals can give transient homeotropic alignment near to $T_{I\text{-}N}$ when confined in plasma-cleaned glass, explained as a result of dipolar interactions

with the surfaces[10]. The alignment of RM734 can be induced by a combination of dipole interactions and H-bonding with the hydroxyls introduced by the treatment with piraña solution, as represented in Fig 3.8e.

Once the system gets to $T_{N\text{-}N_F}$ the homeotropic order suddenly starts changing, transforming into an inhomogeneous planar texture, with several zones inextinguishable upon rotations between crossed polarizers (Fig 3.8b), indicating twisted domains and the formation of interactions with the surfaces strong enough to overcome the elastic and electric torques deriving from clashing surface orientations. The change in orientation during the N-N_F transition is probably due to the arise of spontaneous polarization, which would produce strong repulsions due to surface charge accumulation; furthermore, the H-bonded-mediated anchoring has a polar nature, being pointed towards the glass, thus being incompatible with an equioriented ferroelectric nematic phase.

If the N_F phase is slowly heated back to the N phase is recovered, while for fast heating rates a transient pseudo-planar state is observed (Fig 3.8c) for few seconds prior to converting to the homeotropic alignment. In this state molecules are roughly aligned with the filling direction and the planar layer is thin, since it the appearance of colours is a sign of reduced thickness. This splayed molecular configuration is sketched in Fig 3.8d and its preferential alignment along the filling direction may indicate a stable tilt of the RM734 molecules on the surface, possibly indicating a sort of common H-bond anchoring direction.

The random planar N_F ordering obtained in hydroxylated glass cells, compared with the previous surfaces, is much less sensitive towards in-plane electric fields which generates a highly inhomogeneous and inextinguishable texture, sign of a twisted structure. This structure survives up to $\mathbf{E} = \pm 20 V/cm$, when the interaction with the surfaces are overcome and a roughly homogeneous texture is obtained (Fig 3.8f). If the N-N_F transition occurs with a field of at least $\mathbf{E} = \pm 7.5 V/cm$ a well aligned planar state is obtained; when the field is removed the alignment is lost and the random planar texture of Fig 3.8b is reobtained.

3.4 Discussion

Looking at the variety of different behaviours of RM734 confined into different cells it's evident that the type and the strength of the surface coupling vastly influences the textures, the defects and the field response of the N_F phase, as summarized in Table 3.1.

Fluorolink MD700 cells showed the planar alignment with the smallest surface interactions, with an homogeneous orientation in the same direction of the loading flow, in N phase, turning in a particular texture, with typical defect lines and a remarkably high sensitivity towards external electric fields once entered in the ferroelectric phase.

Rubbed Teflon cells, while still being planar in both N and N_F phases, show a high polar coupling with the surfaces, in the direction of rubbing. This coupling produces homogeneous textures asymmetrically responding to oppositely directed external fields and is strong enough to maintain the alignment once $\mathbf{E}$ is removed.

C16 silanized cells are characterized by an intermediate behaviour between these two: the alignment is again planar in both N and N_F phases, but the polar contributions are lower, resulting in a smaller asymmetric response towards in-plane electric fields and in the impossibility of alignment retention.

A markedly different behaviour is shown by cells realized using hydroxylated glass slides; in this samples, an anchoring transition is present, with the alignment passing from homeotropic in N phase to random planar in N_F phase. This random planar align-

ment has the strongest LC-surface interactions in locally random directions, which can be overcome only by relatively high fields and promptly reformed once **E** is removed.

This wide set of behaviours indicates that the polar nature of the ferroelectric phase has a role in interacting with different surfaces and that the bulk structure assumed by RM734 to account for the peculiar elastic and electric constraints of the N_F phase vastly relies on the specificities of the confining materials. For example two parallel rubbed surfaces, with strong polar coupling, can induce a vectorially unidirectional orientation of the polarization that can be exploited to switch between uniform and twisted structures, respectively producing dark and bright states. Using two weakly interacting surfaces, instead, is possible, using extremely low in-plane fields, to induce, for both the bulk and the surfaces, a complete π rotation of the polarization, obtaining a device switchable with two opposite **E** directions.

3.5 Conclusion

In this chapter the alignment of the N_F of RM734 confined in cell with different rubbed and unrubbed surfaces has been presented. According to the different natures of the four tested substrates, several different effects, arising from the polar symmetry breaking of the N_F phase, has been observed. RM734 molecules possess different degrees of coupling with different materials, affecting their collective behaviour, forming different textures and showing different responses toward external electric fields for every different tested substrate. The alignment type obtained in N phase and upon cooling in N_F phase, for both FC and ZFC, has been studied and treated in detail in the previous sections and summarized in Table 3.1. According to the results presented so far in this chapter, the interactions of the N_F of RM734 with the confining surfaces is greatly affected by its polar ordering; the understanding of the interplay between a material and different bounding surfaces is indeed one central aspect of liquid crystal science and technology.

These results further demonstrate that the control of the polarity of the 2D confining surfaces can be a practical method to impose a structured vectorial orientation distribution of a 3D volume of polar molecules.

Confining surface	N phase (180°)	N_F phase (130°)	E-field response after ZFC	E-field response after FC	Alignment stability after $\mathbf{E}$ removal
Rubbed C16 silanized glass	Rubbing-induced planar alignment	Rubbing-induced strong quadrupolar alignment coupled with polar alignment	Asymmetric response uniform with: $\mathbf{E} \leq -1V/cm \cup \mathbf{E} \geq 5V/cm$	Analogous to ZFC	Unstable
Rubbed Teflon	Rubbing-induced planar alignment	Rubbing-induced strong quadrupolar alignment coupled with strong polar alignment	Asymmetric response uniform with: $\mathbf{E} \leq -1V/cm \cup \mathbf{E} \geq 10V/cm$	Analogous to ZFC	Stable
Unrubbed Fluorolink MD700	Free to slide degenerate planar alignment	Degenerate planar	Symmetric response. Uniform with: $\mathbf{E} \leq -0.5V/cm \cup \mathbf{E} \geq 0.5V/cm$	Analogous to ZFC	Stable with grounded electrodes
Unrubbed hydroxy-lated glass	Homeotropic alignment	Strong local random polar anchoring	Weak symmetric response. Uniform with: $\mathbf{E} \leq -20V/cm \cup \mathbf{E} \geq 20V/cm$	Symmetric response uniform if FC with: $\mathbf{E} = \pm 7.5V/cm$	Unstable

Table 3.1: Summary of the behaviour of RM734 in the four considered treated cells: alignment type in N and N_F phases, response to external in-plane electric fields $\mathbf{E}$ and alignment stability after $\mathbf{E}$ removal.

Bibliography

[1] R. J. Mandle, S. J. Cowling, and J. W. Goodby. A nematic to nematic transformation exhibited by a rod-like liquid crystal. *Physical Chemistry Chemical Physics*, 19:11429–11435, 2017.

[2] A. Mertelj, L. Cmok, N. Sebastián, R. J. Mandle, R. R. Parker, A. C. Whitwood, J. W. Goodby, and M. Čopič. Splay nematic phase. *Physical Review X*, 8, 11 2018.

[3] N. Sebastián, L. Cmok, R. J. Mandle, M. R. D. L. Fuente, I. D. Olenik, M. Čopič, and A. Mertelj. Ferroelectric-ferroelastic phase transition in a nematic liquid crystal. *Physical Review Letters*, 124, 1 2020.

[4] H. Nishikawa, K. Shiroshita, H. Higuchi, Y. Okumura, Y. Haseba, S. I. Yamamoto, K. Sago, and H. Kikuchi. A fluid liquid-crystal material with highly polar order. *Advanced Materials*, 29, 11 2017.

[5] X. Chen, E. Korblova, D. Dong, X. Wei, R. Shao, L. Radzihovsky, M. A. Glaser, J. E. Maclennan, D. Bedrov, D. M. Walba, and N. A. Clark. First-principles experimental demonstration of ferroelectricity in a thermotropic nematic liquid crystal: Polar domains and striking electro-optics. *Proceedings of the National Academy of Sciences*, 117:14021–14031, 2020.

[6] X. Chen, E. Korblova, M. A. Glaser, J. E. Maclennan, D. M. Walba, and N. A. Clark. Polar in-plane surface orientation of a ferroelectric nematic liquid crystal: Polar monodomains and twisted state electro-optics. *Proceedings of the National Academy of Sciences*, 118, 2021.

[7] J. Cognard. *Alignment of Nematic Liquid Crystals and Their Mixtures*. Gordon and Breach Science Publishers,, 1982.

[8] J. C. Wittmann and P. Smith. Highly oriented thin films of poly(tetrafluoroethylene) as a substrate for oriented growth of materials. *Nature*, 352:414–417, 1991.

[9] P. Hubert, H. Dreyfus, D. Guillon, and Y. Galerne. Anchoring orientation of nematic and smectic a liquid crystals on ptfe treated plates. *Liquid Crystals*, 45:757–764, 2018.

[10] Y. Kim, M. Lee, H. S. Wang, and K. Song. The effect of surface polarity of glass on liquid crystal alignment. *Journal de Physique II*, pages 1371–1383, 1995.

Part III

Sessile droplets of RM734 on Lithium Niobate crystals

CHAPTER 4

Electrostatic instability of RM734 sessile droplets deposited on ferroelectric crystals

4.1 Introduction

In this chapter the behaviour of sessile droplets of the ferroelectric nematic material RM734[1,2], once deposited on a ferroelectric crystal of lithium niobate ($LiNbO_3$, LN), is investigated[3]. The fluidity of the N_F phase, coupled with its huge polarization density, increases the responsivity of this new material towards electric fields while qualitatively modifying it respect of the one of both conventional dielectric liquids and ferroelectric solids; these two characteristics, as noticed in the previous chapter, lead to the accumulation of a surface charge $\sigma = \mathbf{P} \cdot u$ every time $\mathbf{P}$ isn't parallel to a confining surface, being u a unit vector representing the perpendicular direction to it. This observation motivated the need for an investigation of the interactions between the ferroelectric nematic solid and a ferroelectric crystal, studying the coupling between the polarizations of the two ferroelectric materials and seeing the differences in wettability and contact angle between N and N_F phases of RM734.

To probe these properties small droplets of RM734 are deposited upon an untreated lithium niobate crystal and their contact angles are recorded while cooling from isotropic to ferroelectric nematic phases. The contact angle is maximum – and thus the wettability is minimum– in the I phase, slightly and continuously decreasing together with T and across the I-N transition and showing an abrupt discontinuity at $T_{N\text{-}N_F}$. If T is further decreased, a shape-instability point is reached, and the droplet explodes ejecting jets of material, branching into secondary streams and breaking into new smaller droplets, which can explode as well once the temperature is low enough.

This electrostatic instability can be seen as an analog of the so-called Rayleigh instability[4], in which charged conductive liquid droplets disintegrate once a critical charge-to-volume ratio is exceeded. This explosion occurs when the electrostatic repulsions overcome the surface tension of the liquid, reducing the droplet electric charge upon the formation of jets which take the charges apart. Rayleigh instability has been deeply investigated[5–10] and exploited in various biomedical[11–13] and technological applications, such as electrospray ionization mass spectroscopy[14], inkjet printing[15] and 3-D printing[16], however, due to its fast kinetics, the exact fission mechanism, involving the formations ad retractions of fluid jets, has not been reported yet. Even though some theoretical investigation has been done on infinitely long LC jets[17,18], Rayleigh instability in liquid crystalline materials has never been experimentally observed.

The instability described in this chapter shares features from both the Rayleigh instability, (like the formation of jets and secondary droplets) and the polar properties of the N_F phase (like the molecular order into the jets and the dependence of the instability threshold on T, reflecting the N_F's $\mathbf{P}$ dependence of on T). Furthermore the viscosity

of RM734 in ferroelectric nematic phase varies between 0.05 and $3Pa \cdot s$ depending on T[19], being higher than the one of the materials usually used in Rayleigh instability works[6,7,14], slowing the process down and allowing kinetical studies.

4.2 Materials and methods

4.2.1 Materials

$LiNbO_3$ crystals

RM734 has been used as ferroelectric fluid while as ferroelectric solid substrates z-cut slices of lithium niobate crystals with a thickness of $900\mu m$ has been used, whose structure is represented in Fig. 4.1a. Three different types of crystals have been used for the experiments: undoped crystals, bulk iron-doped crystals, containing $0.1\%mol$ of iron and diffused iron-doped crystals[20,21], in which $0.3\%mol$ of iron atoms are confined in the first, $30\mu m$-thick, superficial layer of the substrate. The bulk spontaneous polarization $\mathbf{P}_{LiNbO_3}$ of a lithium niobate crystal along the [0001]z axis arises from the displacement of the lithium and niobium atoms across the same axis producing an asymmetric unit cell possessing ferroelectric properties (Fig 4.1b). Its magnitude is very high, reaching a huge value of about $60\mu C/cm^2$ at room temperature, which is over ten times higher than the one of RM734, and decreases as a function of T until the Curie temperature T_C ($\sim 1413K$) is reached (Fig. 4.1c) and the cation displacement abruptly goes to 0 (Fig 4.1d). However, due to the presence of a compensation mechanism due to the migration of free charges on the z-cut surfaces, the surface charge density of a thermalized $LiNbO_3$ crystal is not equal to the bulk polarization as one could expected in an idealized crystal, but it is reduced to only $10^{-2}\mu C/cm^2$ [22].

If a rapid variation of T occurs, a transient pyroelectric field is obtained as a result of the combination of the fast displacement of the cations in the bulk and the slow motion of the free charges at the surfaces: when the temperature is modified, the bulk polarization of the crystal promptly respond to this change while the free charges at the surface are still in their previous position, producing the pyroelectric effect[23–25]. Its strength can be extimated using the pyroelectric coefficient of $LiNbO_3$ crystals, which is almost constant in the temperature range used during the experiment and assumes, according to the literature for both doped[26] and undoped materials[27,28], values in the range of $10^{-5} - 10^{-4}C/m^2K$. This parameter can be obtained as the slope of the polarization graph fig. 4.1c finding a value of about . Considering a temperature decrease of $\sim 30K$, a variation in $\mathbf{P}_{LiNbO_3}$ in the order of $\sim 1\mu C/cm^2$ is found and thus a similar induced surface charge density can be expected because of the slow redistribution of charges.

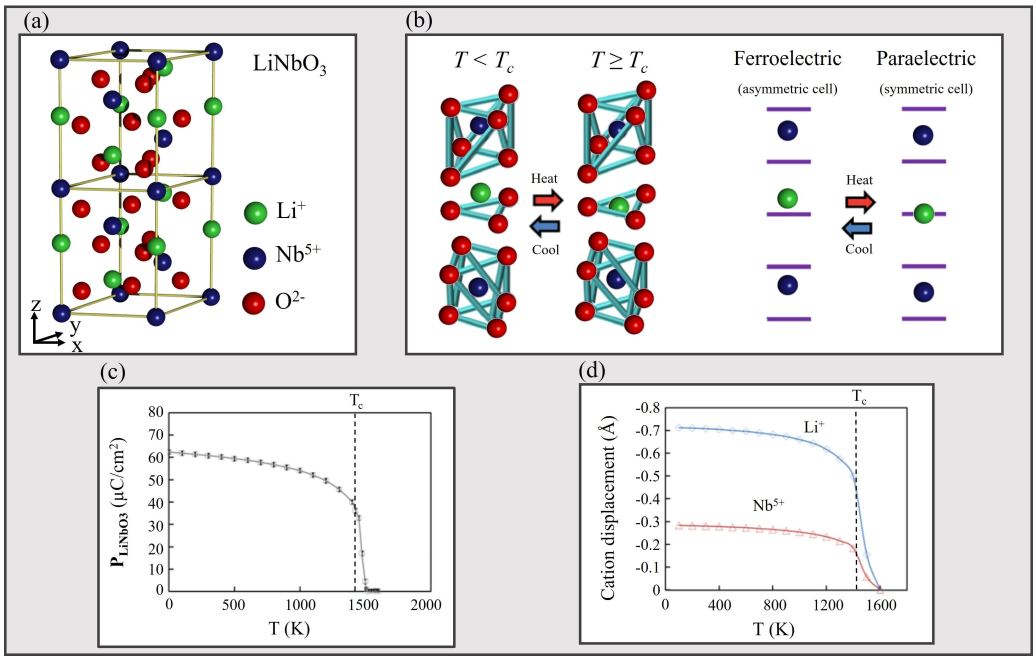

Figure 4.1: (a) $LiNbO_3$ crystal structure. (c) Simulated polarization density for a $LiNbO_3$ crystal. The vertical dashed line marks the Curie temperature. (d) Mean cation displacement as a function of T in a $LiNbO_3$ crystal. The red curve represent niobium ions while the blue curve represents lithium ions. The vertical dashed line marks the Curie temperature.

RM734 droplets

Round droplets of RM734 are created using a four-step process:

1. A small quantity of RM734 powder is heated on a clean glass slide until the melting point is reached.
2. A clean, cold, stainless steel needle is dipped into the liquid and raised, obtaining a small solidified droplet on the tip; the obtained RM734 sphere can be enlarged performing successive and rapid dips.
3. The obtained spheres are then remolten on the glass substrate and cooled to RT.
4. Solid droplets are then collected and placed onto the proper substrate, slowly pre-heated to $200°C$, a temperature higher than $T_{I\text{-}N}$.

A calibration slide has been used to measure the diameter d of the droplets, finding values in the range $250\mu m < d < 1250\mu m$.

4.2.2 Polarized transmission optical microscopy observations

Images of the droplets are collected both in bright field and between crossed-polarizers while movies are recorded with a rate of $25FPS$. Thermal control is achieved using a microscope oven and the temperatures were lowered form $200°C$ to $80°C$, cooling the sample from below. The cooling rate used was $0.1°C/s$, unless differently stated.

4.2.3 Contact angle measurements

The contact angle θ is measured, as a function of T, using the setup sketched in Fig. 4.2 which can be summed up as the combination of a collimated light source, an imaging system and an hot stage. The light source is composed by a white LED, producing the light, coupled with an iris and a collimating lens to obtain a collimated beam while the imaging system is made up with an imaging lens, an iris (working as an aperture stop), a collecting lens and a CMOS-camera; the lenses are placed so to have their focus into the aperture of the iris. The thermal control is achieved using an aluminum block surrounding four resistive heater cartridges, which are powered by a programmable power supply and driven by a Labview PID, receiving temperatures from a thermocouple connected to a DAQ. In these experiments the temperature of the material was lowered form $200°C$ to $90°C$, cooling the crystal from below. The cooling rate used was $0.1°C/s$, unless differently stated.

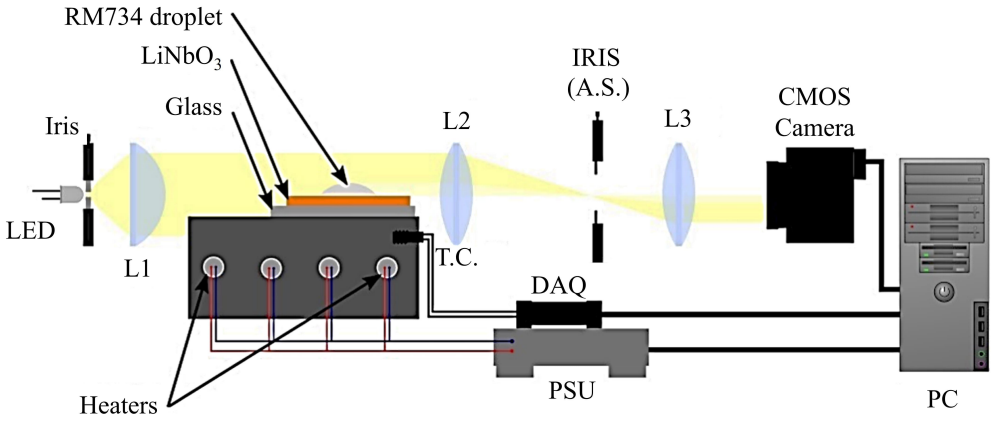

Figure 4.2: Setup for measuring RM734 droplets contact angle on $LiNbO_3$. L1, L2 and L3 represent respectively collimating, imaging and collecting lenses. Two iris are present, the first one is coupled with a LED light source to reduce its width while the second one is placed between L2 and L3 and works as an aperture stop (A.S.). A CMOS camera is positioned in the focal plane of L3. The temperature control of the sample is operated by an hot stage made of an aluminum block with four resistive heater cartridges inserted. A termocouple (T.C.) records the temperature and, together with a DAQ, feeds a PID controller that drives a programmable power supply unit (PSU) connected to the heating cartridges.

4.3 Experimental results

4.3.1 Contact angle

The measured contact angles θ, obtained for sessile droplets of RM734 laying on a $LiNbO_3$ surface, and varying as a function of T, are shown in Fig. 4.3a. A continuous increase of the wettability is visible when cooling from I to N phase and across $T_{I\text{-}N}$, probably caused by a decrease of the surface tension γ – a behaviour commonly observed in conventional thermotropic nematic mesogens[29] – and an increase of the interactions with the charged ferroelectric surface, further reducing γ and consequently, according to the Lipmann realtion[30], the contact angle θ. Once $T_{N\text{-}N_F}$ is reached a sudden jump in θ,

evident even by a visual comparison of the pictures in Fig4.3c, is recorded, with a new value in N_F phase being roughly an half of the one in N phase.

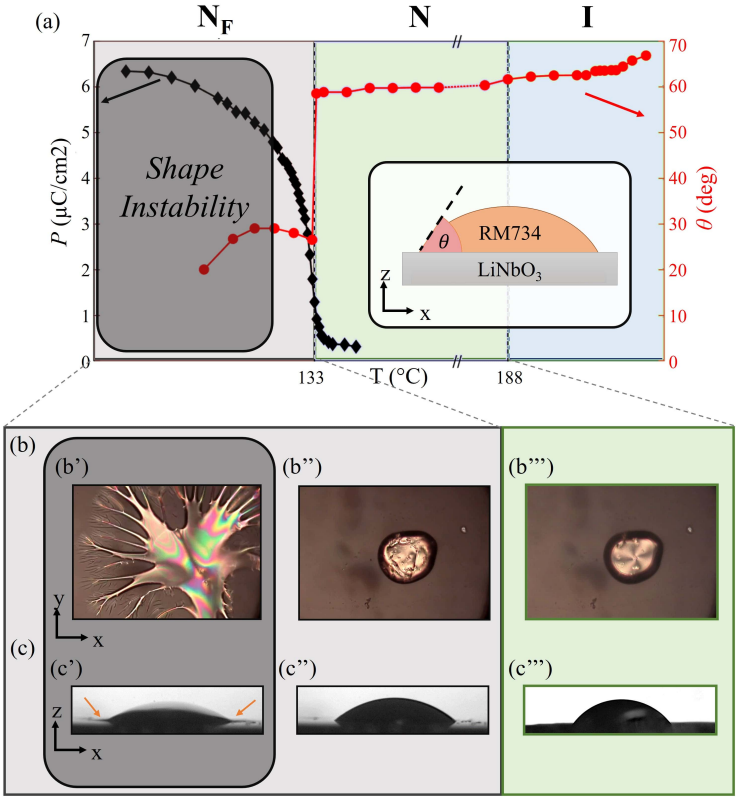

Figure 4.3: (a) Spontaneous polarization P (black diamonds) ad contact angle θ (red dots) of a RM734 sessile droplet on a $LiNbO_3$ crystal as a function of temperature. Different shadings indicate different LC mesophases and the instability region within the N_F phase. The inset shows the schematics of the analyzed system, representing the LC material, the ferroelectric crystal and the contact angle θ (b) PTOM images of the same droplet at three different temperatures, $160°C$ (b'''), $130°C$ (b'') and $109°C$ (b'), showing the different textures in N and N_F phases and the result of the explosive instability. Droplet diameter $\sim 300\mu m$. (c) Side view of the same droplet at the same three temperatures, comparing (c''') and (c'') is it possible to see the decrease of contact angle related to the N-N_F transition. Orange arrows in (c') indicate two different jets expelled on the surface.

This change in wettability is associated to a change in the textures when imaged between crossed polarizers: indeed, in N phase molecules possess a well-defined orientation, with **n** homeotropically aligned respect of the lithium niobate surface and parallel to the air surface, forming a defect on the top (Fig. 4.3b'''), in complete agreement with previous observation on sessile RM734 droplets [31]. The homeotropic alignment of the N phase of RM734 induced by $LiNbO_3$ surfaces has been verified constructing a $6\mu m$-thick flat cell using lithium niobate crystals slides as confining substrates. At temperatures lower than $T_{N\text{-}N_F}$, the polar order starts emerging leading to the formation of a brighter and more complex texture characterized by the presence of several topological defect

lines (Fig 4.3b") together with a change of the surface orientation of the molecules, passing from homeotropic to planar, in an alagous way of the hydroxylated glass cells treated in the previous chapter[32].

4.3.2 Shape instability

When the temperature is further decreased, an explosive shape instability occurs, modifying the droplet shape an making it spread on the surface. This sudden reaction is provoked by the interaction between the polarizations of the ferroelectric nematic and the ferroelectric crystalline material and it occurs, once fixed the cooling rate, at a temperature which depends for the largest part on the droplet's diameter and for a minor part on the specific lithium niobate sample. This event is imaged in Fig 4.3b' and c' where a further flattening of the droplet is accompanied wit the emission of liquid jets (pointed by orange arrows), while no visible texture changes are present right before the explosion. Even though droplet instabilities occur every time the temperature is decreased, the explosion may occur with different morphologies, as can be noticed in Fig 4.3b' and in Fig. 4.4a-d, showing the first video frame collected after the instability event ($40ms$) in various different droplets.

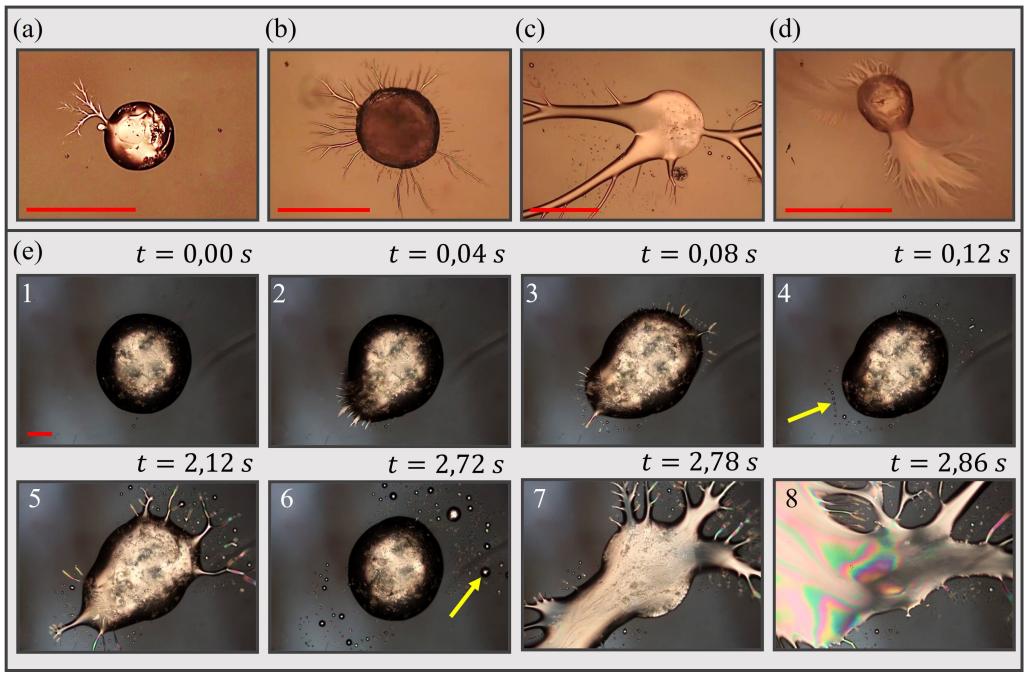

Figure 4.4: (a-d) Galley of different RM734 droplets explosions on iron-doped $LiNbO_3$ crystals, imaged as the first frame ($40ms$) after the instability event . Droplet diameter, explosion temperature and cooling rates: (a) $300\mu m$, $128^\circ C$, $0.3^\circ C/s$; (b) $480\mu m$, $104^\circ C$, $0.1^\circ C/s$, (c) $500\mu m$, $131^\circ C$, $0.2^\circ C/s$, (d) $250\mu m$, $125^\circ C$, $0.07^\circ C/s$. (e) Consecutive frames of the cooling, from $133^\circ C$ to $123^\circ C$, of a $1100\mu m$ RM734 droplet on an undoped lithium niobate crystal. Several characteristics of the instability and be observed: jet ejection and branching (panel e, frames 2 and 3), formation of secondary droplets (panel e, frames 3 and 4), reformation of the original droplet (panel e, frame 6), further instabilities (panel e, frames 5, 7 and 8)

The five principal possible behaviours observed are: (I) violent explosion (Fig. 4.3b'); (II) slower expulsion of a single jet (Fig. 4.4a); (III) ejection of several thin jets (Fig 4.4b); (IV) expulsion of large jets (Fig. 4.4c); (V) protrusion of large areas combined with emission of jets (Fig. 4.4d).

This variety may result from several factors like differences in droplet size, cooling rates, $LiNbO_3$ substrates and instability temperature, however, a clear interconnection between the observed behaviour and these parameter hasn't been detected. After this first stage, the instability proceeds in a similar way in all the observations, with an example in Fig. 4.4e, representing a $1100\mu m$-sized RM734 droplet exploding (starting at $T = 131°C$) on an undoped $LiNbO_3$ crystal when cooled from $133°C$ to $123°C$. The instability event begins with the expulsion of jets accompanied with a droplet shape deformation (Fig. 4.4e frame 1), the ejected jets tips show a tendency to bifurcate, probably caused by an instability of the jets themselves (Fig. 4.4e frames 3, 5 and 7). This bifurcations create a multi-level ramified structure in which the typical angle between arms is $\sim 45°$ (further examples are present in Fig 4.7). After the first expulsion event, the system seems to lose its propulsion and the jets start to break up in two parts, one being retracted back to the original droplet (Fig 4.5) and one splitting into new smaller droplets (marked with yellow arrows in Fig 4.4e panels 4 and 6).

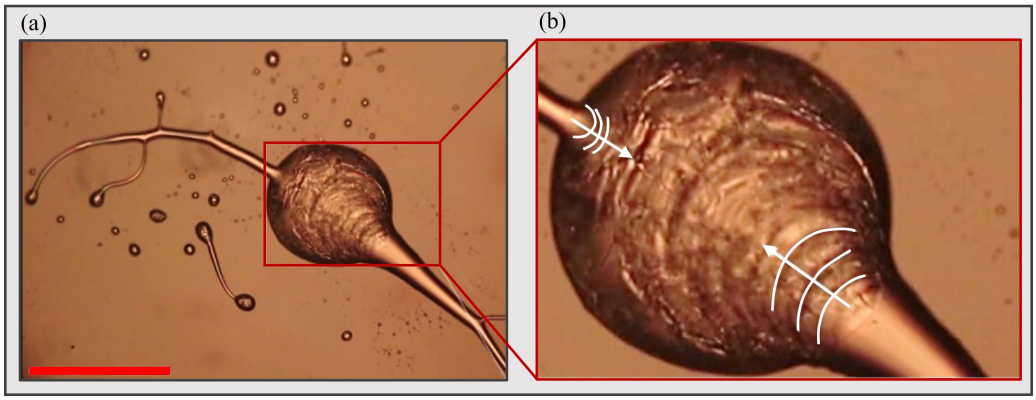

Figure 4.5: (a) Retraction of jets in a RM734 droplet on a doped $NbLiO_3$. Droplet diameter $450\mu m$, scale bar $500\mu m$. (b) Enlargement of (a) showing the mechanical waves (highlighted in white), moving in the verse of the white arrow, provoked by the retraction of the liquid crystalline material

This loss of material, reducing its size, temporally stabilizes the original droplet which can undergo new instabilities as T is further reduced. The correlation between the droplet size and the shape instability temperature T_{si} has been measured studying consecutive explosion of both the mother droplet (which can be up to seven for a single experiment) and the largest among the secondary droplets (similarly exploding once a low enough T is reached); the results are represented in Fig 4.6 which also shows the polarization on RM734 droplets as a function of their size.

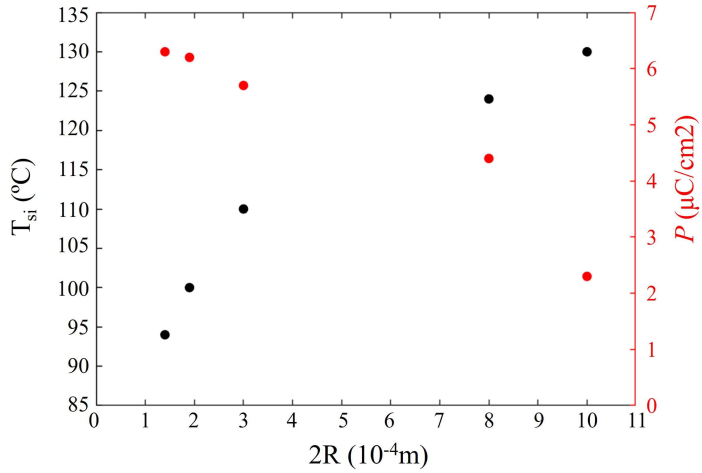

Figure 4.6: Dependence of shape instability temperature T_{si} and polarization **P** on droplet diameter 2R.

This plot evinces that smaller droplets require higher value of **P**, and hence lower temperatures, to eject jets of materials, suggesting that the stability of the droplets increases lowering the diameter. When the jets are imaged through crossed polarizers it is clear that the director **n** is oriented along their main axis, since the jets parallel to either the polarizer or the analyzer appear dark (Fig. 4.7). This observation implies that, being **P** parallel to **n** in N_F phase, the jet tips possess an electrical charge, suggesting that their repulsion and tendency to bifurcate is caused by electrostatic interactions.

Other observations suggest the predominant role of electrostatics are: the path followed by LC streams; the repulsion between the jets, which spaces them and prevents their merging (Fig. 4.7a); the interaction of jets with other droplets which can be repulsive (Fig 4.7d), making the stream avoid the droplet, or attractive, provoking the collision of the jet and the droplet. The importance of electrostatics is further highlighted by the need of the ferroelectric lithium niobate crystal as a solid surface, indeed, using other surfaces (such as glass, Teflon and polymer-coated glass) no traces of instability can be detected in sessile RM734 droplets. Flipping the $LiNbO_3$ slide makes no difference on the RM734 instability, showing that the sign of the pyroelectric field generated by the lithium niobate is irrelevant, thus excluding a possible role of solubilized ions and confirming that the instability arises solely from the polarization of the N_F phase. Using the aforementioned conditions jets are uniquely emitted in contact with the ferroelectric surface (as shown in Fig. 4.3c'); however, if the grounded metal lid of the microscope oven is kept close to the sample, tree-like jets are formed, vertically connecting the droplet and the lid (Fig. 4.8).

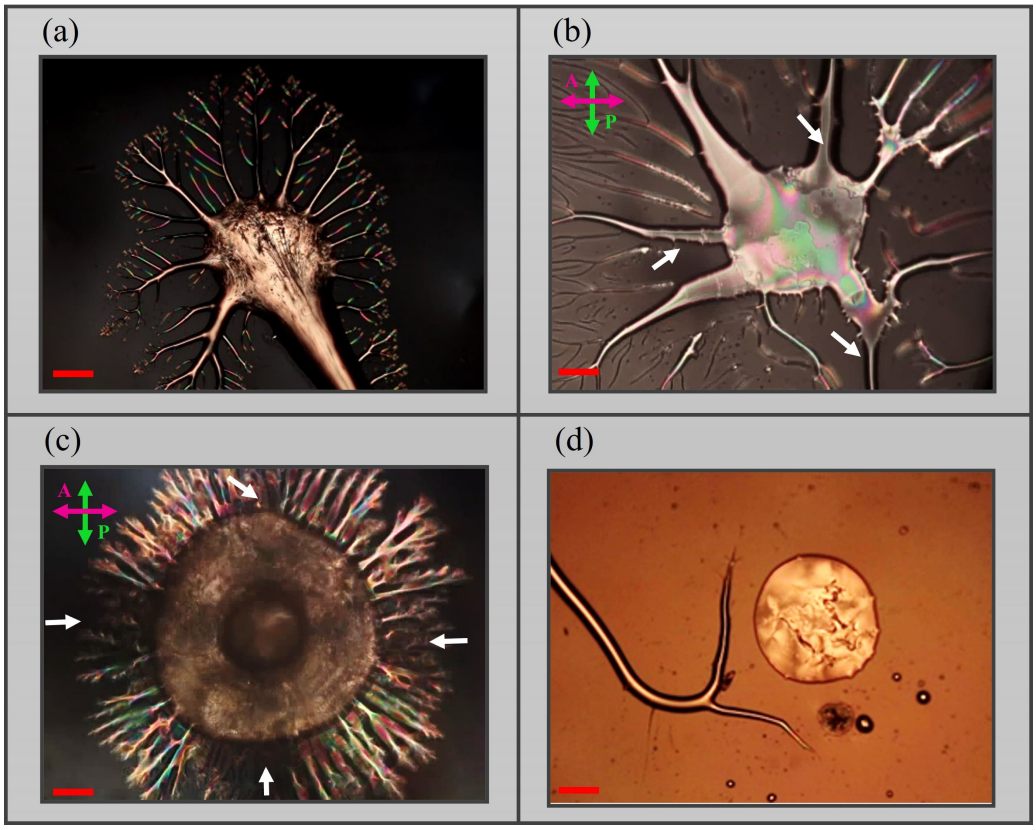

Figure 4.7: Gallery of images describing various features of RM734 jets. (a) RM734 jets ejected during an instability event on an undoped $LiNbO_3$ substrate, showing consecutive branching and mutual repulsion. (b and c) PTOM images of RM734 jets ejected during instability events on undoped $LiNbO_3$ substrates, showing that jets aligned along either the analyzer or the polarizer appear dark (white arrows) and demonstrating that the director **n** and polarization **P** are both aligned along the main axis of the jet. (d) RM734 jets on an iron-doped $LiNbO_3$ substrate deflecting to avoid a second RM734 droplet.

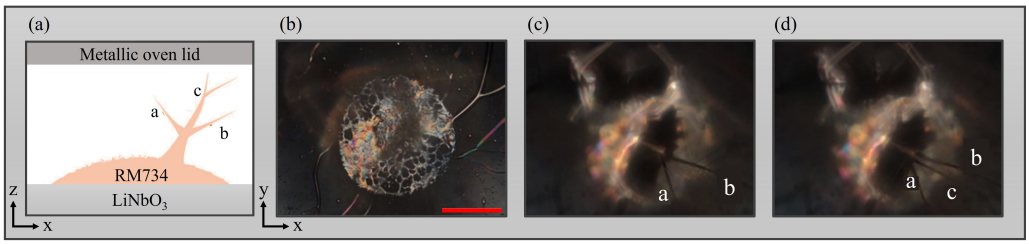

Figure 4.8: 3D jet ejection. (a) Scheme of a side view of a RM734 droplet laying on a $LiNbO_3$ surface exploding towards the oven lid. (b-d) Consecutive frames of an uncommon 3D explosion, occurring at low temperature after several conventional 2D explosions. Letters marks the obtained vertical jets in both the scheme and the pictures. Time between frames $40ms$, scale bar $500\mu m$

Since the N_F phase is monotropic, all the presented results are collected upon cooling from the I phase; however, if a crystallized RM734 droplet is heated, is it possible to observe brief jet ejection during the C-N phase transition, suggesting that a ferroelectric-like ordering can be transiently obtained before entering in the N phase. Temperature variations are fundamental to produce the instability, indeed, if T is fixed or changed with a small rate, the explosions are prevented even if strong, but constant, thermal gradients are introduced removing the oven lid. The need of thermal variations are a proof that surface charge density of LiNbO3 is not sufficient to induce instability into RM734 droplets and that the presence of lithium niobate pyroelectricity is required. Thermal gradients, however, can generate additional in-plane field component, modifying the jet kinetics; indeed, from the observations, with a high T homogeneity, seems that ejected jets move with a smaller velocity, but a precise characterization of this phenomenon has not been performed yet.

4.4 Discussion

4.4.1 Fringing field

Rayleigh instability, in which liquid droplets suddenly eject fluid jets when charged over a certain threshold, is probably the closest example to the explosive behaviour of ferroelectric nematic RM734 sessile droplets deposited on lithium niobate crystals. An example of this behaviour is provided by electrospray and charged levitated droplets[6], here fluid jets are produced from points of the droplet surface in which a curvature increase and a charge accumulation lead to the creation of tips, inducing the formation of secondary droplets. In the considered system, since free charges are not present, the whole process is provoked by the interplay between the bulk polarization of the N_F phase and the one of the ferroelectric crystal. Since the dimensions of the $LiNb_3$ substrate are finite, the pyroelectric effect produces a fringing electric field $\mathbf{E}_f$, as schematized in Fig. 4.9a; its direction is mainly in the vertical direction and its magnitude is a small fraction f, of the internal field σ_{LN}/ϵ_0, which depends on the finite crystal size and is $f \approx 10^{-3}$[33].

In a nematic ferroelectric droplet, generally, $\mathbf{P}$ structures itself parallel to the droplet surface, in order to minimize the electrostatic energies produced; doing so the system minimizes the non-zero $\nabla \cdot \mathbf{P}$ deformations which would result in a space charge accumulation. When a droplet is deposited onto a surface, a nearly planar orientation of the molecules at the solid-liquid interface is expected. If an external field – like the lithium niobate fringing field $\mathbf{E}_f$ – is applied, the liquid crystal molecules, and thus $\mathbf{P}$, slightly reorient, polarizing the droplet upon the accumulation of surface charges (in the order of $\sigma \approx f\sigma_{LN} \approx 10^{-3}\mu C/cm^2$) and eliminating the internal field. The role of fringing field has been confirmed using geometries realized to maximize it (e.g. depositing a droplet near the edges of the solid substrate); when such geometries are used, as shown in Fig. 4.10, much more violent explosions are observed.

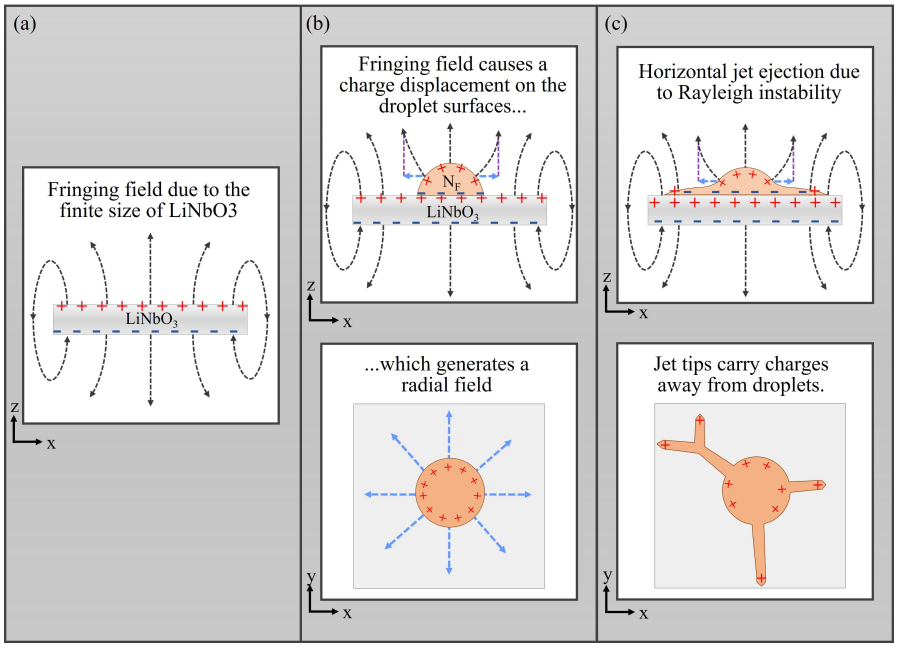

Figure 4.9: Sketch of a fringe field- induced explosion of a RM734 droplet. (a) Sketch of the fringing field of a finite $LiNbO_3$ slide. (b) Sketch of the bound charges and polarization field of a sessile RM734 droplet induced by the fringing field of the $LiNbO_3$ slide. The radial component obtained is represented with blue arrows (c) Sketch of the jet ejection, drove by the radial field

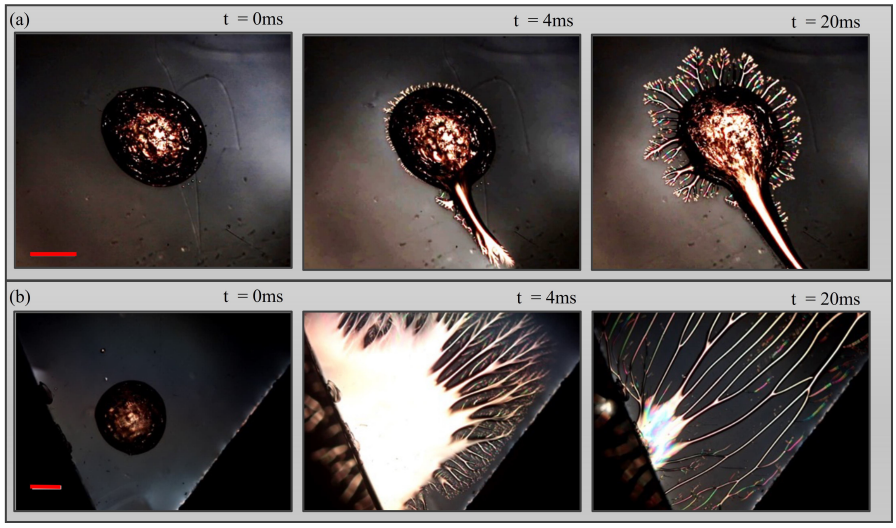

Figure 4.10: Different explosions induced by fringing field of different magnitude. The two droplets have a similar size ($2R = 1200\mu m$) and deposited on two different positions of the same $LiNbO_3$ slide. (a) Instability events of a RM734 droplet in the center of the slide where the fringing field is minimum. (b) Instability events of a RM734 droplet in the corner of the slide where the fringing field is maximum. Scale bar = $500\mu m$

4.4.2 Contact angle

The charges deposited on the surfaces, as represented in Fig. 4.9b, are of opposite sign at the two different interfaces and large enough to compensate the polarization charge of the lithium niobate substrate; this charge density, however, is several orders of magnitude smaller than the spontaneous bulk polarization of the N_F phase of RM734 (Fig. 2.1b), suggesting that the reorientation of of a fraction of a degree is enough to screen $\mathbf{E}_f$ and thus probably occurring during the N-N_F transition. Furthermore, the lowering of surface tension, caused by the Coulomb repulsions between the bound charges deposited on the surface, can explain the observed sudden change in contact angle θ depicted in Fig 4.3a at the transition between the two nematic phases. Indeed, assuming that the liquid-air surface tension is the only one showing significant variations and using the Young-Dupré equation[34]:

$$cos\theta = \frac{\gamma_{SA} - \gamma_{SL}}{\gamma_{LA}} \tag{4.1}$$

where γ_{SA} is the solid-air surface tension, γ_{SL} is the solid-liquid surface tension and γ_{LA} is the liquid-air surface tension, it is possible to estimate that a reduction in the contact angle θ from $60°$ to $30°$ corresponds to a decrease of the surface tension γ_{LA} of $\sim 25\%$. A basic quantification of the charge density required to induce the observed changes can be obtained considering the electrostatic energy U of a uniformly charged disk[35]:

$$U = \frac{8\pi}{3} k_C \sigma^2 R^3 \tag{4.2}$$

where k_C is the Coulomb constant while R is the disk radius, considered to be equal as the droplet. If a surface tension compatible with the one of conventional nematics[29,36], such as $\gamma \approx 3 \times 10^{-2} J/m^2$ (and thus $\Delta\gamma = 10^{-2} J/m^2$), is assumed, a value of $\sigma \approx 2 \times 10^{-3} \mu C/cm^2$ can be obtained; an analogous result is obtained ($\sigma \approx 10^{-3} \mu C/cm^2$) when considering a spherical or half-spherical shell, in good accordance with the expectations. Since the fringing field of the $LiNbO_3$ substrate is roughly independent on T in the considered range, a T-independent Coulomb effect on γ is equally expected as it can be roughly be seen in Fig. 4.3a.

4.4.3 Jets emission

When a droplet gets polarized in this way, thanks to its hemispherical shape, it produces an electric field possessing a planar (*xy*) radial component (Fig. 4.9b), capable of driving the ejected jets. In the observed cases, instabilities usually start at the rim of the droplet, involving the bulk only in later stages, probably suggesting that topological defects, which are easily formed on the surface, can be a zone of charge accumulation, acting as a trigger point for the jet ejection. For example, if during the process of polar ordering two opposite directions of $\mathbf{P}$ are trapped facing one against the other, a charged domain wall (represented with a red surface in Fig. 4.11a), capable of triggering the instability, is created. In all observed samples, indeed, is always possible to notice the spontaneous formation of various defect walls and lines during the N-N_F transition.

In domain walls of area S a charge $q = 2\mathbf{P}S$ is accumulated, producing an instability when the Coulomb force F_C becomes larger than F_S, the force arising from surface tension. These two forces can be extimated as:

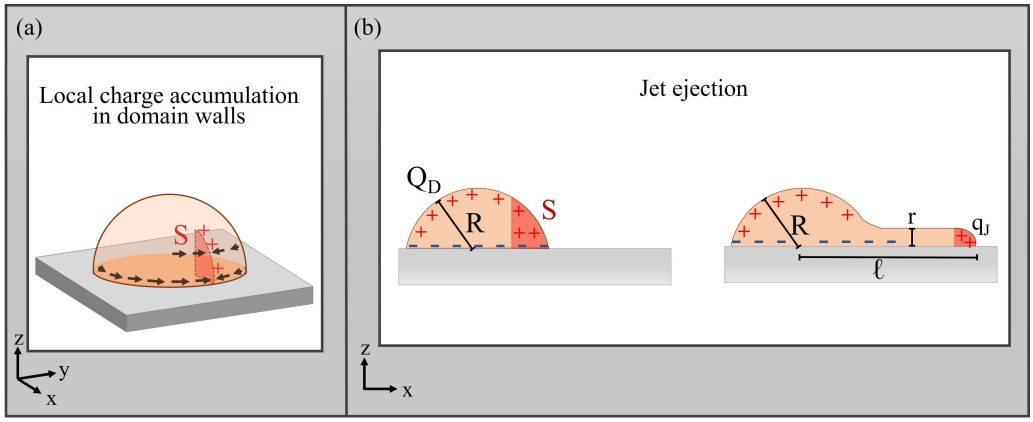

Figure 4.11: (a) Sketch of a possible charge accumulation on a domain wall caused by the contact of two different polarizations. (b) Relevant parameters used for theoretical considerations.

$$F_C = k_C \frac{qQ}{R^2} \tag{4.3}$$

$$F_S \approx \gamma\sqrt{S} \tag{4.4}$$

where $Q = \sigma A$ is the charge of a droplet of area A. F_S can be considered the force opposing the creation of a tip whose apex is the localized charge trying to escape the droplet. The first instability of Fig. 4.6 occurs with $\mathbf{P} \approx 2\mu C/cm^2$; assuming $\gamma \approx 10^{-2} N/m$ and $\sigma \approx 10^{-3}\mu C/cm^2$ it is possible to observe that F_C overcomes F_S when $S > 0.2\mu m^2$, an area much smaller than the droplet size. This indicates that the jets can be induced by the charge accumulated in very small regions.

Once the instability starts, it proceeds trough an explosive process favoured by the flow-induced orientational order of the director along the stream (Fig.4.7b and c) which increases the coulombic repulsion transporting the polarization charges to the jet tip. Indeed, considering a simplified hemicylindrical jet as the one in Fig. 4.11b, it is possible to compare the repulsive force experienced by the jet tip F_{Ct} with the one caused by the surface tension F_{St}:

$$F_{Ct} = k_C \frac{Qq_t}{\ell^2} \tag{4.5}$$

$$F_{St} = \gamma\pi r \tag{4.6}$$

in which ℓ and r are the length and the radius of the jet while $q_t = \mathbf{P}\pi r^2/2$ is the charge of the tip; from this comparison it can be noted that $F_{Ct} > F_{St}$ when:

$$P > 0.4 \times 10^{-5} \frac{\ell^2}{rR^2} \mu C/cm^2 \tag{4.7}$$

which is always verified in the presented observations (Fig. 4.3b, 4.4, 4.5, 4.7, 4.8, 4.10) where: $0.13mm < R < 0.6mm$, $10\mu m < r < 100\mu m$ and $0.2mm < \ell < 3mm$.

During their growth, jets develop in a complex way, following a combination of different factors, such as: surface interactions, local electric fields generated by other jets

and droplets, additional instabilities caused by the charge accumulation on tips, and possible effects provoked by thermal gradients. Jets usually running on the surface may be explained through a combination of the minimization of the energy required to expand its surface –which is lower when in contact with the $LiNbO_3$ substrate since $\gamma_{SL} < \gamma_{LA}$– and the presence of the radial electric field, arising from the polarization of the droplet. Furthermore, a decrease in T corresponds to an increase in $\mathbf{P}$ (Fig. 2.1b), leading to the accumulation of larges polarization charges and hence repulsive forces. A close inspection of the explosive events reveals the presence of various additional phenomena like a polarization reversal in jets once detached from their droplet, secondary droplets exhibiting either an attractive or a repulsive behaviour, sudden collective instabilities. The exact origin of this events has not been described yet, however they may be originated from non-trivial couplings between flow and polar ordering or from a specificity of the $LiNbO_3$ substrate and his thermal history.

4.5 Conclusions

Even though Rayleigh instability, in which conductive and dielectric liquid droplets break once a critical charge is reached, is a well-known and studied phenomenon [4–17], it has never been observed in neutral dielectric liquids.

In this chapter, a presentation of electrostatic instabilities, occurring when sessile droplets of the ferroelectric nematic liquid crystal RM734 are cooled on the surface of ferroelectric crystalline lithium niobate slide, has been given.

This new type of instability arises from the accumulation of polarization charges on the liquid-air interface, induced by the coupling between the polarizations of a liquid and a solid ferroelectric material. Indeed, when the temperature is lowered, the polarization of the N_F material increases together with polarization charges up to a point in which the coulombic repulsions can surpass the surface tension and induce the instability. This event appears as a sudden expulsion of polarized liquid crystalline jets, led by the electrostatic repulsion of their charged tips exerted by the droplet. These jets can further bifurcate and move undergoing a novel phenomenology of electrostatically dominated fluid motion.

The instability described in the current chapter can be considered to be closely dependent on the specific properties of the recently discovered N_F phase, such as the combination between huge spontaneous polarization coupled with fluidity.

This set of properties, together with new electro-optic and electro-mechanic phenomena, can produce body forces that can be exploited, once fully understood and controlled, to create new electrohydromechanical applications, such as soft robots.

Bibliography

[1] R. J. Mandle, S. J. Cowling, and J. W. Goodby. A nematic to nematic transformation exhibited by a rod-like liquid crystal. *Physical Chemistry Chemical Physics*, 19:11429–11435, 2017.

[2] X. Chen, E. Korblova, D. Dong, X. Wei, R. Shao, L. Radzihovsky, M. A. Glaser, J. E. Maclennan, D. Bedrov, D. M. Walba, and N. A. Clark. First-principles experimental demonstration of ferroelectricity in a thermotropic nematic liquid crystal: Polar domains and striking electro-optics. *Proceedings of the National Academy of Sciences*, 117:14021–14031, 2020.

[3] R. Barboza, S. Marni, F. Ciciulla, F. A. Mir, G. Nava, F. Caimi, A. Zaltron, N. A. Clark, T. Bellini, and L. Lucchetti. Explosive electrostatic instability of ferroelectric liquid droplets on ferroelectric solid surfaces. *Proceedings of the National Academy of Sciences*, 119(32):e2207858119, 2022.

[4] L. Rayleigh. Xx. on the equilibrium of liquid conducting masses charged with electricity. *The London, Edinburgh, and Dublin Philosophical Magazine and Journal of Science*, 14(87):184–186, 1882.

[5] C. B. Richardson, A. L. Pigg, and R. L. Hightower. On the stability limit of charged droplets. *Proceedings of the Royal Society of London. Series A, Mathematical and Physical Sciences*, 422(1863):319–328, 1989.

[6] D. Duft, T. Achtzehn, R. Müller, B. A. Huber, and T. Leisner. Rayleigh jets from levitated microdroplets. *Nature*, 421(6919):128–128, Jan 2003.

[7] T. Achtzehn, R. Müller, D. Duft, and T. Leisner. The coulomb instability of charged microdroplets: dynamics and scaling. *The European Physical Journal D - Atomic, Molecular, Optical and Plasma Physics*, 34(1):311–313, Jul 2005.

[8] A. I. Grigor'ev, A. N. Zharov, and S. O. Shiryaeva. Effect of the initial deformation of a charged drop on nonlinear corrections to critical conditions for instability. *Technical Physics*, 50(8):1006–1015, Aug 2005.

[9] M. I. Oh, A. Malevanets, M. Paliy, D. Frenkel, and S. Consta. When droplets become stars: charged dielectric droplets beyond the rayleigh limit. *Soft Matter*, 13:8781–8795, 2017.

[10] H. J. Krappe. Stability of a charged, conducting, spheroidal droplet. *Physica Scripta*, 93:024003, 2018.

[11] B. Almería, W. Deng, T. M. Fahmy, and A. Gomez. Controlling the morphology of electrospray-generated PLGA microparticles for drug delivery. *J Colloid Interface Sci*, 343(1):125–133, Oct. 2009.

[12] B. Almería and A. Gomez. Electrospray synthesis of monodisperse polymer particles in a broad (60nm–2µm) diameter range: guiding principles and formulation recipes. *Journal of Colloid and Interface Science*, 417:121–130, 2014.

[13] S. A. Malik, W. H. Ng, J. Bowen, J. Tang, A. Gomez, A. J. Kenyon, and R. M. Day. Electrospray synthesis and properties of hierarchically structured plga tips microspheres for use as controlled release technologies. *Journal of Colloid and Interface Science*, 467:220–229, 2016.

[14] J. N. Smith, R. C. Flagan, and J. L. Beauchamp. Droplet evaporation and discharge dynamics in electrospray ionization. *The Journal of Physical Chemistry A*, 106(42): 9957–9967, 2002.

[15] J. Xie, J. Jiang, P. Davoodi, M. Srinivasan, and C.-H. Wang. Electrohydrodynamic atomization: A two-decade effort to produce and process micro-/nanoparticulate materials. *Chemical Engineering Science*, 125:32–57, 2015. Pharmaceutical Particles and Processing.

[16] W. Jung, Y.-H. Jung, P. V. Pikhitsa, J. Feng, Y. Yang, M. Kim, H.-Y. Tsai, T. Tanaka, J. Shin, K.-Y. Kim, H. Choi, J. Rho, and M. Choi. Three-dimensional nanoprinting via charged aerosol jets. *Nature*, 592(7852):54–59, Apr 2021.

[17] L. G. Fel and Y. Zimmels. Rayleigh instability in liquid-crystal jets. *Journal of Experimental and Theoretical Physics*, 98(5):960–973, May 2004.

[18] X. Yang and Q. Wang. Capillary instability of axisymmetric, active liquid crystal jets. *Soft Matter*, 10:6758–6776, 2014.

[19] X. Chen, Z. Zhu, M. J. Magrini, E. Korblova, C. S. Park, M. A. Glaser, J. E. Maclennan, D. M. Walba, and N. A. Clark. Ideal mixing of paraelectric and ferroelectric nematic phases in liquid crystals of distinct molecular species. *Liquid Crystals*, 49 (11):1531–1544, 2022.

[20] A. Zaltron, M. Bazzan, N. Argiolas, M. V. Ciampolillo, and C. Sada. Depth-resolved photorefractive characterization of lithium niobate doped with iron by thermal diffusion. *Applied Physics B*, 108(3):657–663, Sep 2012.

[21] L. Vittadello, A. Zaltron, N. Argiolas, M. Bazzan, N. Rossetto, and R. Signorini. Photorefractive direct laser writing. *Journal of Physics D: Applied Physics*, 49:125103, 2016.

[22] S. Sanna and W. G. Schmidt. $LiNbO_3$ surfaces from a microscopic perspective. *Journal of Physics: Condensed Matter*, 29:413001, Sep 2017.

[23] S. M. Kostritskii, O. G. Sevostyanov, M. Aillerie, and P. Bourson. Suppression of

photorefractive damage with aid of steady-state temperature gradient in nominally pure linbo3 crystals. *Journal of Applied Physics*, 104(11):114104, 2008.

[24] P. Ferraro, S. Grilli, L. Miccio, and V. Vespini. Wettability patterning of lithium niobate substrate by modulating pyroelectric effect to form microarray of sessile droplets. *Applied Physics Letters*, 92(21):213107, 2008.

[25] S. M. Kostritskii, M. Aillerie, and O. G. Sevostyanov. Self-compensation of optical damage in reduced nominally pure linbo3 crystals. *Journal of Applied Physics*, 107 (12):123526, 2010.

[26] T. Gebre, A. K. Batra, P. Guggilla, M. D. Aggarwal, and R. B. Lal. Pyroelectric properties of pure and doped lithium niobate crystals for infrared sensors. *Ferroelectrics Letters Section*, 31(5-6):131–139, 2004.

[27] R. L. Byer and C. B. Roundy. Pyroelectric coefficient direct measurement technique and application to a nsec response time detector. *Ferroelectrics*, 3(1):333–338, 1972.

[28] S. Bonfadini, F. Ciciulla, L. Criante, A. Zaltron, F. Simoni, V. Reshetnyak, and L. Lucchetti. Optofluidic platform using liquid crystals in lithium niobate microchannel. *Scientific Reports*, 9(1):1062, Jan 2019.

[29] M. G. J. Gannon and T. E. Faber. The surface tension of nematic liquid crystals. *Philosophical Magazine A*, 37(1):117–135, 1978.

[30] F. Mugele and J.-C. Baret. Electrowetting: from basics to applications. *Journal of Physics: Condensed Matter*, 17:R705, 2005.

[31] M. T. Máthé, A. Buka, A. Jákli, and P. Salamon. Ferroelectric nematic liquid crystal thermomotor. *Phys. Rev. E*, 105:L052701, May 2022.

[32] F. Caimi, G. Nava, R. Barboza, N. A. Clark, E. Korblova, D. M. Walba, T. Bellini, and L. Lucchetti. Surface alignment of ferroelectric nematic liquid crystals. *Soft Matter*, 17:8130–8139, 2021.

[33] G. J. Sloggett, N. G. Barton, and S. J. Spencer. Fringing fields in disc capacitors. *Journal of Physics A: Mathematical and General*, 19:2725, 1986.

[34] M. E. Schrader. Young-dupre revisited. *Langmuir*, 11(9), 1995.

[35] O. Ciftja. A result for the coulomb electrostatic energy of a uniformly charged disk. *Results in Physics*, 7:1674–1675, 2017.

[36] V. A. Korjenevsky and M. G. Tomilin. Experimental investigation of the surface energy of a nematic liquid crystal. *Liquid Crystals*, 15(5):643–649, 1993.

Part IV

RM734 confined into microchannels

CHAPTER 5

Superscreening and polarization control in linear microchannels

5.1 Introduction

In the present chapter, the interplay between the recently discovered ferroelectric nematic phase N_F [1–4] and applied external electric fields $\mathbf{E}$ is investigated.

This coupling with electric fields is considerably different from the dielectric response of common nematics; however, these differences have not yet been fully investigated. The diversity arises because of the presence of a spontaneous polarization that can be easily reoriented in the presence of $\mathbf{E}$. Indeed, in a conventional N material, the director, thanks to the dielectric anisotropy of nematic liquid crystals, experiences a quadrupolar coupling with electric fields which can generate a torque τ on the molecule proportional to $\mathbf{E}^2$ and with a strength comparable to orientational elasticity; in a N_F material, instead, the presence of a spontaneous bulk polarization implies a dipolar coupling with electric fields and self-interactions, caused by the accumulation of space charges every time a divergence of $\mathbf{P}$ is present, which can produce electric torques that are orders of magnitude larger than the elasticity of the material. This unconstrained rotation of $\mathbf{P}$ is indeed only limited by the elasticity caused by the non-perfect orientation and by the electrostatic forces produced by the polarization charges deposited both on the confining surfaces ($\sigma_p = \mathbf{P} \cdot \mathbf{u}$ where $\mathbf{u}$ is a unit vector representing the normal direction to the surface) and in the bulk ($\rho_P = -\nabla \cdot \mathbf{P}$). These features describe a complete new type of fluid, with properties differing from both nematic liquid crystals and ferroelectric crystals, in which the polarization, being intimately connected with the crystalline unit cell, is fixed in certain directions.

To evaluate the interplay of $\mathbf{P}$ and $\mathbf{E}$, the N_F material has been confined into differently-shaped microchannels dug into bulk glass and connecting two gold electrodes, a detailed view on the fabrication process is presented in the next section. All channels, as represented in Fig 5.1a, possess a rounded square cross-section of width $w = 35\mu m$ and a length $\ell = 1mm$, but are different in shape, bending in order to have a central section forming different angles with the direction connecting the electrodes (Fig 5.1b): $0°$ (straight, I-shaped channel), $90°$ (L-shaped channel), $135°$ (Z-shaped channel), $180°$ (S-shaped channel). A ferroelectric nematic material, indeed, once confined into a channel, should align with $\mathbf{P}$ parallel to it in order to accumulate the least amount of bound charges on the surfaces and hence minimize its overall electrostatic energy, a feature which could result in captivating implications once a bent channel is considered.

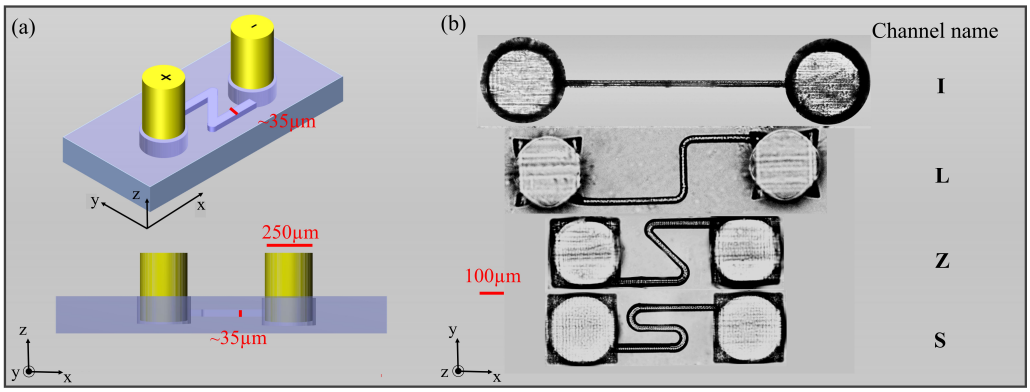

Figure 5.1: (a) Sketch of the microchannels buried in fused silica glass. Gold wires, used as electrodes, are represented as yellow cylinders (b) Microscopy images of the four considered channels, having the central section forming different angles with the direction connecting the electrodes.

5.2 Materials and methods

The liquid crystal mesogen RM734, has been used to fill, with the aid of a vacuum oven, four different microchannels, imaged in Fig. 5.1b, whose fabrication has been performed as follows.

5.2.1 Channel fabrication

Microchannels were produced with a technique called FLICE, which stands for "Femtosecond Laser Irradiation followed by Chemical Etching"[5,6]; this is a 2-step process comprising a first irradiation with a powerful laser source followed by a chemical etching which selectively removes the irradiated zones.

Channels are realized in $1mm$-thick fused silica glass slides (Corning HPFS 7980) which are irradiated using a a cavity-dumped diode-pumped Yb:KYW laser, a pulsed source with pulse duration of $\sim 300fs$, repetition rate of $1\ MHz$ and an emission wavelength of $1030nm$. The second harmonic of the beam ($515nm$) is focused into the bulk of the glass using a $63x$, $0.75NA$ microscope objective, whose spherical aberration is compensated with a correction ring. A power of $280mW$ is used, while the glass slide is scanned with a velocity of $1mm/s$ using a high precision three axis stage. The holes for the access of the electrodes were irradiated, from bottom to top, drawing circular helices, with a diameter of $280\mu m$, a pitch of $5\mu m$ and an height of $850\mu m$, while the channels are irradiated, at a depth of $300\mu m$ into the glass, drawing 9 parallels lines, with a separation of $2\mu m$.

The irradiated slide is then submerged into a $20\%v/v$ solution of hydrofluoric acid (HF) in water and mildly stirred for 45 minutes at $35°C$ in order to quickly etch the electrode holes and then soaked for 30 hours to a $10M$ water solution of potassium hydroxide (KOH) to precisely etch the channel. This combination of etchants has been chosen to combine the benefits of the fast (but unselective) etching of HF and the slow etching of KOH allowing to obtain a roughly constant cross-section in the channel[7]. This process introduces a roughness onto the channel surfaces which can be reduced from $50nm$ to $19nm$ upon thermal annealing[8]. In this process the glass slide is heated

up to $800°C$ with a rate of $200°C/h$, maintained there for 10 hour and then heated again up to $1215°C$, where is maintained for 25h prior to cooling back to RT.

In order to ensure planar alignment[9] channel surfaces were silanized using hexadecyltrimethoxysilane (HDTMS). With the aid of an ultrasonic bath, used to prevent flow-induced directional biases, microchannels has been soaked for 7 minutes into a solution prepared dissolving $2\%v/v$ of HDTMS in a 95:5 mixture of ethanol and water, previously acidified to pH 5 with acetic acid and let react for 5 minutes at RT. After the soaking, the chip is heated with a hot plate at $110°C$ for 10 minutes and used the following day after resting at RT. Prior to usage the channels are rinsed with ethanol in a ultrasonic bath for 2 minutes.

5.2.2 Transmitted light intensity measurements

Transmitted light intensities were measured, with cross polarizers either inserted (I_P, I_{P45}) or removed (I_S, I_{S0}), recording high frame per second videos ($400FPS$) using a CMOS microscope camera. Data are extracted from a $30 \times 30\mu m^2$ region of the channel aligned with the polarizer (and hence dark in its stable state between cross polarizers), centering it on the interface nucleation region when analyzing the central branches or at the central point when analyzing side branches. The intensity between cross polarizers I_P has been normalized with the maximum intensity of the same region aligned at $45°$ respect of the polarizer, I_{P45}, while the intensity without polarizers I_S has been normalized with the maximum intensity in the same region at the instant t_0, I_{S0}. All the reported measurements are the result of averaging three different negative-to-positive switches and three positive-to-negative switches.

5.2.3 Interface velocity measurements

During the switching of an electric field **E** applied to RM734-filled microchannels, two interfaces are generated in the central portion of the channel, moving towards the electrodes; their velocity v_i has been measured recording, using a CMOS microscope camera, high-frame rate videos ($500FPS$) which are analyzed with a tracking-edge MATLAB script.

The movies are taken in the central portion of the channel, aligned along the polarizers in order to have a dark state at the equilibrium between the switches and the region of interest is placed starting from the interface nucleation spot, recording the motion of a single interface at time. v_i is obtained using a MATLAB script working as follows. First an intensity profile is created for every frame upon averaging the intensity along the width, in a normal direction to the channel main axis, obtaining a nearly constant value during the equilibrium, changing with a switching event in which the interface position is marked by a step-like increase in brightness (Fig. 5.2a). In the shown example the brightness of the dark state is ≈ 1000 (blue), roughly uniform during the equilibrium, while the moving interface is represented a sudden change from ≈ 1000 to ≈ 8000 (blue to red). Using a threshold, the interface position is defined in every frame (Fig. 5.2b) and successive switching events are collapsed making them start from a common origin (Fig. 5.2c). Averaging these curves it is possible to notice that the motion of the interface is approximately linear in the first instants after its formation (Fig.5.2d). The linear region is then fitted and v_i, assumed constant, is extracted.

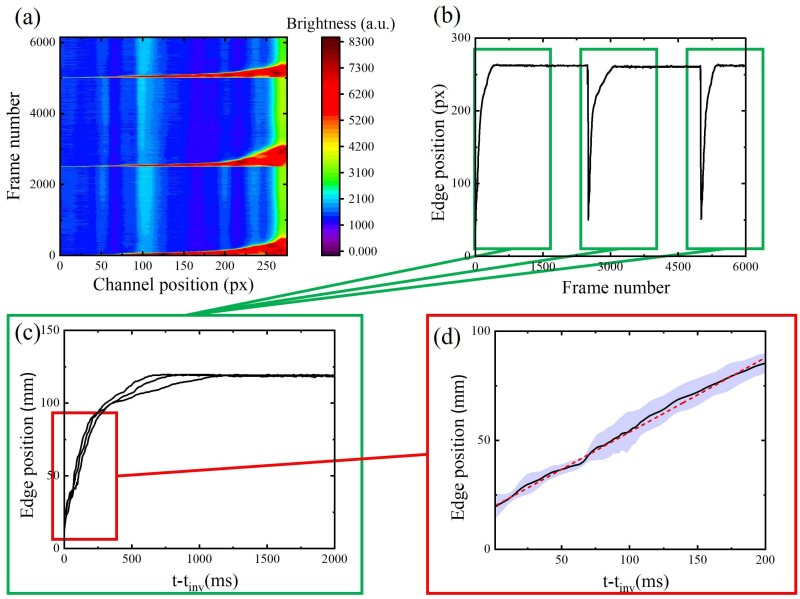

Figure 5.2: (a) space-time representation of the intensity in the central part of a channel. (b) Position of the interface during three switching events. (c) Comparison of the interface position in three distinct switching events. (d) average of the first portion of the three interface positions curves and linear fitting curve (dashed red line), v_i is extracted as the slope of the fitting curve.

5.2.4 Numerical simulations of ferroelectric fluids confined into microchannels

To understand the behaviour of the ferroelectric liquid crystalline material once confined into a microchannel different numerical simulations have been performed by Professor Mattew Glaser at the Colorado University of Boulder. The ferroelectric polarization $\mathbf{P}$ is considered to have a constant magnitude P_0 but can rotate so that $\mathbf{P} = \mathbf{P}(\mathbf{r}) = P_0\mathbf{p}(\mathbf{r})$, being $\mathbf{p}(\mathbf{r})$ a unit vector parallel to the nematic director $\mathbf{n}$. Furthermore the z dimension is considered negligible with respect to the x and y dimensions, making all quantities ($\mathbf{P}$, $\mathbf{E}$, ρ) independent of z and confining $\mathbf{P}$ and $\mathbf{E}$ to the x-y plane ($E_z = 0$ and $P_z = 0$). The assumption on z is required to produce a a computationally tractable quasi-2D model capable of representing the general physics of a ferroelectric nematic material confined into a microchannel. The free energy density of the N_F phase can be obtained summing orientational elastic and electrostatic contributions:

$$f(x, y) = f_{elast}(x, y) + f_{elect}(x, y) \tag{5.1}$$

The orientational elastic free energy has been calculated using the one-elastic-constant approximation of the Frank-Oseen equation:

$$f_{elast} = \frac{1}{2}K|\nabla\theta|^2 \tag{5.2}$$

where K is the elastic constant for both splay and bend deformations and θ is the orientation of $\mathbf{p}$ in the $x - y$ plane. The electrostatic free energy density has been calculated as:

$$f_{elect} = -\mathbf{P} \cdot \mathbf{E} = -P_0(E_x cos\theta + E_y cos\theta) \tag{5.3}$$

considering **E** the total electric field generated from both free and bound charges. Upon functional minimization, realized using a relaxation method, it is possible to obtain the equilibrium structure; after defining various θ on a discrete grid with grid spacing $a = 1.5\mu m$, the equations of motion are solved, for every timestep, from setting the total torque τ (arising from elastic, electrostatic and viscous forces) to zero using an explicit Euler time-stepping scheme. Furthermore, to get a more similar model of the real channels, a homogeneous roughness of amplitude $\delta = 0.76\mu m$ has been introduced into the channel boundaries. The three different torques can be calculated as:

$$\tau_{elast} = K\nabla^2\theta \tag{5.4}$$

$$\tau_{elect} = (\mathbf{P} \times \mathbf{E}) \cdot z = P_0(E_y cos\theta - E_x sin\theta) \tag{5.5}$$

$$\tau_{visc} = -\gamma\delta\theta/\delta t \tag{5.6}$$

where γ is the rotational viscosity. To realize the simulated channels a geometry matching, in the $x - y$ plane, the one of the real channels has been considered. For computational expediency a potential difference $\Delta V = 1000V$ ($\sim 10^3$ times higher than the one used in real experiments); using this ΔV the entire processes are indeed complete within $500\mu s$.

The simulation protocol has been realized in order to minimize the dependence on initial conditions and comprises three different steps: (1) the system is initialized with a completely random polar director field, assigning a random value in the range $-\pi$ an π; (2) the system is let evolve for $510\mu s$ under a constant potential difference of $-1000V$ between the two channel terminals; (3) the sign of the potential difference is changed to $+1000V$ and the system is let evolve for other $500\mu s$. The reported results are obtained after the step (3) and can be assumed as a qualitative model for the experimental switching dynamics. In this model, the electrodes free charge are represented as a uniform and opposite charge density placed at the channel ends, which can be scaled at each time-step to maintain a constant potential difference ΔV between the two terminals. Full theoretical details and computational methods can be found in the supporting information of[10]

5.3 Experimental results

5.3.1 Response to static fields

When the microchannels are filled with RM734, if a voltage ΔV is not applied between the electrodes, only a partial alignment along the channel is obtained in both N and N_F phases (Fig 5.3a), probably caused by a residual roughness of the channel surfaces. Instead, when a potential difference ΔV is applied, a "nominal" electric field $\mathbf{E_0} \equiv \Delta V/\ell$ is generated; no significant effects are present in the nematic phase for fields up to $\mathbf{E_0} \approx 50V/mm$, while, in the ferroelectric nematic phase, an electric field as low as $\mathbf{E_0} \approx 0.25V/mm$ produces a virtually perfect alignment in every tested geometry (Fig. 5.3b). In order to exclude the presence of discontinuities in the **P** direction such as defect walls or lines, a detailed inspection of the channels has been conducted, focusing on both the curved sections (Fig. 5.3c) and the regions in which **P** should be oriented against the electrode-to-electrode direction expected for $\mathbf{E_0}$, without finding any trace of discontinuity. This complete continuity indicates that both the nematic director **n**

and the polarization **P** are always parallel to the channel walls, continuously following the channel, regardless of its shape (Fig.5.3d). Furthermore, this continuity of **n** and **P** implies that **E** must possess an analog continuity along the channel rather than being oriented along the trivial direction connecting the electrodes as in a conventional dielectric media. This behaviour can be seen as an analogy of what happens in a conventional bent conductive wire, in which free charges can be accumulated at the surfaces, driving the electric field along the wire, independently of its route; in a N_F material, indeed, this same effect could be achieved through bound charges.

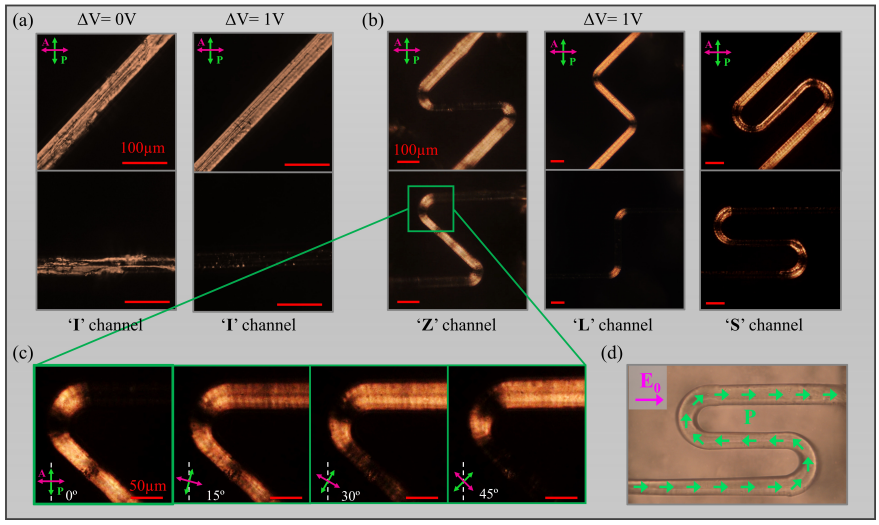

Figure 5.3: (a) PTOM images of the RM734-filled "I" channel, without and with an applied voltage $\Delta V = 1V$. (b) PTOM images of the considered "bent" geometries while a potential difference $\Delta V = 1V$ is applied. (c) Enlargement of curved section of a "Z" channel, imaged at different angles respect of the polarizers (d) Sketch of the proposed continuity of **P** direction (green arrows) within a "S" channel, showing that in the central section the polarization is oriented against the nominal applied electric field $\mathbf{E_0}$.

5.3.2 Ferroelectric superscreening

This continuity of **P** and **E** along the channel can be explained as a result of the orientational freedom of **P** in N_F, which allows an immediate accumulation of bound charges onto the surfaces capable of eliminating any component of **E** normal to the boundaries, making it always parallel to the channel axis. This phenomenon, renamed *ferroelectric superscreening*, is schematized in Fig.5.4.

The bare channel, without the ferroelectric material, when immersed in a transverse electric field $\mathbf{E_{0\perp}}$ behaves as a capacitor, possessing a dielectric constant ϵ and a capacitance per unit of length C (Fig 5.4a). When the ferroelectric liquid crystal is added, a new bulk polarization field **P** is present (Fig 5.4b); this polarization field has the remarkable properties of being reorientable, due to its liquid crystalline nature, and spontaneously spatially uniform, to minimize polarization space charges in the bulk [11]. Every variation of **P** from the parallel direction to the channel axis ($\psi \neq 0$) results in the deposition of a polarization surface charge per every unit length $\lambda = wPsin\psi$, where w is the channel width. This charge produces an electric field $E_p(\psi)$ inside the channel which generates a torque density trying to prevent the reorientation; this can be considered as an

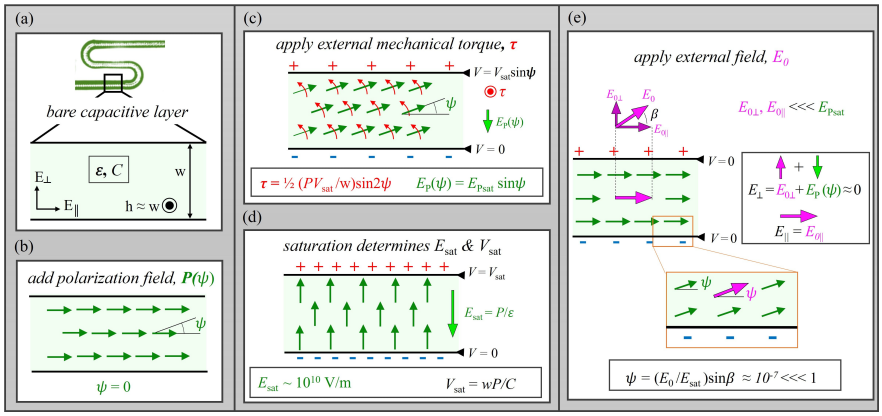

Figure 5.4: Sketch of the ferroelectric superscreening in a microchannel. (a) The empty channel possess a capacitance/length C, which can be obtained as a ratio between the potential difference along the channel V and λ, the charge along each edge per unit length of the microchannel, so that $\lambda = CV$. (b) Since the polarization field $\mathbf{P}(\psi)$ is locally oriented along the nematic director $\mathbf{n}$, its spatial variations are controlled by both the nematic elasticity and the coupling between $\mathbf{P}$ and electric fields. Being the ratio $\sqrt{\epsilon K}/P$, with K a Frank elastic constant, very small, the electrostatics is predominant, making $\mathbf{P}$ uniform with an orientation ψ which is responsive, as a spatially uniform field, towards external torques. (c) If a external ψ-independent mechanical torque τ is applied, a restoring electrostatic torque arising from the the polarization surface charge deposition on the confining boundaries. (d) If the polarization is placed perpendicular to the channel the maximum potential difference $V \equiv V_{sat}$ is obtained, which is, for the considered experimental conditions V_{sat} is in the order of 10^{-5}, producing an electric field $E_{sat} \sim 10^1 0v/m$, a field many order of magnitudes larger than the ones experimentally accessible. (e) In the typical experimental conditions, the microchannels are immersed in an electric field $\mathbf{E_0}$ which form an angle β with the channel main axis. This field can be decomposed in two components: $E_{0\parallel}$ running unaltered along the channel and $E_{0\perp}$ which is everywhere cancelled by superscreening. Since the applied fields $\mathbf{E_0}$ several orders of magnitude smaller than E_{sat}, the tilt angles ψ required to eliminate $E_{0\perp}$ are too small to be observed.

electrostatic spring which tries to take ψ back to 0 (Fig 5.4c). The stiffness of this electrostatic spring is extremely high and can be estimated considering the potential difference $V_{sat} = wP/C$, obtained at saturation when $\psi = 90°$ (Fig 5.4d). In the conditions explored in this chapter $V_{sat} \approx 10^5 V$, a value that makes nearly impossible to orient $\mathbf{P}$ perpendicular to the channel, considering the enormous electric fields that would be required.

In Fig 5.4e, a condition similar to the experimental one is considered: an external field $\mathbf{E_0}$ is applied with an angle β respect to the channel axis, generating a torque that rotates $\mathbf{P}$ and a second one, as in Fig 5.4c, that tries to oppose to the first. The torque balance is reached, in this case, when $E_\perp = 0$ within the channel, with $E_P(\psi)$ compensating $E_{0\perp} = 0$[12–14]. Considering the typical polarization of RM734 in N_F phase ($P \approx 6\mu C/cm^2$) and the magnitude of the used electric fields ($E_0 \approx 1V/mm$), submicroradians reorientations of $\mathbf{P}$ are enough to completely suppress any component of the electric field normal to the surfaces, leaving the material virtually parallel to the local channel axis in every point. This fast and strong screening effect, which eliminates the perpendicular components of E_0, is a peculiar property of the N_F phase; the name *ferroelectric superscreening* has indeed been chosen to underline the difference between this collective dipolar reorientation exhibited by the whole fluid and the conventional

screening effected by both free charges in conductors and dipoles in dielectrics. In the following experiments, ferroelectric superscreening locally eliminates the perpendicular electric field component, but further affects the global longitudinal components as a result of long-range interactions provoked by the altered mound charge distribution.

5.3.3 Field reversal experiments

In order to better investigate the role of bound charges in ferroelectric superscreening a study of the response of the confined N_F material once $\mathbf{E_0}$ is reverted has been performed. When ΔV is switched, indeed, the homogeneous planar alignment (as in Fig 5.5a) becomes suddenly unstable: the system breaks into micron-sized domains which tend to coalesce forming larger bright regions that evolve to another analogous homogeneous planar alignment (but with opposite polarity) through the motion of an interface (Fig 5.5b).

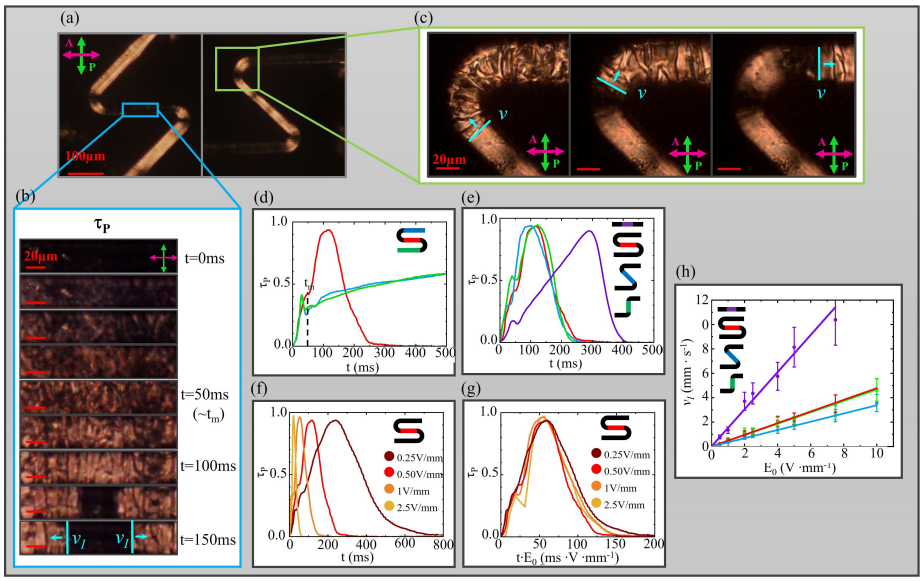

Figure 5.5: Ferroelectric nematic polarization switching in microchannels. (a) PTOM images, with different orientations, of a "Z" channel with $\Delta V = 1V$ applied. (b) Sequence of PTOM images showing the time evolution of the central part of a "Z" channel after the voltage inversion occurring at $t = 0$. In the images is it possible to observe the formation and coarsening of domains and the creation of the two homogeneous-defected interfaces moving with velocity v_i towards the electrodes. (c) Sequence of PTOM images showing the continuous motion of the homogeneous-defected interface along a curve of a "Z" channel with velocity v_i. (d) Time evolution of the transmittance between crossed polarizers $\tau_P(t)$ measured in three different sections of a "S" channel after the inversion of ΔV from 0.5V to -0.5V. (e) Time evolution of the transmittance between crossed polarizers $\tau_P(t)$ measured in the central section of all the different channels after the inversion of ΔV from 0.5V to -0.5V. (f) Time evolution of the transmittance between crossed polarizers $\tau_P(t)$ measured in the central section of a "S" channel channels after the inversion of different ΔV, resulting in different E_0. (g) Same data of the previous plot represented on the rescaled time $t \cdot E_0$. (h) Dependence of the velocity v_i of the homogeneous-defected interfaces as a function of the nominal applied electric field E_0, measured in the first moments after its formation.

This switching phenomena can be characterized measuring the intensity of the transmitted light, with the analyzer inserted (I_P) or removed (I_S), while keeping the polarizer inserted. These signals transiently change for a short period, whose length varies depending on ΔV. Transmitted intensities are recorded in the central portion of different branches aligned along the polarizers to start from a dark state in the case of inserted analyzer and from its maximum value in the case of removed analyzer and values have been separately normalized with I_{P_45} and I_{S_0}, which are respectively the maximum brightness recorded with the channel at $45°$ respect to the polarizer and the brightness in the equilibrium conditions; The two transmittances are thus $\tau_P(t) = I_P(t)/I_{P_45}$ and $\tau_S(t) = I_S(t)/I_{S_0}$. Unfortunately, due to the reduced section of the microchannels, the polarization current flowing through the electrodes could not be measured to compare with the transmittances, however an analogous measurement on a $20\mu m$-thick flat cell has been performed and shown in Fig 5.6, where is evident that electric switching occurs much faster than optical switching. This observation suggests that, in the channels, the homogeneous-defected interface separates a region in which the polarization has been completely reversed from another in which the reversal is incomplete, implying that this interface carries a polarization charge involved in its motion towards the electrodes, as explained in the next paragraphs.

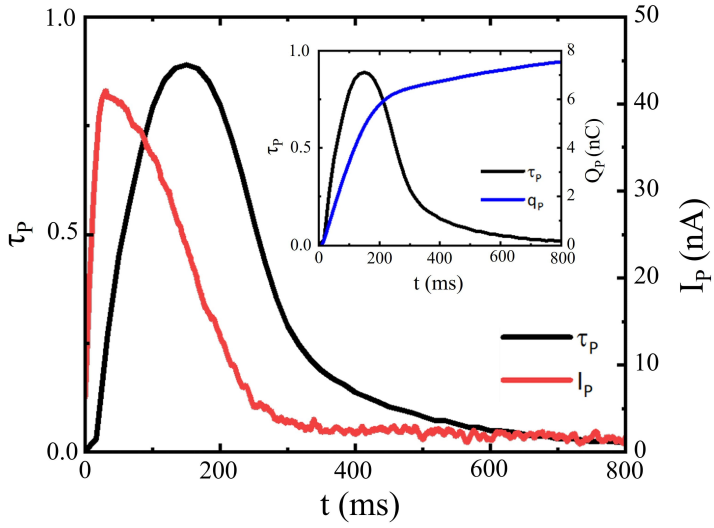

Figure 5.6: Comparison between electrical and optical switching in a Fluorolink covered flat cell. Time evolution of the transmittance between crossed polarizers $\tau_P(t)$ measured in the central portion of the cell (black curve) compared with the polarization current I_P flowing through the electrodes after the switching of a voltage ΔV from $0.5V$ to $-0.5V$ (red curve). In the inset a comparison between $\tau_P(t)$ and the total charge Q_P flowing through the electrodes, obtained integrating the current. Cell thickness is $20\mu m$, the width is $1cm$ and the electrode separation is $1mm$.

A combined inspection of both PTOM images and transmittances allows a deeper comprehension of the different steps of the multiscale switching process. When the inversion begins, at $t = 0$, the uniform texture breaks in a grainy irregular pattern made of micron-sized domains, in accordance with the idea of an inversion of $\mathbf{P}$ completed upon the rotation of the molecules in a multitude of different directions. As can be noted

respectively from Fig. 5.5d-g and Fig. 5.7b-e, this event is accompanied with both an increase in $\tau_P(t)$ due to the presence of twisted domains (Fig. 5.5b) and a decrease in $\tau_S(t)$ due to the scattering happening at the domain borders (Fig. 5.7a).

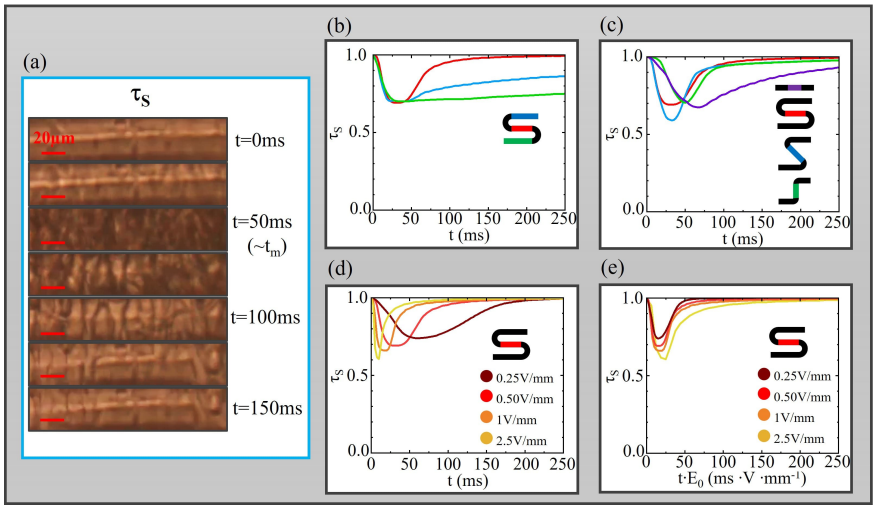

Figure 5.7: (a) Sequence of bright field images showing the time evolution of the central part of a "Z" channel after the voltage inversion occurring at $t = 0$. (b) Time evolution of the optical transmittance $\tau_S(t)$ measured in three different sections of a "S" channel after the inversion of ΔV from 0.5V to -0.5V. (c) Time evolution of the optical transmittance $\tau_S(t)$ measured in the central section of all the different channels after the inversion of ΔV from 0.5V to -0.5V. (d) Time evolution of the optical transmittance $\tau_S(t)$ measured in the central section of a "S" channel channels after the inversion of different ΔV, resulting in different E_0. (e) Same data of the previous plot represented on the rescaled time $t \cdot E_0$.

This disordering in the N_F texture increases up to a maximum before starting to decrease, as evident from Fig 5.7 in which the time evolution of $\tau_S(t)$ presents a minimum, and hence the maximum scattering, at the same time $t \approx t_m$ at which $\tau_P(t)$ shows a dent during its growth (Fig. 5.5d-g).

This time t_m indicates the transition between two distinct regimes, as revealed performing pulsed field reversals, in which the potential difference ΔV is inverted for short times, producing incomplete **P** reorientations (Fig 5.8). From this experiments is it possible to observe that, when ΔV is inverted for times $t_{inv} < t_m$ (green curves in Fig. 5.8), $\tau_P(t)$ relaxes back with a simple exponential decay, whose relaxation time is independent on t_{inv} but only on ΔV, while, if the voltage is inverted for times $t_{inv} > t_m$; instead, when $t_{inv} > t_m$ (blue curves in Fig. 5.8), the decay becomes much longer and irregular. This difference in behaviour is more evident in Fig. 5.8b where every $\tau_P(t - t_inv)$ is normalized for its maximum value $\tau_{Pmax}(t = t_inv)$; all the $t_{inv} < t_m$ green curves collapse onto the same exponential curve (pink dashed curve) while the $t_{inv} > t_m$ blue curves show longer non-exponential decays. This difference can be explained assuming that t_m is the point at which N_F domains have rotated enough to start reconnecting in the opposite direction, changing topology and forming new interactions that prevent a simple elastic relaxation following its own footsteps.

After t_m, in the reorganization regime, domains start merging, the texture smoothens and most of defect lines disappear, provoking another growth in $\tau_p(t)$ which, after reach-

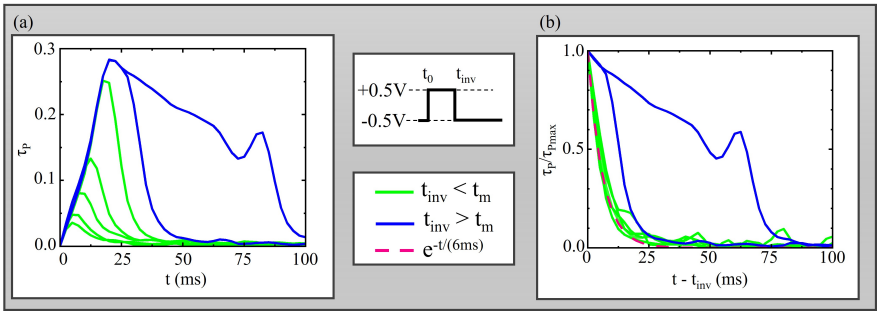

Figure 5.8: (a) Pulsed switching experiments preformed in the central section of a "Z" channel after the inversion of ΔV from -0.5V to 0.5V for different pulses of length t_inv (b) Decay of $\tau_P(t - t_{inv})$ normalized over its maximum value $\tau_{Pmax}(t = t_inv)$ at the inversion point, plots are represented after the peak of the graph in (a) is reached.

ing a maximum, decreases back to 0 once the molecules are uniformly oriented in the opposite direction. The new homogeneous polar ordering is obtained through a nucleation process typically starting in the center of the channel – probably being the narrowest portion of the channel due to the etching stage of the production process – and requires a combination of disentangling of topological defects, annihilation of defects with opposite charge and detachment of the molecules from the surface; this last, as can be inferred chapter 3 and in[9], is probably the final event happening. The nucleation produces two interfaces, separating the defected regions from the newly created defectless uniform region, which expands through their motion towards the electrode (Fig 5.5b and c) with a velocity v_i. The reversal of the polarization $\mathbf{P}$ involving the passage of a running interface implies an asynchronous completion of the switching, which is faster near the nucleation point (for example the red curve in Fig 5.5d and Fig. 5.7b) and much slower near the electrodes (blue and green curves in Fig 5.5d and Fig. 5.7b). A further analysis of $\tau_p(t)$ in different branches of the same channel reveals that the behaviour in the first regime ($t < t_m$) is the same in the whole channel (Fig 5.5d and Fig. 5.7b); analogous results are obtained for every channel shape. Comparing $\tau_p(t)$ in the various geometries (Fig. 5.5e and Fig. 5.7c) it is possible to notice that, for the central portion of every bent channel, if the same Δv is inverted during the switching, an equal trend is obtained for every regime; surprisingly this is not true for the simple "I" channel, which shows a slower rise and a steeper decay. The position of the dent in the growth t_m is instead essentially alike for all the four channels.

The whole switching process is completely controlled by electrical interactions, measuring $\tau_p(t)$ in the same portion of the same channel with different applied fields $\mathbf{E_0}$ (Fig. 5.5f and Fig. 5.7d), is it possible to notice that the entire kinetics becomes faster increasing ΔV in a proportional way, as becomes evident from the collapse of the curves in Fig. 5.5g and Fig. 5.7e then the time is rescaled with $\mathbf{E_0}$. The dent at $\tau_p(t_m)$ becomes more deep when increasing $\mathbf{E_0}$ (Fig 5.5g) due to an increased turbidity (Fig 5.7e), reflecting that with higher electric fields the switching occurs faster with the system breaking up in smaller domains, with their borders provoking an increased scattering of light.

This linear dependence of the polarity inversion on $\mathbf{E_0}$ suggest that $\tau_p(t)$ can be exploited as a proxy to estimate the local electric field $\mathbf{E_L}$ inside the channels. According to this logic, the identical growth of $\tau_p(t < t_m)$ in the different portion of the same channel hints that in the disordering regime the local field is uniform in the whole channel and

the equal shape of $\tau_p(t_m)$ in the central part of all bent channels, when w, ΔV and ℓ are the same, reveals that $\mathbf{E_L}$ is the same in the analogous samples.

Furthermore the nucleation of the moving interfaces occurs in the narrowest portions of the channels, suggesting that in that positions the local field is higher. A measurement of the velocity v_i of the interfaces for different ΔV reveals that this speed is constant in the first $100\mu m$ of movement and linearly proportional to the applied voltage (Fig. 5.5h). Again it is possible to notice that the velocity in all the bent channels is very similar in all bent channels and different in the simple "I" channel.

This dependence of v_i on ΔV suggest that this type of motion is driven by electrical forces and follows the local electric field $\mathbf{E_L}$, further confirming that its direction is always along the channel, regardless of its shape. In order to explain this motion the interfaces must possess an electrical charge, coherently with the aforementioned polarization charge arising from the junction between a homogeneous and a defected region, as shown in Fig. 5.6. Since v_i is constant for every ΔV, the interface motion must be opposed to a viscous-type friction force, probably reflecting the rotational viscosity of the domains, rotating to free the bulk volume from defects. A simplified model of this motion is presented in the following section.

5.3.4 Interface propagation model

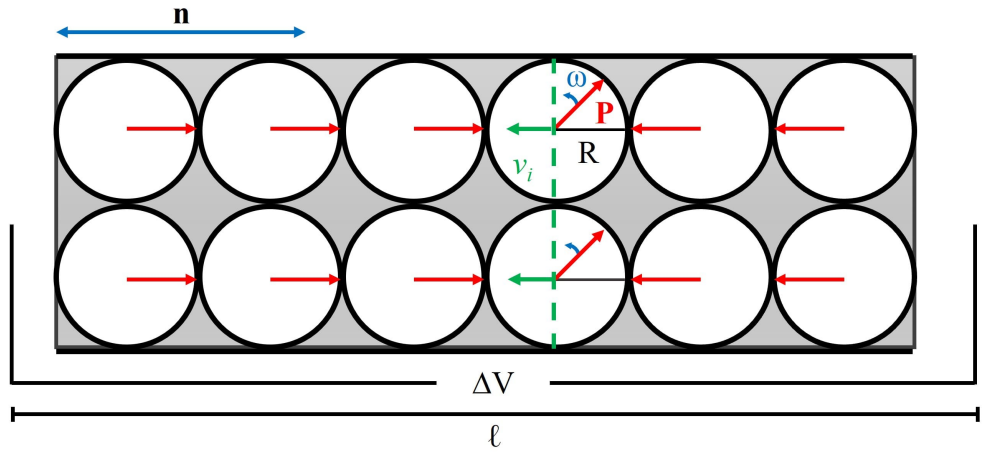

Figure 5.9: Sketch of the proposed model for the interface propagation. In the model the velocity v_i of the interface (green dashed line) is related to the liquid crystal rotational viscosity η. $\mathbf{n}$ is the non-polar nematic director at the equilibrium. The material is divided into circular domains of radius R and uniform polarization $\mathbf{P}$, which can rotate with an angular velocity ω. ℓ is the length of the channel and ΔV the applied voltage at its ends.

The uniform-defected interface moves with a constant velocity v_i which is proportional to the applied electric field $\mathbf{E_0}$. This behaviour corresponds to an electrophoretic mobility in which the electrostatic forces are balanced by an opposite viscous friction proportional to v_i. In order to correlate this type of viscous drag to the considered system, in which the bulk rotation, the annealing of defects and the surface switching produce the motion of a charged interface, a simple model has been proposed. As can be

seen in Fig. 5.5, the defected region of RM734 in N_F phase is composed by highly distorted domains that we assume to have all the same radius R. The motion of the interface involves the alignment of successive portions of the N_F phase in the direction of the applied field; this motion can be modeled as a succession of consecutive domain rotations, in a way that a certain domain can start its rotation only when the neighbouring one has completed its own, merging to the uniform N_F, as schematized in Fig.5.9. Assuming that each domain has to perform a rotation of $\pi/2$, completed in a time t_R, the velocity of the interface v_i can be calculated as the displacement of a domain size R in a time t_R:

$$v_i = \frac{R}{t_r} = \frac{2R\omega}{\pi} \tag{5.7}$$

where ω is the angular velocity of the domain, which can be obtained balancing the rotation-inducing electric torque τ_E and the opposite viscous torque τ_V. τ_E is considered to be constant and equal to the maximum torque experienced by $\mathbf{P}$ when forming an angle of $45°$ with $\mathbf{E} = \Delta V/\ell$:

$$\tau_E = \mathbf{P} \times \mathbf{E} \approx P\frac{4}{3}R^3\frac{\Delta V}{\ell}\frac{1}{\sqrt{2}} \tag{5.8}$$

in which P is the polarization and ℓ is the channel length. The viscous friction can be assumed to be the one of a sphere rotating in a viscous fluid:

$$\tau_V = 8\pi\eta R^3\omega \tag{5.9}$$

where η is the viscosity of the medium. Thus, balancing the torques is it possible to obtain:

$$\omega = \frac{P\Delta V}{\ell 6\sqrt{2}\eta} \tag{5.10}$$

which can be substituted in equation 5.7 to obtain:

$$v_i = \frac{R}{\pi}\frac{P}{3\sqrt{2}\eta}\frac{\Delta V}{\ell} \tag{5.11}$$

The experimental data are in the form:

$$v_i \approx A\frac{\Delta V}{\ell} \tag{5.12}$$

where A is in the order of $A \approx 10^{-6} m^2/sV$.

If a domain radius of $R \approx 10\mu m$ – as can be measured from PTOM observations – and a rotational viscosity $\eta \approx 5 \cdot 10^{-2} Pa \cdot s$ – as reported in [15] – are assumed, a velocity v_i can be estimated from this model as:

$$v_i \approx 0.4 \cdot 10^{-6}\frac{m^2}{sV} \tag{5.13}$$

Showing that the velocity of this type of electrophoretic motion observed is in the same order of magnitude of the one predicted by the simplified model and thus probably related to the liquid crystalline viscosity.

5.3.5 Continuum modeling of equilibrium structure and switching dynamics

The experimental observations and consequent considerations has been compared with the results of numerical simulations of the equilibrium structure and switching dynamics of a ferroelectric nematic liquid crystalline material confined into microchannels whose details are presented in the previous "Materials and methods" section. From these simulations it is possible to understand the general characteristics of the system both at equilibrium and during the switching process; for example in Fig. 5.10a some frames of the time evolution of the polarization **P**, the total charge density ρ (obtained as the sum of free and bound charges) and electric field **E** after the voltage inversion in a simulated "S" channel are shown. $P_{\parallel}$ and $E_{\parallel}$, the components of **P** and **E** parallel to the local channel direction, can be extracted upon averaging and, for the central section of the "S" channel under examination, plotted in Fig. 5.10b and c, where the coloured vertical lines correspond to the color-matching panels of Fig. 5.10a.

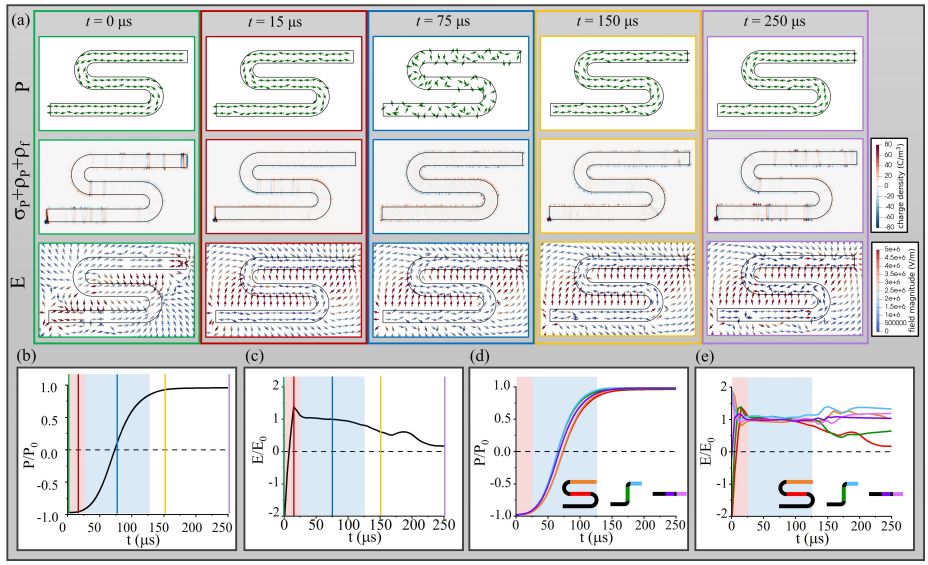

Figure 5.10: Results of simulated switching of N_F materials in microchannels upon the inversion of a the voltage on the electrodes. Starting condition is the equilibrium configuration for the opposite voltage. (a) Snapshot at different moments of the time evolution of polarization **P**, total charge $\rho = \sigma_P + \rho_P + \rho_f$, and electric field **E** in a "S" channel. For clarity **P** and **E** shown are only a fraction (1 in 196) of the total ones. (b) and (c) $P_{\parallel}(t)$ and $E_{\parallel}(t)$ averaged in the central section of the "S" channel shown in (a). Vertical coloured lines mark the times corresponding to the snapshots in (a) with matching colours. (d) and (e) $P_{\parallel}(t)$ and $E_{\parallel}(t)$ averaged in different regions of various channels, matching the colour code of the schematic legend. Red shading in panels (b)-(d) indicates the time interval of the field inversion while blue shading indicates the time interval of the polarization inversion.

Focusing on this example is it possible to notice that in the first instant after the potential difference reversal ($t = 0$) the electric field has an inhomogeneous intensity over the channel, with a relevant component perpendicular to the channel surfaces which is rapidly screened by a tiny reorientation of the polarization on the surfaces, as predicted by the superscreening effect. After $15\mu s$ (red lines and frames), indeed, the electric field has reversed its direction and becomes nearly uniform in magnitude ($\sim 1V/\mu m \equiv$

$1000V/mm$, the same intensity of the nominal applied electric field E_0). In the same time interval, the electric field outside the channel inverts its direction, provoking a change in sign of the bound charges at the channel boundaries. Analogous results are obtained for every position of all the different geometries, as shown in Fig. 5.10d and e, where it is possible to observe that the inversion of **E** (red shading) occurs much faster than the inversion of **P** (blue shading), that, in the same fraction of time, has remained nearly unchanged. Therefore, after the field inversion, **E** and **P** are in oriented in antiparallel directions and hence in an unstable configuration, inducing a reorientation of the polarization. Blue framed snapshots show the polarization state at time $t = 75\mu s$, in which $P_{\|} \approx 0$, revealing that even in the simulations **P** inversion happens through a disordered states created by the breaking of the uniform N_F alignment into small domains which minimize the energy cost provoked by the accumulation of surface and bulk bound charges. Remarkably, even though this polarization inversion occurs via a chaotic reorientation of **P**, $E_{\|}$ and σ remain nearly constant in the interval $t = 25 - 125\mu m$, the time required by $P_{\|}$ to nearly complete its inversion (blue shading), meaning that the reversal of **P** happens under the conditions of an uniform and constant electric field; a result found in every tested geometry (Fig. 5.10d and e). After the polarization inversion event a last stage of reorganization occurs; this step involves a subtle reorientation of the polarization field which produces an associated change in bound charges distribution which are condensed in several bands of opposite sign oriented perpendicular to the channel, making the field intensity inhomogeneous along the channel, as can be seen in purple framed snapshots of Fig. 5.10 ($t = 250\mu s$). The equilibrium configuration of σ and $E_{\|}$ is different in the considered positions of various channels (unshaded region in Fig. 5.10e), sensitively depending on the fine details of the channel, such as dimensions, surface roughness and grid spacing, making impossible a direct comparison with the experiments. A comparison between equilibrium states of a rough and a smooth "S" channel are shown in Fig 5.11, while further examples and a detailed description are present in the supporting information of[10].

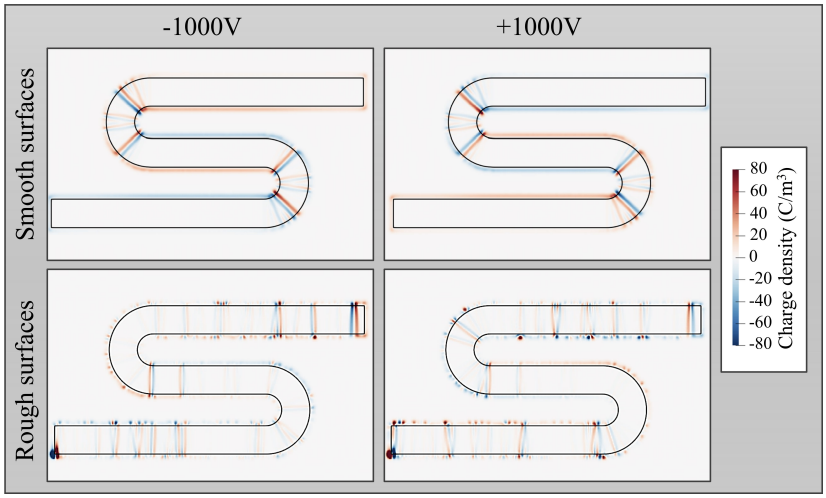

Figure 5.11: Comparison of the simulated charge density at the equilibrium in smooth and rough "S" channels

Summarizing, the simulations of the polarization inversion of an N_F material confined in different channels reveal that the switching process occurs in three different stages:

1. A rapid screening of the component of $\mathbf{E_0}$ perpendicular to the surfaces is obtained via little reorientations of the molecules next to the boundaries, resulting in a uniform electric field which follows the winding paths of the channel and an inversion of the sign of the bound charges producing an inversion of the field outside the channel. (Ferroelectric superscreening)

2. The polarization is reverted, under the conditions of a constant and uniform $\mathbf{E}$, passing through a disordered intermediate state and ending with uniform alignment of $\mathbf{P}$ along the channel. (Polarization reversal)

3. Slow reorganization of the polarization field, depending on fine details, redistributing bound charges within the channel. (Annealing)

Finally, some simulations on tapered channels have been performed to clarify the role of channel width variations in the nucleation of the interface, discovering an increase of the local electric field in the correspondence of the narrowings, producing a faster polarization reversal. The evolution of $P_{\|}$ and $E_{\|}$ in the central potion of "S" channels with different characteristics is shown in fig 5.12, where is evident that at the equilibrium, in the central region of the tapered channels the magnitude of the electric field is much higher than in untapered ones. Further examples and a detailed description is present in the supporting information of[10].

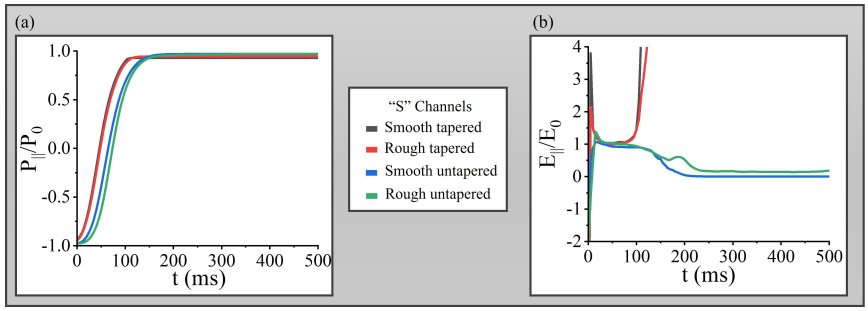

Figure 5.12: $P_{\|}(t)$ and $E_{\|}(t)$ averaged in the central section of various "S" channel with different characteristics as indicated by the legend.

The behaviour of the "I" channel is more peculiar; if a straight smooth channel is simulated, it shows a much slower dynamics which gets dramatically faster if a roughness or a tapering is introduced. Further considerations on this results are present in the next section.

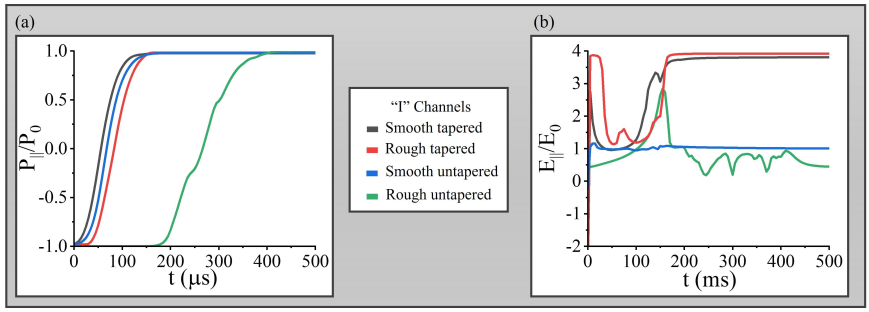

Figure 5.13: $P_{\parallel}(t)$ and $E_{\parallel}(t)$ averaged in the central section of various "I" channel with different characteristics as indicated by the legend.

5.4 Discussion

Even though the simulations have been performed with strong simplifications, the results are in good agreement with most of the experimental observations describing the peculiar features of the ferroelectric nematic phase. In both simulations and experiments the polarizations follows, in a continuous way, the channel bends, from electrode to electrode, even in sections that are opposed to the nominal applied electric field $\mathbf{E_0}$. This behaviour, as confirmed by simulations, is induced by the so-called ferroelectric superscreening, the immediate deposition of surface polarization charges that screen $E_{\perp}$, the component of the field perpendicular to the the channel surfaces, modifying the electric field inside the channel and making it aligned with the local channel axis, with an intensity that is nearly uniform and constant in every channel during the polarization reversal. The presence of superscreening and uniform guided field is experimentally confirmed by the similarity of the first step of electrically-driven polarization switching kinetics in every position of all the tested bent channel.

Another common aspect between simulations and experiments is the fracturing of the uniform N_F alignment into tiny domains to minimize the accumulation of bulk and surface bound charges resulting from the high spontaneous bulk polarization. Being the simulations confined in a 2D-plane, thus missing the third dimension, this results can be considered only a qualitative indication. Experimental data show that the completion of $\mathbf{P}$ reversal occurs through the nucleation of a uniform region in the narrowest portion of the channel, which is the zone with the highest local electric field, as confirmed by simulations. The expansion of this homogeneous region involves the motion of two charged interfaces with a velocity v_i, that is equal for the central zone of every bent channel, suggesting that the intensity of the field in that regions is roughly equal; however, to simulate this phenomenon, a much more detailed and complex simulation would be needed.

The behaviour of the "I" channel, surprisingly, is slightly different than the bent ones, showing a slower disordering of $\mathbf{P}$ combined with an higher v_i. Simulations on rough channels, however, predicts a common behaviour for all the tested geometries; instead, if a smooth linear channel is simulated, a much slower evolution of $\mathbf{P}$ is recorded. The addition of tapering or surface roughness (or both) the $\mathbf{P}$ reversal times becomes comparable to the one of bent channels. The slower dynamics in smooth linear channel could be explained as a consequence of symmetry; in this channel, indeed, there are no points in which a charge accumulation is favoured, such as the curves in bent channels. As a consequence, in the straight smooth channel, a non-zero $\nabla \cdot \mathbf{P}$ have to be accumulated

to cancel $E_\perp$, while, in the other channels, curvatures, surface roughness and tapering can provide easy accumulation points for bound charge, making the charge distribution process faster, hence the different behaviour of the linear "I" channel could be explained on the basis of its particular construction details.

5.5 Conclusions

Confining RM734, a ferroelectric nematic liquid crystal, into bent microchannels it was possible to highlight the unique capability of these materials of promptly eliminate any electric field component perpendicular to dielectric confining surfaces. This phenomenon, arising from the combination of spontaneous bulk polarization and fluidity, can be considered as a defining property of the N_F phase and has been named "ferroelectric superscreening". The elimination of $E \perp$ is obtained through subtle reorientations of $\mathbf{P}$ and appears to be the first and driving event of the complex multiscale polarization reversal occurring when the voltage at the channel ends is inverted. This superscreening acts only at the N_F-dielectric interface, when the ferroelectric material is in contact with a conductor, such as electrodes in the considered experiments, bound polarization charges can be balanced by free charges whose manipulation allows strong-electro-optical responses, as the one obtained upon inverting the potential at the electrodes.

Thanks to superscreening the field inside the sample is continuously parallel to the local channel axis inducing the polarization field to become aligned in the same direction to minimize the electrostatic energy arising when the two fields are not parallel. The observed phenomena are in fact essentially dominated by electrostatic contributions, which from the simulations appear to be 10^4 times larger than elastic contributions[10], making the N_F phase markedly different from the conventional non-polar N phase. Another interesting observations come from the "S" channel; here, in principle, the polarization can share a common orientation in all the three horizontal sections, with two abrupt polarization reversal, forming defect walls, in the two bending sections. This configuration is however unstable because such type of wall would be very highly charged, possessing a charge density of $\sim \pm 2P_0$ producing electric fields of the order of $10^{10} V/m$.

Polarization reversal, after potential inversion, is completed through the annealing if the defects in the bulk of the material and the polarity inversion of the molecules at the surfaces. These two events occur almost simultaneously in a nucleated process in which an homogeneous zone appears in the zones of the microchannels where the field is highest – such as narrowings – and expands with the motion towards the electrodes of two charged interfaces until the polarization of the channel has been completely reverted. This motion is similar to an electrophoretic-type motion in which a charged object is drag by an electric field against a viscous friction. The whole inversion process is electrically driven and specific to this particular phase in which electrostatic contributions dominate over elastic ones.

The results shown in this chapter can provide the basis to comprehend the behaviour of ferroelectric fluids when geometrical confinement effects become significant, for example when confined in different systems such as composite structures, porous materials, disordered media with with either quenched or annealed disorder, and topologically patterned substrates.

This work, furthermore, suggest that the optical axis in N_F-based electro-optical devices can be controlled, even in multiple positions, exploiting apposite designed microconfining geometries in which the ferroelectric fluid polarization can be manipulated using small electric fields.

Bibliography

[1] R. J. Mandle, S. J. Cowling, and J. W. Goodby. A nematic to nematic transformation exhibited by a rod-like liquid crystal. *Physical Chemistry Chemical Physics*, 19:11429–11435, 2017.

[2] H. Nishikawa, K. Shiroshita, H. Higuchi, Y. Okumura, Y. Haseba, S. I. Yamamoto, K. Sago, and H. Kikuchi. A fluid liquid-crystal material with highly polar order. *Advanced Materials*, 29, 11 2017.

[3] X. Chen, E. Korblova, D. Dong, X. Wei, R. Shao, L. Radzihovsky, M. A. Glaser, J. E. Maclennan, D. Bedrov, D. M. Walba, and N. A. Clark. First-principles experimental demonstration of ferroelectricity in a thermotropic nematic liquid crystal: Polar domains and striking electro-optics. *Proceedings of the National Academy of Sciences*, 117:14021–14031, 2020.

[4] O. D. Lavrentovich. Ferroelectric nematic liquid crystal, a century in waiting. *Proceedings of the National Academy of Sciences*, 117(26):14629–14631, 2020.

[5] A. Marcinkevičius, S. Juodkazis, M. Watanabe, M. Miwa, S. Matsuo, H. Misawa, and J. Nishii. Femtosecond laser-assisted three-dimensional microfabrication in silica. *Optics Letters*, 26(5):277–279, Mar 2001.

[6] R. Osellame, H. Hoekstra, G. Cerullo, and M. Pollnau. Femtosecond laser microstructuring: an enabling tool for optofluidic lab-on-chips. *Laser & photonics reviews*, 5(3):442–463, Feb. 2011.

[7] S. LoTurco, R. Osellame, R. Ramponi, and K. C. Vishnubhatla. Hybrid chemical etching of femtosecond laser irradiated structures for engineered microfluidic devices. *Journal of Micromechanics and Microengineering*, 23(8):085002, 2011.

[8] F. Sala, P. Paié, R. Martínez Vázquez, R. Osellame, and F. Bragheri. Effects of thermal annealing on femtosecond laser micromachined glass surfaces. *Micromachines*, 12 (2), 2021.

[9] F. Caimi, G. Nava, R. Barboza, N. A. Clark, E. Korblova, D. M. Walba, T. Bellini, and L. Lucchetti. Surface alignment of ferroelectric nematic liquid crystals. *Soft Matter*, 17:8130–8139, 2021.

[10] F. Caimi, G. Nava, S. Fuschetto, L. Lucchetti, P. Paiè, R. Osellame, X. Chen, N. A. Clark, M. Glaser, and T. Bellini. Superscreening and polarization control in confined ferroelectric nematic liquids. *arXiv*, 2022. URL https://arxiv.org/abs/2210.00886.

[11] Z. Zhuang, J. E. Maclennan, and N. A. Clark. Device Applications of Ferroelectric Liquid Crystals: Importance of Polarization Charge Interactions. In J. W. Doane and Z. Yaniv, editors, *Liquid Crystal Chemistry, Physics, and Applications*, volume 1080, pages 110 – 114. International Society for Optics and Photonics, SPIE, 1989.

[12] N. A. Clark, D. Coleman, and J. E. Maclennan. Electrostatics and the electro-optic behaviour of chiral smectics c: 'block' polarization screening of applied voltage and 'v-shaped' switching. *Liquid Crystals*, 27(7):985–990, 2000.

[13] Y. Shen, T. Gong, R. Shao, E. Korblova, J. E. Maclennan, D. M. Walba, and N. A. Clark. Effective conductivity due to continuous polarization reorientation in fluid ferroelectrics. *Phys. Rev. E*, 84:020701, Aug 2011.

[14] D. Coleman, D. Mueller, N. A. Clark, J. E. Maclennan, R.-F. Shao, S. Bardon, and D. M. Walba. Control of molecular orientation in electrostatically stabilized ferroelectric liquid crystals. *Phys Rev Lett*, 91(17):175505, Oct. 2003.

[15] X. Chen, Z. Zhu, M. J. Magrini, E. Korblova, C. S. Park, M. A. Glaser, J. E. Maclennan, D. M. Walba, and N. A. Clark. Ideal mixing of paraelectric and ferroelectric nematic phases in liquid crystals of distinct molecular species. *Liquid Crystals*, 49 (11):1531–1544, 2022.

CHAPTER 6

Electric field and topological defects in channels with complex geometries

6.1 Introduction

The discovery of ferroelectric superscreening and polarization control of a ferroelectric nematic liquid crystal[1,2] confined in simple linear channels[3], presented in the previous chapter, motivated the research of new phenomena which could arise from the confinement of a ferroelectric fluid in more complex geometries. These new shapes can possess, for example, branching or bridges where the symmetry breaking of the N_F phase can produce frustration and topological defects. In the current chapter some preliminary results of the confinement of RM734 in microchannels with complex geometries are presented together with an introductory discussion. All microchannels, realized with the FLICE technique[4,5] just like the ones of the previous chapter, are buried into bulk glass, possess a rounded square cross-section of width $w = 30\mu m$ and connect two round gold electrodes $250\mu m$ wide. Their geometries include a simple branch ("Y"-shaped channel), a circular section inserted into a straight channel ("Loop"–shaped channel) and a circular section linking two parallel straight channels ("Green lantern"–shaped channel) (Fig.6.1).

6.2 Materials and methods

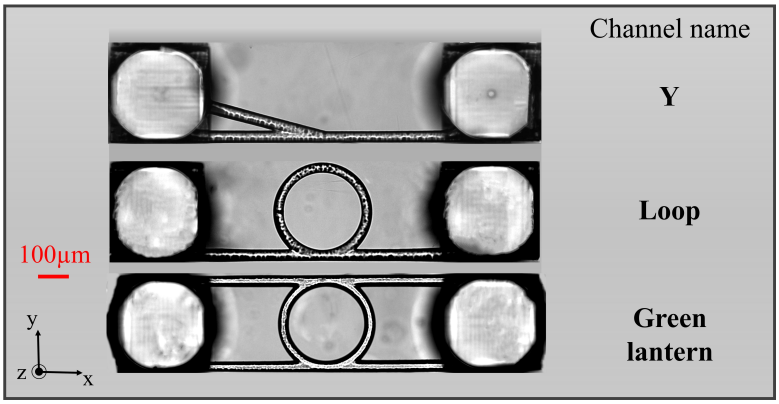

Figure 6.1: Microscopy images of the three considered channels, having different complex geometries.

The ferroelectric liquid crystal RM734 has been used to fill, with the aid of a vacuum oven the three different microchannels shown in Fig. 6.1, whose fabrication[4–7] and surface treatment[8] is equal to the previous channels and described in detail in the previous chapter.

The behaviour of RM734 confined in the microchannels has been investigated at $130°C$, in N_F phase, using PTOM. The time variation of the transmitted light between crossed polarizers has been extracted from $400FPS$ videos, recorded with a CMOS camera, using the same method explained in the previous chapter.

6.3 Experimental results and discussion

6.3.1 "Y"-shaped channel

When a potential difference, as low as $\Delta V = 0.5V$, is applied to the electrodes of a "Y"-shaped channel, a good alignment of the molecules along the channel axes is obtained, even in the oblique branch; this behaviour, predicted on the basis of the ferroelectric superscreening and coherently with the observations treated in the previous chapter, is shown in Fig. 6.2 where a voltage $\Delta V = 1V$ is applied to the terminals of the microchannel.

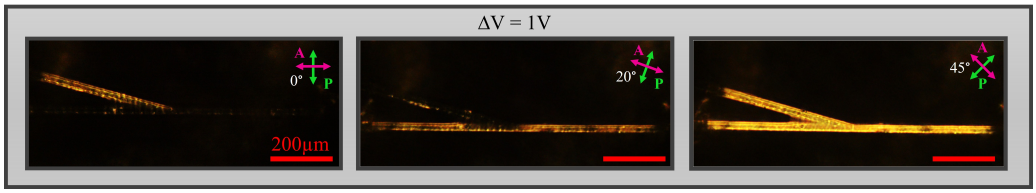

Figure 6.2: PTOM images of the "Y"-shaped channel at different orientations respect of the polarizers with $\Delta V = 1V$ applied

Inverting the sign of the voltage, a switch is provoked into the channel. However, this polarization reversal shows some differences with the one occurring in simple linear channels of chapter 5. Right after the potential inversion, a disordering in the channel appears, analogously to the simpler channels, which clears after the passage of the moving interfaces. However, in this case, the long time behaviour after positive-to-negative and negative-to-positive switches are not identical. The formation of "flame-like" defects (marked with blue frames in Fig. 6.3) is observed, which are generated from the positive electrode and wobble for several seconds before disappearing leaving a uniform texture.

Furthermore, the bifurcation region, in the negative-to-positive case, requires a much longer time to reach the equilibrium configuration; in the example shown in Fig. 6.3, for $\Delta V = 5V$, the equilibrium in the bifurcation in reached in less than $1s$ for the positive-to-negative switch while more than $90s$ are required in the case of the negative-to positive-switch. These phenomena could originate from an asymmetric motion of the ions which could be present as impurities into the LC material, helping or disturbing the alignment, or from some difference between the positive and the negative splay of RM734. Indeed, the symmetry breaking of the N_F phase can allows differences in splays of opposite sign, which are instead forbidden, for symmetry reason, in the N phase.

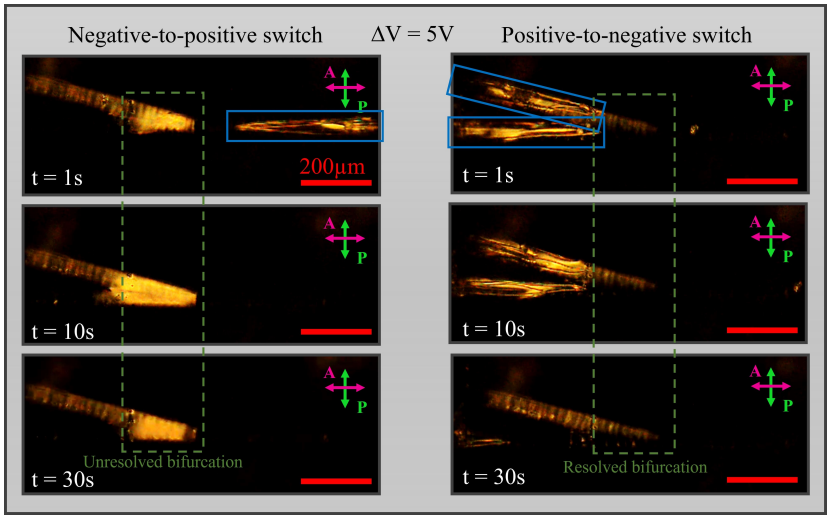

Figure 6.3: Sequences of PTOM images showing the differences of negative-to-positive and positive-to-negative switches in a "Y"-shaped channel. Blue frames highlight the flame-like defects, generated from the positive electrode. Green dashed frame indicate the bifurcation zone in which RM734 cannot find an equilibrium configuration after the positive-to-negative switch, on the contrary that negative-to-positive switch, which reaches the equilibrium in less than 1 second. After positive-to-negative switch, more than 90s are required to obtain the alignment (not shown).

Another difference between the "Y"-shaped microchannel and the simple linear channels is the fact that the birefringence growth in the disordering regime, occurring in the first instants after the voltage reversal, is not constant in the whole channel. Fig 6.4 shows that the transmitted light intensity through cross polarizers $\tau_P(t)$ is faster in the straight portion before the bifurcation; the time of the dent in the growth, indicating the time at which most of the molecules have completed half of the rotation, is indeed approximately double after the bifurcation and the slope of the curves are smaller. This indicates that the potential drop in the right, single arm is twofold the one in the left, double arms, and hence, being the lengths equal, a different electric field intensity.

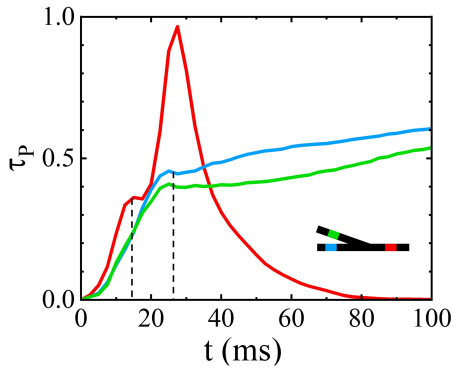

Figure 6.4: Time evolution of the transmittance between crossed polarizers $\tau_P(t)$ measured in three different portions of a "Y"-shaped channel after the inversion of ΔV from $1V$ to $-1V$.

6.3.2 "Loop"-shaped channel

To ensure the alignment of RM734 in the circular section of an "Loop"-shaped channel a voltage $\Delta V = 2V$ is required, while a $\Delta V = 0.5V$ is enough for the linear section. The obtained ordering, however, is not perfect: for every tested voltage, indeed, two different defected zones are present near the intersections between the ring and the straight part. One defect is long and narrow, while the other is short and wide as the channel; the same shapes are found in different and independent repetitions, even if the channel is filled with DIO, a different compound showing the N_F phase, but are absent in the N phase. Remarkably the position of these defects can be swapped inverting the sign of the potential difference, as shown in Fig. 6.5. Increasing the ΔV is it possible to "compress" the long defect, making it similar, but still different to the short one and obtain a better alignment into the circular region.

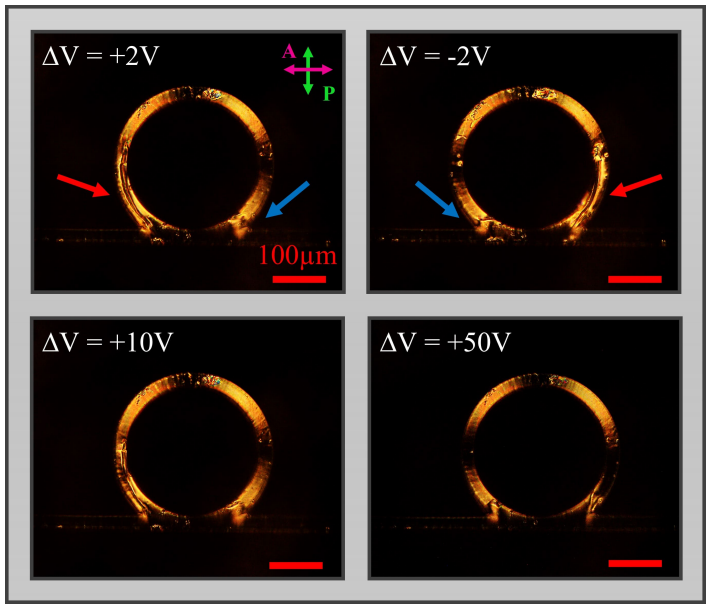

Figure 6.5: PTOM images of the "Loop"-shaped channel with various ΔV applied. Red arrow indicates the long and narrow defect while blue arrow indicates the sort and wide defect; their position is switched when the voltage is inverted.

Upon performing a PTOM analysis on these defected zones it appears that RM734 molecules are not following the channel in a straightforward "loop the loop" configuration, schematized in the left panel of Fig 6.6a, but are running in the opposite direction, as in the right panel of the same figure. This counter-intuitive orientation can be explained considering that the potential difference between the intersections of the circular and the straight part (indicated with white marks in Fig. 6.5a) needs to be equal calculated both along the central portion of the straight region and along the circle, a condition which is not obtainable with the loop the loop configuration. This inversion of the polarization direction can explain the formation of the two defected zones whose structures are graphically described in Fig. 6.6b. The motivation behind the formation of defect zones of different topology is still unknown, however, the differences could again originate from a difference in the elastic energy for positive and the negative splay deformation of the N_F phase.

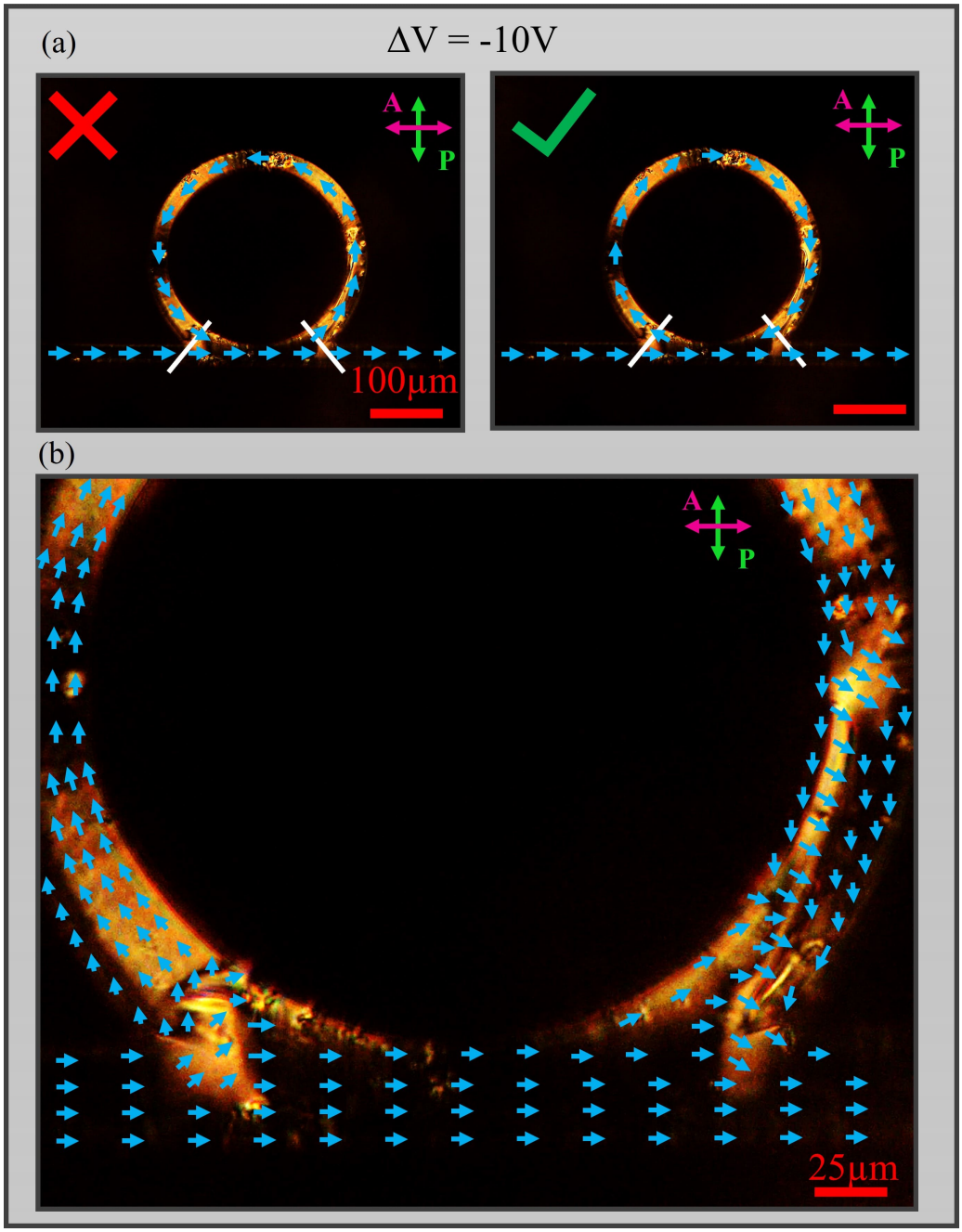

Figure 6.6: (a) The two possible orientation in the circular section of a "Loop"–shaped channel: left panel shows the straightforward loop the loop configuration while right panel shows the configuration actually assumed by RM734 polarization, represented as blue arrows. White marks indicate the intersection between the circular and the straight parts. (b) Graphical representation of RM734 polarization in the defected zones of a "Loop"-shaped channel

When the voltage is inverted the straight part completes the polarization reversal faster than the circular portion; here the final reorganization requires only a slightly longer time to merge the rotating domains but also need an additional period to recreate the inverted defect structures and reach a final equilibrium. Looking at the transmitted light intensity through cross polarizers $\tau_P(t)$, shown in Fig 6.7, is it possible to see that the disordering regime is much faster in the straight portion than every position of the circular section, in which instead $\tau_P(t)$ grows at the same rate everywhere. This indicates that the electric field have different values after the bifurcations but remains constant inside the circular section. The fact that the field intensity in the circular portion of the microchannel is only a fraction of the external nominal applied electric field E_0 can justify the larger ΔV required to align the material inside that part.

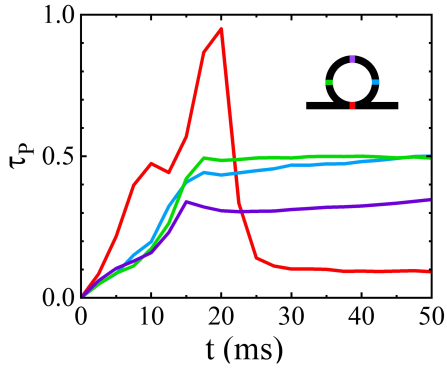

Figure 6.7: Time evolution of the transmittance between crossed polarizers $\tau_P(t)$ measured in three different portions of a "Loop"-shaped channel after the inversion of ΔV from $2V$ to $-2V$.

6.3.3 "Green Lantern"-shaped channel

The "Green lantern"' shaped microchannel gives an example of geometry in which the RM734 polarization cannot assume a simple and predictable orientation; when a voltage is applied, the molecules are indeed easily aligned within the two straight branches; however, there is no way to continuously connect them without the formation of defects in the central ring. A minimum potential difference $\Delta V = 0.5V$ is required to obtain an homogeneous alignment within the parallel sections and for $0.5V < \Delta V < 5V$ stable defects are obtained in the ring which can be modified inverting the electric field (Fig. 6.8). Their shape however is not reproducible and changes every time the voltage is inverted. These defects are probably stable because the electrostatic energy is not enough to overcome the viscosity of the material. Instead, if a $\Delta V > 5V$ is applied to the electrodes, the defects are not resolved and an equilibrium configuration cannot be obtained even after an hour. The defects in the central region, then the potential difference is high enough, continuously move, enlarging and reducing, with a speed that increases with the applied voltage (as the three bottom panels of Fig. 6.9).

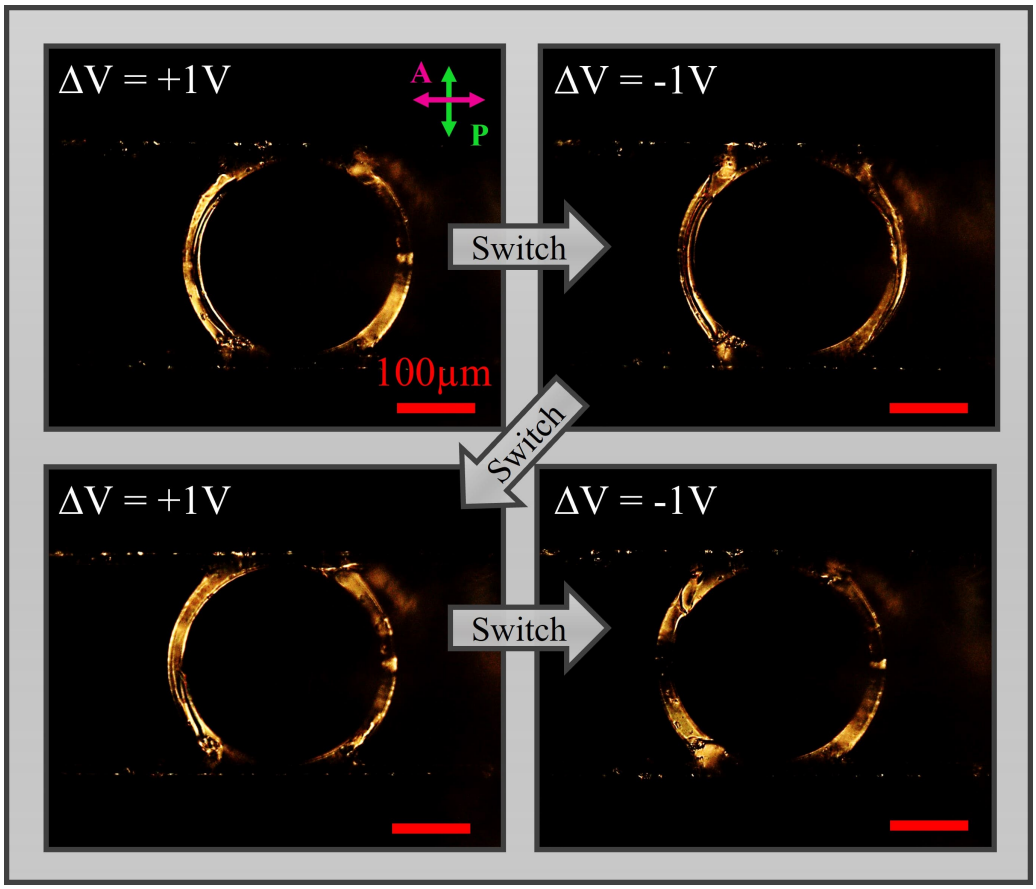

Figure 6.8: PTOM images of different equilibrium states of RM734 in a "Green lantern"–shaped channel after consecutive ΔV switching.

Looking at the polarization reversal dynamics after voltage switching is it possible to notice that the ring does not shows the breaking into microdomains seen in every position of every other channel. In the "Green lantern"–shaped channel, indeed, the typical multiscale switching dynamics only involves the two straight branches (upper panels of Fig. 6.9), which get uniform after the passage of multiple interfaces. The reorganization of the molecules inside the ring seems to occur only after the completion of the polarization reversal in the parallel arms, probably due to the new boundary conditions (central panels of Fig. 6.9). This observation could suggest that the electric field inside the ring is null or very low. After the reorganization of the defected zones in the central ring, since in the presented example the voltage used is $\Delta V = 10V$, is it possible to notice in the bottom panels of Fig. 6.9 the continuous motion of the recently formed defects.

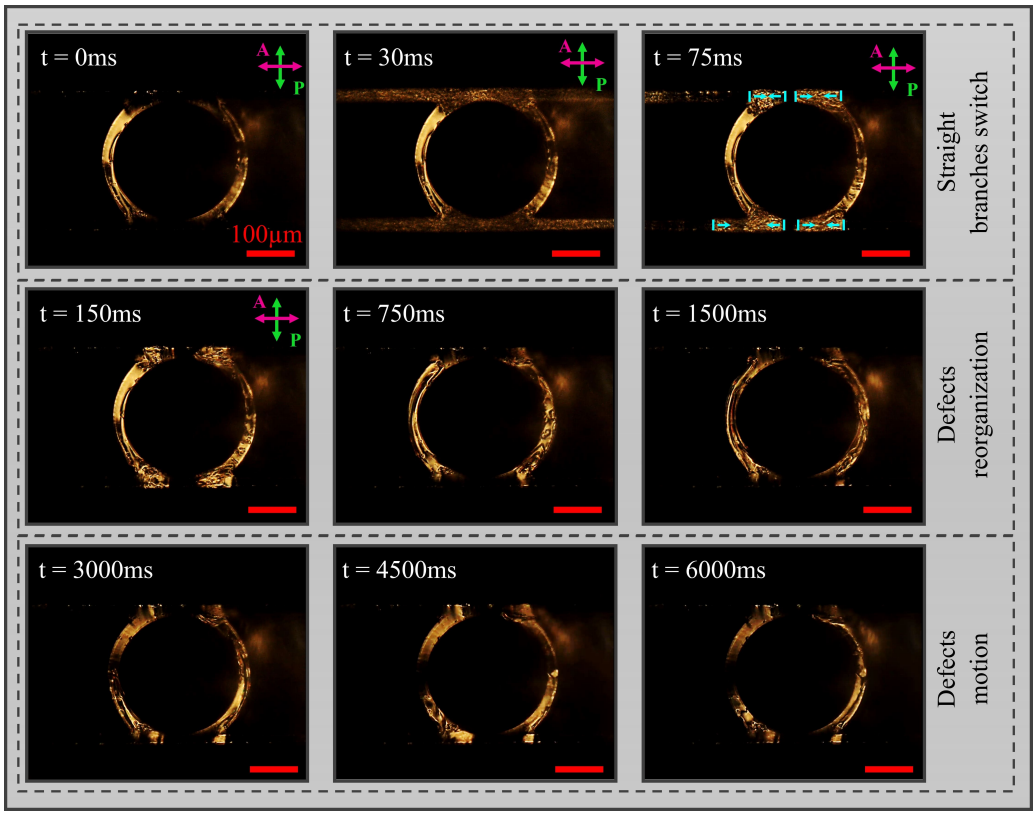

Figure 6.9: Time sequence of PTOM images showing the RM734 polarization reversal in a "Green lantern"–shaped channel after the reversal of ΔV from $-10V$ to $10V$. Light blue lines and arrows indicate the moving interfaces

6.3.4 Conclusions

In this chapter the confinement of RM734 in microchannel with complex geometries has been presented, allowing to detect new phenomena which are not present in the simple linear geometries of chapter 5. Studying the asymmetric "Y"-shaped channel, it was evident that, in this case, the positive-to-negative and the negative-to-positive voltage inversion produced different long-time dynamics in the RM734 polarization reversal, with opposite locations of the "flame-like" defects and different times required to obtain the equilibrium state.

Looking at the time evolution of $\tau_P(t)$ in various positions of the same channel it was possible to notice that the electric field inside the ferroelectric material splits roughly equally after the bifurcation, reinforcing the idea of a field guided into the channels by the ferroelectric superscreening.

This finding is also true for the "Loop"-shaped microchannel, in which the electric field in the circular section appears to be only a fraction of the nominal applied electric field E_0, in this case, however, the field is not split equally at the first bifurcation with a biggest part continuing in the straight portion and a smaller one running into the ring. Furthermore the alignment in the "Loop"-shaped channel is not uniform as in the previous cases but requires the presence of two distinct defected zones at the bifurcations; this

asymmetry in a symmetric channel is very intriguing as it could indicate the presence of a difference in the positive and the negative splays of the N_F phases.

The "Green lantern"- shaped channel represent the first example of geometry in which an equilibrium configuration cannot be found for RM734 with a continuous motion of defects under the effect of a constant potential. In this channel zones in which the electric field seems to be suppressed are also found, providing another degree of control over the fields and the polarization of ferroelectric nematic materials confined in microchannels.

All these results, although still preliminary, can be very interesting for both basic and applied researches. Asymmetric channels could indeed help on study the intimate properties of the N_F phase, such as the possible difference in positive and negative splay, never observed in any other liquid crystalline material, while bifurcations and complex geometries can provide high degrees of control over the LC polarization and confined electric fields potentially allowing the realization of advanced electro-optic devices.

Bibliography

[1] R. J. Mandle, S. J. Cowling, and J. W. Goodby. A nematic to nematic transformation exhibited by a rod-like liquid crystal. *Physical Chemistry Chemical Physics*, 19:11429–11435, 2017.

[2] X. Chen, E. Korblova, D. Dong, X. Wei, R. Shao, L. Radzihovsky, M. A. Glaser, J. E. Maclennan, D. Bedrov, D. M. Walba, and N. A. Clark. First-principles experimental demonstration of ferroelectricity in a thermotropic nematic liquid crystal: Polar domains and striking electro-optics. *Proceedings of the National Academy of Sciences*, 117: 14021–14031, 2020.

[3] F. Caimi, G. Nava, S. Fuschetto, L. Lucchetti, P. Paiè, R. Osellame, X. Chen, N. A. Clark, M. Glaser, and T. Bellini. Superscreening and polarization control in confined ferroelectric nematic liquids. *arXiv*, 2022. URL `https://arxiv.org/abs/2210.00886`.

[4] A. Marcinkevičius, S. Juodkazis, M. Watanabe, M. Miwa, S. Matsuo, H. Misawa, and J. Nishii. Femtosecond laser-assisted three-dimensional microfabrication in silica. *Optics Letters*, 26(5):277–279, Mar 2001.

[5] R. Osellame, H. Hoekstra, G. Cerullo, and M. Pollnau. Femtosecond laser microstructuring: an enabling tool for optofluidic lab-on-chips. *Laser & photonics reviews*, 5(3): 442–463, Feb. 2011.

[6] S. LoTurco, R. Osellame, R. Ramponi, and K. C. Vishnubhatla. Hybrid chemical etching of femtosecond laser irradiated structures for engineered microfluidic devices. *Journal of Micromechanics and Microengineering*, 23(8):085002, 2011.

[7] F. Sala, P. Paié, R. Martínez Vázquez, R. Osellame, and F. Bragheri. Effects of thermal annealing on femtosecond laser micromachined glass surfaces. *Micromachines*, 12(2), 2021.

[8] F. Caimi, G. Nava, R. Barboza, N. A. Clark, E. Korblova, D. M. Walba, T. Bellini, and L. Lucchetti. Surface alignment of ferroelectric nematic liquid crystals. *Soft Matter*, 17:8130–8139, 2021.

Conclusions and future perspectives

In the present thesis several aspects of the behaviour of the ferroelectric nematic liquid crystal RM734 under the effect of confinement and electric fields has been treated. In order to conclude, a brief summary of the main results obtained, along with other possible future developments of these topics, is here presented:

Surface alignment of RM734

The behaviour of RM734 confined in flat cells of various natures has been studied, allowing to detect different type of coupling with the surfaces which strongly influenced its bulk ordering[1]. The interaction strength between the liquid crystal and various materials have been evaluated through the application of external electric fields and, upon using various rubbed and unrubbed substrates, the possibility to obtain homogeneous planar alignment with a controllable orientation have been demonstrated. The observed textures have been interpreted on the basis of the symmetry breaking of the N_F phase, helping to point out the various differences between the conventional and the ferroelectric nematic phases. Among the different types of alignment obtained in the tested cells, the homeotropic alignment in the N_F phase has not been found; opposite charged surfaces or conductive material could be tested to compensate or take away the polarization charges deposited by a ferroelectric liquid when the molecules are pointing against a boundary. Untreated indium tin oxide has been tested to realize a cell but the results were unsatisfactory and hence not presented. Other possible developments could derive from the combination of different materials, rubbing direction or surface patterning on the top and the bottom surfaces, aiming to generate particular defects which could help in understanding every aspect of the newly discovered ferroelectric nematic phase. For example, combining a linearly rubbed surface with a circularly rubbed one, Rudquist developed a convenient method, based on the observed defects, to distinguish between the N and N_F phases[2].

RM734 sessile droplets on lithium niobate crystals

The deposition of RM734 sessile droplets on ferroelectric lithium niobate crystals allowed to reveal an electrostatic explosive behaviour, similar to the so-called Rayleigh instability, never observed before in neutral dielectric liquids[3]. The observed instability is provoked by the electrostatic repulsion generated by the accumulation of polarization charges on the droplet surface: when the coulombic force surpasses the surface tension of the drop a shape instability occurs and a portion of the material

is expelled as a polarized liquid jet. The dynamic and the motion of these electrostatic jets has been analyzed but some phenomena are not fully understood; further researches on these sessile droplets using both both ferroelectric solids and externally applied electric fields[4] could help in shed some light on the peculiar behaviour of the N_F phase arising from the combination of its huge spontaneous bulk polarization and its fluidity.

Furthermore, the presence of photovoltaic effects in lithium niobate crystals[5] enables the study of the coupling between light-induced electric fields and the RM734 polarization, which can produce further instabilities[6] or the motion of the entire droplets (unpublished results), opening a whole new field in electrohydromechanical researches.

RM734 confined in microchannels

The confinement of RM734 in microchannels with different shapes emphasized some of the most interesting feats of ferroelectric liquids. The capability of these materials, once put in a container, of effectively screen any electric field component normal to the confining surfaces, after being named *ferroelectric superscreening*, has been described and numerically simulated, resulting a peculiar property of the N_F phase[7].

When the potential at the microchannels terminals is inverted, a multiscale switching event of the polarization occurs whose dynamics has been studied and described. Being the polarization reversal directly dependent on the local electric field, its dynamics can be used as a proxy to evaluate the field magnitude in different portions of the various channels which appears, as confirmed by numerical simulations, constant everywhere inside linear channels, regardless of their shape. If channels with bifurcations are instead studied, it seems that the electric field splits at the bifurcation.

When asymmetric channels are investigated a difference between positive-to-negative and negative-to-positive switches is found, which is not present when symmetric microchannels are instead considered. The reason behind this behaviour is still unknown, however it could arise from a different motion of ions which could be dissolved into the materials or from a difference between positive and negative splay, a possible feature of the N_F phase, never observed in other liquid crystalline materials. To understand these differences studies on microchannels with new asymmetric geometries and further simulations will be required

If geometries in which the continuity of the polarization cannot be granted are used, defected zones are created whose structure has not been completely understood yet, requiring further studies using different techniques, such as second harmonic generation microscopy.

Even though some aspects require an additional level of understanding these results could provide the basis to understand the behaviour of ferroelectric fluids in different confinement conditions such as composite structures, porous materials, disordered media and patterned substrates and could help in the realization of novel electro-optical devices.

Bibliography

[1] F. Caimi, G. Nava, R. Barboza, N. A. Clark, E. Korblova, D. M. Walba, T. Bellini, and L. Lucchetti. Surface alignment of ferroelectric nematic liquid crystals. *Soft Matter*, 17:8130–8139, 2021.

[2] P. Rudquist. Revealing the polar nature of a ferroelectric nematic by means of circular alignment. *Scientific Reports*, 11, Dec 2021.

[3] R. Barboza, S. Marni, F. Ciciulla, F. A. Mir, G. Nava, F. Caimi, A. Zaltron, N. A. Clark, T. Bellini, and L. Lucchetti. Explosive electrostatic instability of ferroelectric liquid droplets on ferroelectric solid surfaces. *Proceedings of the National Academy of Sciences*, 119(32):e2207858119, 2022.

[4] M. T. Máthé, A. Buka, A. Jákli, and P. Salamon. Ferroelectric nematic liquid crystal thermomotor. *Phys. Rev. E*, 105:L052701, May 2022.

[5] L. Lucchetti, K. Kushnir, V. Reshetnyak, F. Ciciulla, A. Zaltron, C. Sada, and F. Simoni. Light-induced electric field generated by photovoltaic substrates investigated through liquid crystal reorientation. *Optical Materials*, 73(1):64–69, 2017.

[6] L. Cmok, N. Sebastián, A. Mertelj, Y. Kong, X. Zhang, and I. Drevenšek-Olenik. Light-induced dynamics of liquid-crystalline droplets on the surface of iron-doped lithium niobate crystals. *arXiv preprint arXiv:2208.02318*, 2022.

[7] F. Caimi, G. Nava, S. Fuschetto, L. Lucchetti, P. Paiè, R. Osellame, X. Chen, N. A. Clark, M. Glaser, and T. Bellini. Superscreening and polarization control in confined ferroelectric nematic liquids. *arXiv*, 2022. URL `https://arxiv.org/abs/2210.00886`.

List of Publications

As of 22/12/2022

Refereed publications

F. Caimi, G. Nava, R. Barboza, N. A. Clark, E. Korblova, D. M. Walba, T. Bellini, and L. Lucchetti. Surface alignment of ferroelectric nematic liquid crystals. Soft Matter, 17:8130–8139, 2021

R. Barboza, S. Marni, F. Ciciulla, F. A. Mir, G. Nava, F. Caimi, A. Zaltron, N. A. Clark, T. Bellini, and L. Lucchetti. Explosive electrostatic instability of ferroelectric liquid droplets on ferroelectric solid surfaces. Proceedings of the National Academy of Sciences, 119(32):e2207858119, 2022

Publications under review

F. Caimi, G. Nava, S. Fuschetto, L. Lucchetti, P. Paiè, R. Osellame, X. Chen, N. A. Clark, M. Glaser, and T. Bellini. Superscreening and polarization control in confined ferroelectric nematic liquids. arXiv, 2022. URL https://arxiv.org/abs/2210.00886

Publications in preparation

F. Caimi, G. Nava, P. Paiè, R. Osellame, A. Costa, N. A. Clark, M. Glaser, T. Bellini. Electric field and topological defects in RM734-filled microchannels with complex geometries.

F. Caimi, G. Zanchetta. Twisted structures in natural and bio-inspired molecules: self-assembly and propagation of chirality from the molecular to the mesoscopic scale.

F. Caimi, M. Todisco, D. Colombo, S. Sattin, T. Bellini. Self-assembly driven polymerization of activated nucleotides.

F. Caimi, F. Fontana, D. Colombo, T. Bellini. Non-enzymatic, liquid crystal promoted reparation of DNA oligomers with backbone gaps.

F. Fontana, F. Caimi, T. Bellini. Spermine-induced segregation and supramolecular ordering in AMP-UMP mixtures